EXCITATION ENERGIES AND DECAY PROPERTIES OF $T = 3/2$ STATES IN ^{17}O, ^{17}F AND ^{21}Na

Thesis by

Arthur Bruce McDonald

In Partial Fulfillment of the Requirements

For the Degree of

Doctor of Philosophy

California Institute of Technology

Pasadena, California

1970

(Submitted July 14, 1969)

TO MY WIFE, JANET

ACKNOWLEDGMENTS

It has been a great pleasure to work in the Kellogg Radiation Laboratory and I wish to express my sincere gratitude to all those who create the stimulating and enjoyable atmosphere there. I particularly wish to thank Professor C. A. Barnes for his helpful guidance throughout this work. The majority of these experiments were performed in collaboration with Dr. E. G. Adelberger. I am very grateful to him for education in the laboratory, and for introducing me to his methods of enthusiastic experimentation. The ^{20}Ne(p,p) experiment was carried out in collaboration with Dr. J. R. Patterson and Dr. H. Winkler and the mass 17 branching ratio measurements with Dr. A. P. Shukla, Dr. D. Ashery and Mr. Hay Boon Mak. I am deeply indebted to them all for their extensive contributions to all phases of the experiments. Financial assistance from the National Research Council of Canada and the California Institute of Technology is gratefully acknowledged. Finally, I wish to thank my wife for her help and encouragement at all times, and my young son, Bruce, for keeping me entertained during the long task of preparing this thesis.

ABSTRACT

The two lowest T = 3/2 levels in ^{21}Na have been studied in the ^{19}F(^{3}He,n), ^{20}Ne(p,p) and ^{20}Ne(p,p') reactions, and their excitation energies, spins, parities and widths have been determined. In a separate investigation, branching ratios were measured for the isospin-nonconserving particle decays of the lowest T = 3/2 levels in ^{17}O and ^{17}F to the ground state and first two excited states of ^{16}O, by studying the ^{15}N(^{3}He,n)^{17}F*(p)^{16}O and ^{18}O(^{3}He,α)^{17}O*(n)^{16}O reactions.

The ^{19}F(^{3}He,n)^{21}Na reaction was studied at incident energies between 4.2 and 5.9 MeV using a pulsed-beam neutron-time-of-flight spectrometer. Two T = 3/2 levels were identified at excitation energies of 8.99 ± 0.05 MeV ($J > 1/2$) and 9.22 ± 0.015 MeV ($J^{\pi} = 1/2^{+}$, $\Gamma < 40$ keV). The spins and parities were determined by a comparison of the measured angular distributions with the results of DWBA calculations.

These two levels were also observed as isospin-forbidden resonances in the ^{20}Ne(p,p) and ^{20}Ne(p,p') reactions. Excitation energies were measured and spins, parities, and widths were determined from a single level dispersion theory analysis. The following results were obtained:

$E_x = 8.973 \pm 0.007$ MeV, $J^\pi = 5/2^+$ or $3/2^+$, $\Gamma \leq 1.2$ keV, $\Gamma_{p_o} = 0.1 \pm 0.05$ keV; $E_x = 9.217 \pm 0.007$ MeV, $J^\pi = 1/2^+$, $\Gamma = 2.3 \pm 0.5$ keV, $\Gamma_{p_o} = 1.1 \pm 0.3$ keV.

Isospin assignments were made on the basis of excitation energies, spins, parities and widths.

Branching ratios for the isospin-nonconserving proton decays of the 11.20 MeV, T = 3/2 level in ^{17}F were measured by the $^{15}N(^3He,n)^{17}F^*(p)^{16}O$ reaction to be 0.088 ± 0.016 to the ground state of ^{16}O and 0.22 ± 0.04 to the unresolved 6.05 and 6.13 MeV levels of ^{16}O. Branching ratios for the neutron decays of the analogous T = 3/2 level, at 11.08 MeV in ^{17}O, were measured by the $^{16}O(^3He,\alpha)^{17}O^*(n)^{16}O$ reaction to be 0.91 ± 0.15 to the ground state of ^{16}O and 0.05 ± 0.02 to the unresolved 6.05 and 6.13 MeV states. By comparing the ratios of reduced widths for the mirror decays, the form of the isospin impurity in the T = 3/2 levels is shown to depend on T_z.

TABLE OF CONTENTS

I. INTRODUCTION

This thesis describes an experimental investigation of the properties of some higher isospin levels in light nuclei, in an attempt to gain further information on the magnitude and nature of the charge dependence of nuclear forces.

Nucleon-nucleon experiments have shown that nuclear forces are charge dependent to within ~ 5% of the strength of the interaction (see Henley 1966) and the symmetry observable in the energy levels of nuclei with the same mass number is also a strong indication of the approximate charge independence of nuclear forces.

If charge dependent interactions are neglected, then all members of an isospin multiplet with total isospin T, and T_z values of T, (T-1), ..., − (T-1), − T, have equal masses. Deviations from this result are an indication of the magnitude of charge dependent interactions, which include, of course, the Coulomb interaction. As the form of the Coulomb interaction is well known, it might be hoped that a comparison of the measured masses of the members of an isospin multiplet with those predicted from calculations including only the Coulomb interaction would provide information about other charge-dependent forces present, if any.

If charge-dependent effects are treated in first order perturbation theory, and if they are only of a two-body character (as is the Coulomb force), then the masses of the members of a multiplet are given by the so-called quadratic mass equation

(Wigner 1958, Wienberg and Treiman 1959, Wilkinson 1964):

$$M(T_z) = a + b\,T_z + c\,T_z^2 \quad .$$

T = 3/2 multiplets, with four members, are the lowest order multiplets where mass measurements of all members overdetermine the parameters of this equation and permit the T_z dependence to be tested. Such tests have been recently made in a number of these quartets in the light nuclei (for a summary, see Cerny 1969a). With the exception of the more precisely measured A = 9 multiplet (Barnes et al. 1967, Nettles et al. 1969), the masses satisfy this equation within experimental errors. For the A = 9 case, Jänecke (1969a) has recently shown that the discrepancy can be explained by including the Coulomb interaction to second order, as suggested earlier by Barnes et al. (1967).

As all charge dependent interactions of a two-body character will have a similar dependence on T_z, the identification of a specifically nuclear, charge-dependent, two-body force would depend on a comparison of the constants of the mass equation with those derived from the Coulomb perturbation alone. A number of studies of systematic mass variations have recently been reported (Hardy et al. 1969a, Jänecke 1968, 1969), but a precise calculation of Coulomb effects is difficult, as pointed out by Wilkinson (1966).

Sections II and III of this thesis describe the use of (^{3}He,n) and (p,p) reactions to locate and accurately determine the mass of T = 3/2 levels in ^{21}Na(T_z = +1/2). The lower lying T = 3/2 levels in the A = 4n + 1 nuclei are of particular interest as they

are bound to isospin-conserving particle decays and their widths and decay properties give an indication of the magnitude and extent of the isospin impurities in their wave functions. With this in mind, the ^{20}Ne(p,p) reaction was studied experimentally, with high resolution, and the data were analyzed using single level dispersion theory to determine total widths and partial decay widths for the two lowest T = 3/2 levels in ^{21}Na.

Section IV describes a detailed examination of the isospin-forbidden particle decays of the lowest T = 3/2 levels in ^{17}O and ^{17}F. A comparison of the decay properties of these mirror levels can be a sensitive probe of the nature of the isospin impurities responsible for the decays. These impurities are proportional to the off-diagonal matrix elements of charge-dependent forces, which affect nuclear masses only in second-order. It is hoped that knowledge of such impurities, coupled with precise measurements of the masses of the members of isospin multiplets, may eventually provide further information on the character of the charge dependence of nuclear forces.

II. T = 3/2 LEVELS IN ^{21}Na AS SEEN IN THE ^{19}F(^{3}He,n) REACTION

A. Introduction

At the time that this study was undertaken (McDonald and Adelberger 1968) very little was known about the excitation energies of the T = 3/2 levels of ^{21}Na. A state, believed to be the lowest T = 3/2 level, had been observed at an excitation energy of 8.90 ± 0.04 MeV as a delayed-proton-emitter following the β^+ decay of ^{21}Mg (McPherson and Hardy 1965; Hardy and Bell 1965).

The ground state of the T_z = -3/2 nucleus, ^{21}F, had been assigned spin-parity $5/2^+$ from the log ft value for its β^- decay (Kienle and Wien, 1963). Twenty-four levels of ^{21}F had been observed in the ^{19}F(t,p) reaction and angular distributions had been obtained for most of these transitions (Horvat 1964). The most intense transition observed was to the first excited state at 0.277 MeV and its angular distribution was fitted well by plane wave Born approximation calculations assuming L = 0. This implies that the level has spin and parity $1/2^+$. The transition to the ground state was weaker and was fitted adequately with L = 2. Other observed transitions were also relatively weak with maximum differential cross sections a factor of 5 to 50 smaller than those for the first excited state.

More recently, in a detailed study of the A = 21 isobaric quartet, Butler et al. (1968), studied the lowest T = 3/2 level in ^{21}Na with the ^{23}Na(p,t) reaction and assigned an excitation energy of 8.92 ± 0.03 MeV. Levels at higher excitation energy were also

observed but not identified as to isospin. They also observed the lowest three T = 3/2 levels of ^{21}Ne in the ^{22}Ne(d,t) reaction and the ground state and first four excited states of ^{21}Mg in the ^{24}Mg(^{3}He,^{6}He) reaction. The T = 3/2 levels of ^{21}Ne have also been studied recently by Hensley (1968, 1969a) using the ^{22}Ne(^{3}He,α) and ^{19}F(^{3}He,p) reactions.

The approximate energies of the low-lying T = 3/2 levels of ^{21}Na may be predicted from the known excited states of ^{21}F and its ground state mass. If it is assumed that there are no appreciable Thomas-Ehrmann shifts, then the mass of the members of an isobaric multiplet are expected to be identical, except for energy differences due to the Coulomb interaction, and the neutron-hydrogen mass difference. Thus, the masses of the members of an isobaric multiplet may be expressed (approximately) as:

$$M(T_z) = Z\,M_H + (A-Z)\,M_n - B + Z(Z-1)KA^{1/3}$$

where B is the binding energy due to the nuclear force, assumed to be constant within a given multiplet, and the Coulomb constant K is assumed to be the same for all levels of a given nucleus. If the constant K is evaluated from the ^{21}Ne-^{21}Na ground state mass difference, excitation energies of 8.80 and 9.08 MeV are predicted for the lowest two T = 3/2 levels in ^{21}Na.

The (^{3}He,n) reaction has been observed to preferentially populate low-lying T = 3/2 levels in light nuclei (Dietrich 1964 and Adelberger 1967), because the simple configurations of these levels are easily reached by one-step diproton stripping.

The extreme single particle Nilsson model may be used to make some qualitative predictions about the configurations of the lowest T = 3/2 levels of ^{21}Na. For the two neutrons and three protons outside an ^{16}O closed shell, we may assume that two neutrons and one proton are in Nilsson orbit 6 ($\Omega = 1/2^+$) and two protons are in Nilsson orbit 7 ($\Omega = 3/2^+$). The lowest two T = 3/2 levels, with $J^\pi = 5/2^+$ and $1/2^+$, could then be members of a K = 1/2 rotational band based on this configuration (Bhatt 1962, Horvat 1964). The ground state of ^{19}F has been interpreted as a member of a K = 1/2 rotational band based on a configuration with two neutrons and one proton in Nilsson orbit 6 outside an ^{16}O core (Paul 1957, Bhatt 1962).

We would therefore expect to preferentially populate the lowest two T = 3/2 levels in ^{21}Na in the ^{19}F(^{3}He,n) reaction because their configurations are easily reached by one-step diproton stripping, whereas the neighboring T = 1/2 levels at such a high excitation energy have complicated configurations which have a small overlap with ^{19}F(0.0) surrounded by two correlated protons. In analogy to the ^{19}F(t,p) reaction, we would expect the angular distribution of the levels at 8.80 and 9.08 MeV to exhibit L = 2 and L = 0 double stripping patterns, respectively.

T = 3/2 levels in ^{21}Na at energies above 12.70 MeV are unbound to isospin-conserving particle decays to ^{20}Ne(10.27, T = 1) + p, and may therefore have appreciable widths. Although at least eight other T = 3/2 levels in ^{21}Na may be expected to lie below this threshold, they are all expected to be weakly populated in the

(^{3}He,n) reaction since only two of these states have peak intensities as great as 1/5 of that of the first excited state in the ^{19}F(t,p) reaction.

B. Apparatus

1. Beam Pulsing System

The experiments were performed using the pulsed-beam-time-of-flight spectrometer associated with the ONR-CIT tandem accelerator to obtain time-of-flight spectra of the neutrons produced in the (^{3}He,n) reaction. The beam pulsing system and neutron spectrometer have been described in considerable detail elsewhere (Dietrich 1964, 1965, and Adelberger 1967); only a brief description will be given here, together with a discussion of some additional characteristics of the apparatus which were discovered during the process of this and other more recent experiments.

Figure 1 is a block diagram of the system. The beam from the tandem accelerator is pulsed by sweeping it vertically across a pair of slits to produce bursts of approximately two nanoseconds duration at intervals of 280 nanoseconds. In order to increase the current in the pulses, the ions are velocity-modulated before entering the tandem so that they arrive at the chopping slits in bunches. If the amplitude and phase of the bunching voltage are properly adjusted, these bunches will arrive just as the beam is sweeping past the opening in the slits and the current in the transmitted beam pulse will be enhanced. As the phase of the bunches, relative to the

sweeping voltage, is very sensitive to fluctuations in the energy of the ions from the ion source, it is necessary to control this phase by means of a feedback system. This circuit (Adelberger 1967a) balances the beam collected on the upper and lower chopping slits. A typical operating value for the beam-burst length is 2.5 ns for 10 MeV $^{3}He^{++}$ ions with a time-averaged beam current of 200 nanoamperes on target.

In his discussion of limits on the time resolution of the system, Adelberger (1967) suggested that the restriction of time resolution to 1.8 ns for $^{3}He^{++}$ at 10 MeV was due to nonisochronous paths through the 90^{o} analyzing magnet. To test this hypothesis, the time resolution was investigated using an 8.5 MeV $^{4}He^{++}$ beam which would have a predicted minimum beam burst duration of 2.2 nsec, assuming the maximum possible difference in path lengths through the magnet (1.75") as Adelberger had for the $^{3}He^{++}$ beam. The time resolution was determined by observing the width of the peak produced by prompt gamma rays from a quartz target; this includes both the beam burst duration and the electronic circuit resolution, the latter of which has been determined to be 1 nanosecond full width at half-maximum (FWHM) by using coincident-gamma-ray sources (Adelberger 1967). For the usual r.f. voltage on the deflecting plates (~5kV), with the chopping slits set at ± 0.150", the observed FWHM was 2 nsec. Increasing the chopping voltage by a factor of 2 reduced the FWHM to 1.6 ns. Reducing the chopping slit spacing to ± 0.030" further reduced the FWHM to 1.25 nsec. If we assume that the total FWHM = $((\Delta t_E)^2 + (\Delta t_B)^2)^{1/2}$ where Δt_E and Δt_B are the electronic time

resolution (1 nsec) and beam burst width respectively, one obtains Δt_B = .75 nsec. This is not a very precise determination, due to uncertainties in Δt_E, but certainly $\Delta t_B \lesssim 1$ nsec. A time resolution of this order has also been observed with 7 MeV proton beams by similar reductions in chopping slits. Of course, such small slit spacings result in a reduction in the time-averaged beam current by a factor of 10 to 15 so that beam currents on target are less than 10 nanoamperes. However, it is clear that there is no lower limit on the beam pulse width of the system, at least down to ~ 1 nsec, other than that set by the practical requirement of sufficient beam current.

2. Neutron Detection

Neutrons were detected by the observation of proton-recoil scintillations in a 2" thick by 5" diameter piece of "Pilot B" plastic scintillator, mounted on a 5" diameter phototube (XP1040). The detector is mounted inside a large neutron collimator and shield, and is surrounded by a lead cylinder 1.625" thick, to reduce background from gamma rays.

The target is viewed by the scintillator through a 5" diameter cylindrical hole in a 22" diameter cylinder of lithium carbonate and paraffin. This "cannon" extends for 0.84 meters in front of the detector to serve as a neutron collimator, as well as surrounding the detector to reduce the background of scattered neutrons from directions other than that of the target.

A 1/2" thick lead disc in front of the neutron detector

attenuates low energy gamma rays by a factor of about 8.5, while attenuating neutrons in the range 1-20 MeV by an approximately constant factor of 1.5.

The collimator and detector are mounted on a cart which moves on an I beam so that the detector can be reproducibly positioned at distances from 1 to 3.6 meters from the target, over the angular range from 0^{o} to 150^{o}.

3. Electronics

In this experiment, neutron flight times were determined from the time interval between pulses from the neutron scintillation counter and a timing pulse produced by the r.f. deflection voltage, as discussed below.

Figure 2 is a block diagram of the electronic apparatus.

A negative, fast timing signal, derived from the anode of the XP1040 photomultiplier, is clipped by a 1.22 m long shorted cable, inverted by a pulse transformer and inspected by the START input discriminator of the ORTEC Model 437 time-to-amplitude converter (TAC). The discriminator triggers at -250 millivolts, near the zero-crossing point of the signal. The photomultiplier was operated at a voltage of +2250 volts which was chosen as a compromise between large signal output and low noise. The length of the clipping cable was selected empirically to give the best time resolution for a peak produced by prompt gamma rays having a large range of energies.

An r.f. signal, derived from a two-turn loop mounted near the beam-deflecting plates, was passed through a variable delay line,

amplified, and inspected by a fast discriminator whose output went to the STOP input of the TAC. The variable delay line was used to change the phase of the STOP pulses, relative to the time of arrival of beam pulses at the target, so that the region of interest of the time spectrum fell within the range of the TAC.

A digital spectrum stabilizer monitored the position of the prompt gamma ray peak and continuously adjusted the zero level of the multi-channel analyzer to compensate for residual time drifts of the STOP pulses.

A linear signal, derived from dynode 11 of the photomultiplier and referred to later as the slow channel, was inspected by a discriminator whose output gated the multichannel analyzer. This discriminator level was set to eliminate phototube noise and small scintillator pulses which would have poor time resolution. Its effect on neutron detection efficiency is described in Section II, C.

4. Target Chamber and Targets

Targets were prepared by evaporating 100 to 300 $\mu g/cm^2$ of reagent grade CaF_2 onto 0.015" thick tantalum backings. Since a neutron group from the $^{12}C(^3He,n_o)$ reaction occurred at a flight time close to that of the lowest T = 3/2 level of ^{21}Na, the target was surrounded by a copper sleeve, cooled by a liquid nitrogen bath to reduce carbon buildup. Carbon targets were used for calibration runs; these were 30 $\pm$ 6$\mu g/cm^2$ thick natural carbon foils purchased from Yissum Research Development Company, Jerusalem, Israel.

The target chamber consisted of a 1" outside diameter glass "tee", centered over the pivot point of the I-beam which positioned the neutron detector cart. The targets were maintained at +300 volts potential, to reduce secondary electron emission, and the glass tube before the target was encircled by a wire suppression ring at -300 volts. The beam charge was collected and integrated by a BNI model 1000 current integrator, which was used to turn off the multichannel analyzer after a predetermined total charge.

C. Experimental Methods

1. Detector Efficiency

The measured neutron detection efficiency is displayed in Figure 3. The sharp reduction in efficiency at low energies is produced by the slow channel discriminator described in Section II, B. This discriminator level was set at the midpoint of the high energy edge of the Compton electron spectrum produced by γ rays from a ^{137}Cs source, with an 18 db attenuator inserted at the input to the slow channel amplifier. After setting the discriminator level, the attenuator was removed; the resultant discriminator level corresponded approximately to an energy of 60 keV for electron-induced scintillator pulses and 450 keV for proton recoils produced by incident neutrons.

For neutron energies between 1.95 and 10.75 MeV the detection efficiency was measured using the $d(d,n)^3He$ reaction at 7.6 MeV incident energy. The gas target cell described by Adelberger (1967) was used so that the number density of target nuclei could be

determined with precision. The absolute d + d neutron cross sections were interpolated from the table of Brolley and Fowler (1960).

At energies below 2.6 MeV, the relative detection efficiency was determined by using the $t(p,n)^3He$ reaction at 3.6 MeV, with a ZrT target. Relative cross sections were taken from Goldberg et al. (1961), and the relative efficiency was matched onto the absolute efficiencies determined from the d(d,n) reaction in the region where the neutron energies overlapped.

All neutron peaks were observed to have a "tail" on the low neutron energy side, as shown in Figure 4, a neutron peak from the $^{13}C(\alpha,n_o)$ reaction. This tail is presumed to be caused by neutrons scattered from the inside walls of the neutron collimator and from $(n,n'\gamma)$ reactions in the collimator and shield. It is observed to be dependent on neutron energy and flight path. The size of this tail relative to the main peak was studied by observing a 6.8 MeV neutron peak, from the $^{13}C(\alpha,n_o)$ reaction, at various detector distances.

The main peak was approximated by a symmetric triangle defined by the peak height and the slope of the high energy side, as shown in Figure 4. The remaining counts were assumed to make up the "tail". The main peak defined in this manner was found to vary as r^{-2} (r ≡ detector-target distance), as expected for the detector solid angle. The tail, however, was found to vary approximately as $r^{-3.5}$, so that the ratio of tail to main peak was not constant.

At a distance of 2 meters, where the detector efficiency measurements were made, the tail was 15 percent as large as the main

peak, and at the closest distance employed, 1.1 meters, it was 25 percent.

Since it is difficult to separate the tail from the main peak in more complicated spectra with varying background levels, the detector efficiency was calculated with the tail included, and all peaks for which the absolute intensity was needed were integrated in a similar manner. For distances greater than 1.5 meters, the error due to the fact that the tail does not satisfy the inverse square law is less than 10 percent. For measurements at shorter distances than this, the neutron angular distribution may be significant in determining line shapes so that more care should be exercised in determining effective detector efficiency for individual cases.

The solid curve shown in Figure 3 has been computed from an expression, quoted by Dietrich (1964), in which multiple scattering, scattering from carbon in the scintillator, and scattering and absorption in the collimator and shield are neglected. A slow channel discriminator cutoff at 450 keV proton energy was used in the calculation. The measured efficiency does not fall as steeply with energy as the computed curve; so for interpolation above 1 MeV, the efficiency has been approximated by the two dashed straight lines. In all data presented, the detection efficiency has been taken from the dashed lines, with an assumed relative error of ± 5 percent. An overall error of ± 10 percent has been assumed for the absolute efficiency.

2. Target Thickness

The energy loss of ^{3}He particles in the CaF_2 targets at the energies of interest, was determined from a comparison of the energies of ^{3}He particles, elastically scattered at 90°; from the target backing and from a clean piece of tantalum. The 24" radius magnetic spectrometer and 16 counter array were used to examine the spectrum of elastically scattered ^{3}He; Figure 5 shows the results of a typical run. Part (a) shows a plot of the number of ^{3}He particles detected versus NMR frequency, for a clean piece of tantalum inclined at a 45° angle to the beam. Part (b) shows a similar plot where the ^{3}He particles have to traverse the CaF_2 coating on a tantalum backing. The reduction in the maximum energy of the scattered particles, due to the energy loss in the CaF_2 layer, may be determined with sufficient precision, even though the slope of the high energy edges are different due to energy loss straggling in the CaF_2 layer, by taking the difference in the energies of the midpoints of the edges as a measure of the total energy loss in the CaF_2 layer.

D. Results

1. Indentification of T = 3/2 Levels

The $^{19}F(^3He,n)^{21}Na$ reaction was studied for various ^{3}He incident energies between 4.2 and 5.9 MeV, covering excitations in ^{21}Na up to 11 MeV. A neutron time of flight spectrum at an incident energy of 5.855 MeV and an angle of 0° is displayed in Figure 6. A

number of neutron groups may be seen above a large continuum due to reactions with multibody final states. In the region around 9 MeV excitation, where the low-lying T = 3/2 states are expected, three levels were observed: an intense forward-peaked group at a ^{21}Na excitation energy of 9.22 MeV, a weaker group at 8.41 MeV, and a group at 8.99 MeV which is partially obscured by neutrons from the $^{12}C(^{3}He,n_{o})$ reaction.

Since the 8.99 and 9.22 MeV levels have angular distributions and energy spacings similar to those observed in the $^{19}F(t,p)$ reaction (Horvat 1964), we tentatively identify them as the lowest two T = 3/2 levels in ^{21}Na and proceed to investigate their properties further, to substantiate this hypothesis.

For this purpose angular distributions were taken, and Q-values were measured at all angles to verify that the levels were produced by a target of mass 19. As these levels are bound with respect to isospin-conserving decays, they are expected to be narrower than the experimental resolution; hence only an upper limit for their width could be determined from the data.

A number of other weakly populated levels were observed in the excitation energy region between 9.2 and 11 MeV but none of them could be clearly discerned to be analogues of levels in ^{21}F.

2. Angular Distributions

An angular distribution of neutrons corresponding to the 9.22 MeV state is presented in Figure 7, for $E_{^3He}$ = 5.86 MeV. In

addition to the errors shown in the figure there is an overall uncertainty of ± 20 percent in the absolute normalization due to uncertainties in target thickness, detector efficiency and charge integration. The density of target nuclei was determined from the energy loss measurements described in Section II,C and the dE/dx tables of Demirlioglu and Whaling (1962). It was not possible to obtain a reliable angular distribution for the 8.99 MeV level due to the presence of carbon contamination, which built up slowly during the accumulation of the experimental data in spite of the presence of the cold sleeve. However, the angular distribution of neutrons from the combination of the 8.99 MeV state and the $^{14}O(0.0)$ level was not forward peaked. The $^{12}C(^{3}He,n)^{14}O(0.0)$ reaction was examined at the same incident energy and found to be strongly forward peaked; it may be concluded therefore that the angular distribution for the 8.99 MeV level is peaked away from 0^{o}.

Figure 8 shows the neutron time of flight spectrum obtained at an incident energy of 5.855 MeV and a laboratory angle of 60^{o}. Both the 8.99 and 9.22 MeV levels are clearly visible, and from the $^{12}C(^{3}He,n_{o})$ angular distribution and the peak observed at 0^{o}, it can be calculated that the 8.99 MeV peak could not contain more than 20 percent contribution from the carbon contaminant, at this angle.

Direct reaction distorted wave Born approximation (DWBA) calculations were performed using the computer code Julie written by Bassel, Drisko and Satchler (1962). The assumptions made in using this code for two particle transfer reactions have been dealt with in detail by Adelberger (1967). The essential feature is that the

two protons in the transferred diproton are assumed to be in a relative 1s state with total spin S = 0 and total isospin T = 1. The calculations may then be performed in the same way as for single particle stripping, using the zero range approximation, and assuming that the diproton is transferred as a single particle.

The optical model potentials used in the calculations are listed in Table 1. The ^{3}He potentials were obtained from an analysis of ^{3}He elastic scattering on ^{19}F by Matous et al. (1966). The neutron potentials are those used for protons in an analysis of the (t,p) reaction on a series of light nuclei (Glover and Jones 1966) (without the Coulomb potential, of course) and were also used in analysis of (^{3}He,n) reactions to other T = 3/2 and T = 2 levels in light nuclei (Adelberger et al. 1969).

The solid curve in Figure 7 is the result of the calculation for transferred angular momentum L = 0; the curve is easily distinguished from the L = 1 case, shown as the dashed curve. This establishes the spin and parity of the 9.22 MeV level as $1/2^{+}$.

Since the neutron group leading to the 8.99 MeV state is not forward-peaked, we conclude that L > 0 for the transition to the state. This is consistent with the L = 2 double stripping expected from our identification of this state as the lowest T = 3/2 level, with spin-parity $5/2^{+}$.

3. Level Widths

Time-of-flight spectroscopy is not a very sensitive method for the determination of the width of narrow levels, but it is possible to do so if a number of simplifying approximations are made for

various contributions to the experimental resolution.

1. It may be assumed that the shape of the prompt gamma ray peak is a good representation of the beam burst shape and electronic resolution for neutrons. The electronic resolution was measured to be 1.4 ns FWHM for 60 to 120 keV gamma rays, which produce a scintillation light output similar to that for 1 MeV neutrons, and 1 ns FWHM for 511 keV gamma rays. Since these are both small compared to the typical beam burst width of 2.5 ns, this difference is not significant.
2. The time broadening function due to detection of neutrons at different points through the scintillator may be approximated by a rectangle of width equal to the flight time of neutrons through the 2" scintillator thickness.
3. The resolution function due to finite target thickness may be approximated by a rectangle of width equal to the difference in flight times of neutrons for the level in question produced by the maximum and minimum incident energies.

A computer program was written which folded together these three contributions with a theoretical level shape obtained by converting a Breit-Wigner shape into the corresponding function with flight time as the independent variable. The resultant shape was then compared with the observed peak and χ^2 was calculated for various assumed values of the total width Γ.

This calculation ignores the presence of "tails" on the neutron peaks due to scattering in the neutron collimator. For this reason, another set of calculations was performed folding together

the neutron line shape from the $^{12}C(^{3}He,n_o)$ reaction on a thin carbon target, the target thickness rectangle and the Breit-Wigner shape. The derived upper limits on Γ were similar for both methods.

The total width of the 9.22 MeV level was determined to be less than 40 keV. It was not possible to make such a determination for the 8.99 MeV level, due to the presence of the unresolved contaminant group from the $^{12}C(^{3}He,n_o)$ reaction.

4. Q-Values

Accurate measurement of Q-values is dependent largely on the calibration of the time scale of the time-of-flight spectrum. For approximate measurements, the time scale could be determined from the shift in peak position caused by the insertion of a delay cable whose length was known to be 149.7 ± 0.3 nanoseconds from previous calibrations with reactions having known Q-values. However, better precision is obtained when a direct comparison can be made between the neutron peak in question and a neutron peak with the same flight time from another reaction with an accurately known Q-value. The spectrometer is then used only as a device for comparing flight times, and errors due to uncertainties in the detector distance and angle, nonlinearities in the time scale and uncertainties in time calibration are either greatly reduced or totally eliminated. The remaining uncertainty arises from the calibration of the incident beam energy, target thickness, and the precision with which a peak can be located in the time spectrum.

The $^{12}C(^{3}He,n)^{14}O(0.0)$ reaction was used as a calibration for the determination of the Q-values of the 8.99 and 9.22 MeV levels. The incident energy had to be changed by less than 10 percent in each case to produce neutrons of the same energy leading to $^{14}O(0.0)$ and to the ^{21}Na state.

A computer program developed originally by Dietrich (1964) and extended by Adelberger (1967) was used for the analysis of the data. At the beginning of each running day the linearity of the TAC plus multichannel analyzer was determined by accumulating a time spectrum with START signals produced by a radioactive source near the detector and STOP signals from the 3.531 MHZ oscillator. As the source events occur randomly in time, this spectrum should be completely flat if the channels correspond to equal time intervals; the deviations from linearity are used by the computer to correct the time scale.

The zero of the time scale is determined from the well-defined position of the peak produced by prompt gamma rays from the target which may be seen near channel 190 in Figures 6 and 8. The computer program uses the calibration information to determine the neutron energy for each channel, and also calculates the equivalent excitation energy in the residual nucleus. A recent useful addition to the program produces a point plot of the data similar to Figures 6 and 8, complete with excitation energy scale to facilitate peak identification. The program also calculates the errors in Q-value resulting from the uncertainties in incident energy, counter distance and angle, and peak location for both the reaction under study and the calibration reaction.

The statistical uncertainty in the incident beam energy was taken to be one-third of the theoretical maximum allowed by the finite slit spacings of the 90^{o} beam analyzing magnet (Pearson 1963),

$$\frac{\delta E}{E} = \frac{1}{3}\frac{\delta E_{max}}{E} = \pm \frac{1}{6}\left(\frac{S_1 + S_2}{R}\right)$$

where S_1 and S_2 are the full widths of the object and image apertures and R (= 34") is the radius of the analyzing magnet. For $S_1 = S_2 = 0.100"$ we obtain

$$\frac{\delta E}{E} = 1 \times 10^{-3} \ .$$

The main contribution to the error in the Q-value determination for the 9.22 MeV level results from the uncertainty in the shape of the background underlying the T = 3/2 peak. For this reason, it was necessary to work at incident energies about 3 MeV above the threshold for production of the level in order to enhance its population cross section relative to the background. As the accuracy of the time-of-flight spectrometer is reduced when the neutron energy increases, it was necessary to accept larger errors in Q than have been previously achieved with this apparatus (Adelberger et al. 1969).

Three separate measurements were made of the Q-value leading to the 9.22 MeV state, with a standard deviation of only 6.7 keV. However, the systematic error arising from uncertainties in the shape of the background under the peak can contribute a maximum error of ± 13 keV. We therefore adopt a Q-value of -1.662 ± 0.015 MeV, which corresponds to an excitation energy of 9.221 ± 0.015 MeV for the

second T = 3/2 state of ^{21}Na. The ^{21}Na ground state mass was taken from a recent measurement by Bloch et al. (1967).

The presence of the contaminant peak from the $^{12}C(^{3}He,n_{o})$ reaction produced a large uncertainty in the location of the centroid of the 8.99 MeV peak. The best value which could be obtained was 8.99 ± 0.05 keV for the excitation energy of the lowest T = 3/2 level in ^{21}Na.

To establish that the 9.221 MeV level was in fact produced by reactions on a mass 19 target, Q-values were computed from the series of runs making up the angular distribution, assuming various target masses from 12 to 28. The χ^2 value for a fit to a constant Q-value is shown as a function of target mass in Figure 9 and it may be seen that the best fit is obtained for a mass 19 target. This demonstrates that the 9.221 MeV level belongs to the nucleus ^{21}Na.

It was not possible to determine the target mass for the group leading to the 8.99-MeV state since it could not be observed over a sufficiently wide range of angles. However, it could not have been produced from ^{16}O or ^{40}Ca since these reactions have more negative Q-values. It is unlikely that the group is produced by a target with Z much greater than 10, in any case, because the Coulomb barrier would strongly inhibit the reaction. Since the neutron group cannot be ascribed to any likely contaminants in the target, and appears with equal intensities in spectra taken with several different CaF_2 targets, we conclude that it also is produced by an ^{19}F target and corresponds to a level in ^{21}Na.

E. Conclusions

The lowest two T = 3/2 levels of ^{21}Na have been identified at excitation energies of 8.99 ± 0.05 MeV and 9.221 ± 0.015 MeV. The identifications are based on a comparison of intensities, angular distributions, and separation energies with the levels of ^{21}F observed in the ^{19}F(t,p) reaction. The 8.99 MeV level has L > 0 and is assumed to be the analog of the ^{21}F ground state. The 9.221 MeV level is populated by an L = 0 transition implying $J^{\pi} = 1/2^{+}$ and has a width less than 40 keV.

The information which has been obtained for these levels is not as accurate as has been obtained in the past for similar low-lying T = 3/2 levels in light nuclei. The 50 keV error in the excitation energy of the lowest T = 3/2 level does not allow a very sensitive test of the quadratic mass law.

As a result, another experiment was undertaken to look for these same levels in ^{21}Na as isospin-forbidden resonances in the ^{20}Ne(p,p) reaction, an experiment which should produce more accurate numbers for excitation energies and total widths, and which could provide further information regarding the partial decay widths for the levels.

III. T = 3/2 LEVELS IN ^{21}Na AS SEEN IN THE ^{20}Ne(p,p) REACTION

A. Introduction

The lowest T = 3/2 levels in ^{21}Na are bound with respect to isospin-conserving particle decays, as may be seen in Figure 10, which is an isobar diagram for mass 21. These levels can only decay by γ emission, or by p and α emission as a result of isospin impurities in the T = 3/2 states or in the energetically-allowed final states of ^{20}Ne or ^{17}F. For this reason, the T = 3/2 states are expected to be narrower than neighboring T = 1/2 levels, and should be observable as compound nuclear resonances in the elastic and inelastic scattering of protons from ^{20}Ne provided that Γ_{p_o}/Γ is not negligible, and Γ is not too much smaller than the experimentally achievable energy resolution.

This method of studying these levels is capable of higher precision in the determination of excitation energies and widths than the ^{19}F(^{3}He,n) reaction. The method, however, can be tedious and unfruitful if the positions of the T = 3/2 levels have not been previously determined with sufficient accuracy to restrict the region of excitation energy which must be surveyed in small energy steps, and with high resolution.

A number of T = 3/2 and T = 2 levels in light nuclei have already been observed as resonances in isospin forbidden reactions. For example, T = 3/2 levels in ^{13}N have been observed by Temmer and

and Van Bree (1966) and Levine and Parker (1967) in the reactions $^{12}C(p,p)$ and (p,p') and by Dietrich et al. (1968), in the $^{12}C(p,\gamma)^{13}N$ reaction; T = 3/2 levels in ^{13}C have been observed by Miller and Kavanagh (1966) and Snover et al. (1968), in the $^{9}Be(\alpha,\gamma)^{13}C$ reaction; T = 3/2 levels in ^{17}F have been studied by Hardie et al. (1963), Patterson et al. (1967), and Temmer et al. (1967), in the $^{16}O(p,p)$ and (p,p') reactions; a T = 2 level in ^{20}Ne has been seen in the reaction $^{19}F(p,p)$ by Bloch et al. (1967a), and by Kuan et al. (1967), who also observed it in the $^{19}F(p,\gamma)$ reaction; a T = 2 level in ^{24}Mg has been studied by Reiss et al. (1967), in the reactions $^{23}Na(p,\gamma)^{24}Mg^{*}$ and $^{23}Na(p,p_o)$.

The observed widths for these levels are all less than 8 keV, and are generally of the order of 2 keV, although the lowest T = 3/2 level of ^{17}F has been shown to have a total width less than 1.2 keV. Isospin assignments for these resonances were made on the basis of their narrow widths and from correspondences with the excitation energies and spins and parities of their analogue levels as measured in isospin allowed reactions.

This section reports a search for resonances corresponding to the lowest T = 3/2 levels in ^{21}Na, in the $^{20}Ne(p,p)$ and (p,p') reactions, over an excitation energy range from 8.87 to 9.42 MeV in ^{21}Na. This range includes the regions where T = 3/2 levels were observed in the $^{19}F(^{3}He,n)$ reaction as reported in Section II.

As these scattering anomalies are expected to be very narrow, a differentially-pumped gas target of natural neon was used, so that the energy resolution would be limited only by the beam

energy spread.

Two cross section anomalies were observed which were much narrower than others nearby and occurred near the expected positions of the T = 3/2 states. Section III, D. describes the analysis of the data which indicates that the spins and the parities of these states are consistent with those expected for the T = 3/2 levels. These anomalies are therefore assumed to correspond to the two lowest T = 3/2 levels in ^{21}Na and their excitation energies were determined to be 8.973 ± 0.007 MeV and 9.217 ± 0.007 MeV.

B. Experiment

1. Apparatus

The differentially-pumped gas target system is shown in Figure 11. It was designed and originally used for the observation of T = 3/2 levels in ^{17}F in the ^{16}O(p,p) and (p,p') reactions by Patterson, Winkler and Zaidins (1967).

The target was mounted inside a 60 cm.-diameter scattering chamber and aligned optically with the beam axis. Three silicon particle-detectors, one fixed at 90° and the others movable from 35° to 162°, viewed the gas through 0.5 mg/cm^2 thick mylar foil windows. The solid angles of the detectors were defined by two sets of rectangular slits which allowed an average angular spread of ± 4°. At all angles investigated, the counters viewed only the target gas and the mylar foil windows on both sides of the target so that scattering from the walls of the target cell was reduced. The beam left the target

cell through a 2 mg/cm^2 Havar foil at the end of a 10 cm long extension tube and was collected in a Faraday cup.

The entrance canals were 3.5 and 3.2 mm in diameter and the second canal was threaded to minimize scattering. With natural neon target gas, a pressure of 3 Torr was maintained for a gas flow rate of about 3 liters (STP) per hour. The pressure in the section of the vacuum system immediately above the 1200 liter/sec diffusion pump was about 6×10^{-4} Torr. The maximum target thickness, which occurred at the 162° counter position, was 700 eV, and the Doppler effect at 30°C contributes an additional energy spread of 300 eV FWHM. The energy loss before entering the observable region of the gas target was estimated to be less than 500 keV.

Slit openings of 1.2 mm were used at the object and image of the 90° analyzing magnet with resultant beam energy spreads as low as 2 keV FWHM. The corona stabilizer gain was set to minimize the voltage fluctuations of the accelerator terminal, as displayed by the calibrated signal from a capacitive pick-up plate. To obtain better energy resolution for the observation of the scattering anomaly corresponding to the lowest T = 3/2 level, whose observed width was 2.1 keV, a variable compensation voltage was applied to the insulated target chamber. An energy error signal was taken from the image slits of the 90° analyzing magnet and used to control a $\pm$ 2 keV variable power supply connected to the target chamber. The gain of this compensation system was adjusted to correspond to the voltage fluctuations of the accelerator terminal as observed by the pick-up plate. With this energy-compensation system the observed width of the lowest

T = 3/2 level was reduced to 1.5 keV.

Energy spectra from the three detectors were routed to three quadrants of an RIDL 400 channel analyzer. A computer program was used to sum the counts in the regions of interest of the spectra and to plot them as a function of incident energy.

2. Excitation Functions and Angular Distributions

The energy range from 6.76 to 7.33 MeV (lab) was surveyed in steps of 2 keV with detectors at 90^{o}, 142^{o} and 162^{o} (lab). The scattering yields were recorded simultaneously at the three angles, in order to improve the chance of detecting a narrow resonance. Subsequently, the energy range was surveyed with detectors at 90^{o}, 54^{o}, and 107^{o} (lab), using 2 keV steps in the region of the observed narrow resonances and 5 keV steps in the intervening regions. Finally, the two T = 3/2 resonances were examined at a total of 8 angles with energy steps of 1 keV.

Figure 12 shows a typical pulse height spectrum obtained at 35^{o} (lab). Clearly resolved groups corresponding to the ground and excited states of ^{20}Ne up to E_x = 4.97 MeV are seen, in addition to several groups resulting from the 10 percent natural abundance of ^{22}Ne. The rise in the spectra at low energies is due to neutron and gamma-ray background. Except at 162^{o}, the elastic scattering peak produced by ^{22}Ne could not be separated from that due to ^{20}Ne; all excitation functions of the elastically scattered protons thus include a small contribution from ^{22}Ne. However, all the anomalies

reported in this work were present in both the elastic and inelastic scattering, which confirms that they are produced by reactions on ^{20}Ne.

Angular distributions were also measured at four energies near the narrow resonances (6.862, 6.882, 7.109, and 7.145 MeV), in 10^{o} steps from 40^{o} to 150^{o} (lab). The absolute cross section was determined by comparison with the elastic scattering from xenon gas introduced into the target chamber. At the proton energy used, the scattering of protons by xenon follows the Rutherford scattering law to at least 70^{o}. The absolute error, which depends on the statistical accuracy of the number of counts recorded, and on the comparison of target pressures and charge integrations, is less than 20 percent.

C. Results

The elastic scattering yields at five angles, covering a range of excitation energies in ^{21}Na from 8.87 to 9.42 MeV, are presented in Figures 13 to 17. Only two of the anomalies observed in this range have widths less than 13 keV and they occur near the expected positions of the T = 3/2 levels as observed in the $^{19}F(^{3}He,n)$ reaction, which are indicated by horizontal bars in the figures. These two anomalies occur at incident proton energies of 6.872 ± 0.005 and 7.128 ± 0.005 MeV and have observed widths of 2.1 and 3.8 keV respectively. These incident energies correspond to excitation energies in ^{21}Na of 8.973 ± 0.007 and 9.217 ± 0.007 MeV when combined with the recent value of 2.432 ± 0.005 MeV for the proton binding energy in ^{21}Na due to Bloch et al. (1967).

These anomalies are most easily observable in the elastic scattering at 163^{o}, where the non-resonant background is a minimum, and do not show up as strongly in the yields of protons to the 1.63 (p_1), 4.25 (p_2) and 4.97 (p_3) MeV levels of ^{20}Ne, as may be seen in Figures 18, 19 and 20. The 8.97-MeV level shows small effects in the p_1 and p_3 channels, whereas the 9.22-MeV level does not appear to resonate in the p_2 or p_3 channels although it does show up in the p_1 channel. The proton yields in the p_1 and p_2 channels at 163^{o} are presented in Figure 21 for the entire energy range.

A total of six levels with widths greater than 13 keV were observed in the elastic or inelastic yields in the energy range covered. These are all assumed to be T = 1/2 levels and their excitation energies are presented in Table 2, together with their observed widths, determined from the data for the reaction channel and angle which best exhibited a Breit-Wigner resonance shape.

D. Analysis

In order to determine the spins and parities, and partial widths of the T = 3/2 levels, calculations were performed using a single-level approximation, in an attempt to fit the elastic scattering data.

The cross sections for elastic scattering of protons from a spin zero target may be written (Feshbach 1960) as:

$$\frac{d\sigma(\theta)}{d\Omega cm} = |A|^2 + |B|^2 \qquad (3\text{-}1)$$

where

$$A = f_c(\theta) + \frac{1}{2ik} \sum_{\ell=0}^{\infty} e^{2i(\omega_\ell - \omega_o)} [(\ell+1)(U_\ell^+ - 1) + \ell(U_\ell^- - 1)] P_\ell (\cos \theta),$$

$$B = \frac{1}{2ik} \sum_{\ell=1}^{\infty} e^{2i(\omega_\ell - \omega_o)} [U_\ell^+ - U_\ell^-],$$

$$f_c = \frac{-\eta}{2k \sin^2(\theta/2)} \exp [- i\eta \ln \sin^2(\theta/2)],$$

$$\omega_\ell - \omega_o = \sum_{n=1}^{\ell} \tan^{-1} (\eta/n),$$

where θ is the center-of-mass scattering angle, $\eta = Z_1 Z_2 e^2/\hbar v$ where v is the relative velocity in the center-of-mass system, k is the wave number, and the $U_\ell^{\pm}$ represent the elements of the collision matrix for collisions with total angular momentum $J = \ell \pm 1/2$.

For the case in question, where there are reaction channels open, the collision matrix may be expressed in terms of complex phase shifts $\delta_\ell^{\pm}$:

$$U_\ell^{\pm} = e^{2i\delta_\ell^{\pm}}$$

or

$$U_\ell^{\pm} = A_\ell^{\pm} e^{2i\triangle_\ell^{\pm}} ; \quad 0 \leq A_\ell^{\pm} \leq 1 \text{ and } \triangle_\ell^{\pm} = \text{real}.$$

The A_ℓ coefficients take into account the absorption of flux from the entrance channel.

On the assumption that the observed narrow anomalies are produced by a single level, it is possible to express the collision matrix for the resonant partial wave in terms of a non-resonant background and a resonant term (see Lane and Thomas 1958):

$$u_{\ell}^{\pm} = \left(e^{2i\delta_{\ell\pm}}\right) \left[1 - \frac{i\Gamma_{p_o}}{E-E_o + i\Gamma/2}\right]$$

where $\delta_{\ell\pm}$ are the non-resonant background phase shifts, E_o is the resonant energy, Γ is the total width of the resonance and Γ_{p_o} is the partial width for decay to the ground state of ^{20}Ne. In terms of R matrix theory, this parametrization amounts to the assumption that the penetrability and shift functions are constant over the width of the resonance, which is a good approximation for the narrow levels in question. In the following discussion all energies and widths are in the center-of-mass system unless otherwise stated.

The method of analysis used was as follows:

1. Non-resonant background phase shifts $\delta_{\ell\pm}$ were chosen to fit the observed angular distributions near the resonances.
2. Resonance shapes were calculated with typical background phase shifts for all values of J^{π} corresponding to $\ell \leq 4$ for $\theta_{cm} = 55^{o}$, 93^{o}, 143^{o}, 163^{o}.
3. These shapes were compared with the observed resonances and appropriate values of J^{π} were selected.
4. Values of E_o, Γ and Γ_{p_o} were determined by careful comparison of calculated and observed resonance shapes at all angles, taking into account the effects of energy resolution.

The measured angular distributions near the T = 3/2 levels are presented in Figure 22. In order to restrict the number of free parameters available to fit the data, the initial phase shifts were restricted to be real ($A_{\ell}^{\pm} = 1$), dependent only on ℓ ($\delta_{\ell}^{+} = \delta_{\ell}^{-}$), and phase shifts for $\ell \geq 4$ were excluded.

A computer program in Citran language was written for the IBM 360-50 computer to calculate off-resonance angular distributions for various values of the phase shifts. As the remote console facility permitted direct access to the computer, the phases could be conveniently varied until acceptable fits were obtained for the angular distributions. The angular distributions which were calculated from the final values of δ_ℓ listed in Table 3,A are presented as solid lines in Figure 22.

To calculate resonance shapes a computer program due to Goosman (1967) was used which evaluates equation 3-1 for ℓ dependent phase shifts and appropriate values of E_o, Γ, Γ_{p_o}, and averages the result with a gaussian resolution function with FWHM = R to approximate the experimental resolution.

Resonance shapes calculated for phase shifts near the final accepted values are presented in Figure 23 for all $\ell \leq 4$. The anomaly shapes at the smaller angles (55^o, 93^o) are not as significantly affected by changes in the background phase shifts (δ_ℓ) as are the shapes at 143^o and 163^o. The reason is that the Coulomb scattering term (f_c) in $\frac{d\sigma}{d\Omega}$ contributes the major portion of the background scattering at angles less than about 90^o, whereas at the larger angles the background is predominantly due to the nuclear scattering terms, containing the δ_ℓ, and is very sensitive to them. However, a comparison of the 55^o and 93^o shapes in Figure 23 with the observed anomalies presented in Figures 13 and 14 is sufficient to establish the spin-parity of the 9.22 MeV level as $1/2^+$ and to strongly suggest that the 8.97 MeV level has spin-parity $3/2^+$ or $5/2^+$. The calculated $1/2^+$

shapes are the only ones to have a strong rise at 55^{o} and strong dip at 93^{o} as observed for the 9.22 MeV level. The 8.97 MeV level has a small rising anomaly at 55^{o} and a dip at 93^{o}, similar to the $3/2^{+}$ and $5/2^{+}$ shapes, but an investigation of anomaly sizes is necessary before the $1/2^{+}$ shapes can be ruled out.

Detailed elastic scattering excitation functions at 8 angles for the two T = 3/2 resonances are presented in Figures 24 and 25.

The experimental energy resolution R for this data was determined from a comparison of the anomalies for the 8.97 MeV level at 143^{o} and 163^{o} with those obtained when the target compensation voltage was used, which are presented in Figure 26. The minimum possible R, resulting from energy loss and Doppler effect in the target is about 0.7 keV. The solid lines in Figure 26 show the fit to the data obtained with R = 0.7 keV, Γ = 1.2 keV, and Γ_{p_o} = 0.15 keV. This sets an upper limit of 1.2 keV for Γ so that the observed width of 2.1 keV for the data presented in Figure 24 is predominantly due to the experimental resolution. Values of R in the range 2.0 ± 0.1 keV provide acceptable fits to this data for all $\Gamma < 1.2$ keV and a value of R = 2 keV was used in the analysis for both of the T = 3/2 levels.

The solid lines in Figure 24 are the shapes calculated for the 8.97-MeV level with $J^{\pi} = 5/2^{+}$, Γ = 0.5 keV and Γ_{p_o} = 0.1 keV, using the background phases tabulated in Table 3A. The quality of the fits at all angles establishes the ℓ value of the resonance to be 2,

although it is not possible to distinguish between $J^{\pi} = 3/2^{+}$ and $5/2^{+}$. Curves for $J^{\pi} = 1/2^{+}$ exhibited anomalies which were the wrong shape at 123^{o} and 143^{o} and did not have the correct relative sizes at other angles, thus eliminating this possible choice of spin-parity.

To test the sensitivity of the shapes to the parameters Γ and Γ_{p}, calculations were performed for $\Gamma_{p_o} = 0.1$ keV, $J^{\pi} = 5/2^{+}$ with various values of Γ between 0.1 and 1.2 keV. It was found that the sizes of the anomalies were not strongly dependent on Γ except for the two extremes of this region.

For anomalies which are Breit-Wigner shaped, such as those at 143^{o} and 163^{o}, the height of the anomaly is roughly proportional to Γ_{p_o}/Γ (for $\Gamma_{p_o}/\Gamma \ll 1$) and its width is proportional to Γ. Therefore, its area, which is the quantity determining the anomaly size after averaging with resolution $R \gg \Gamma$, is approximately proportional to Γ_{p_o}. The validity of the two approximations ($\Gamma_{p_o}/\Gamma \ll 1$ and $R \gg \Gamma$) breaks down near the ends of the investigated range of Γ, but the calculations give a reasonable fit to the data for 0.3 keV $\leqslant \Gamma \leqslant$ 0.9 keV with $\Gamma_{p_o} = 0.1$ keV and R = 2 keV. Acceptable fits were also obtained for $\Gamma = \Gamma_{p_o} = 0.05$ keV, R = 2.1 keV and for Γ = 1.2 keV, $\Gamma_{p_o} = 0.15$ keV, R = 1.9 keV. On this basis, Γ_{p_o} was determined to be 0.1 ± 0.05 keV.

The results obtained for the 9.22 MeV level with Γ = 2.3 keV, $\Gamma_{p_o} = 1.1$ keV and R = 2 keV, using the real, ℓ-dependent phase shifts listed in Table 3A, are presented in Figure 25. The calculations match the data reasonably well for all angles $\theta \leqslant 123^{o}$ but are too large at 143^{o} and do not reproduce the anomaly shapes at 153^{o} and 163^{o}.

As no other $J < 7/2$ produced the correct anomaly shapes at as many angles, and as the discrepancy occurred at the largest angles where the results were most sensitive to background phase shifts, it was concluded that the background phase shifts were the source of the error. Attempts were made to find other phase shifts which would fit the observed angular distribution and produce the correct anomaly shapes for $\theta > 123^{o}$. Although a number of other sets of real, ℓ-dependent phase shifts were found which produced similar angular distributions and different anomaly shapes for $\theta > 123^{o}$, none of them reproduced the experimentally observed anomalies. At this point the restrictions on the background phase shifts were removed, and a fit to the background angular distribution was attempted with complex, J-dependent phase shifts for $\ell \leq 2$. This analysis was performed by Dr. M. J. Levine at Brookhaven National Laboratory using a nonlinear least squares fitting routine written by Birnbaum (1965) and utilized by Levine (1968). The angular distribution which was calculated from the resultant values of $\delta_{\ell}^{\pm}$ listed in Table 3, B is presented as a dashed line in Figure 22.

Goosman's computer program was modified to accept J-dependent phase shifts, and used to calculate anomaly shapes with the new background phase shifts and the same values of Γ_{p_o} and R. These shapes are presented as dashed curves in Figure 25, and may be seen to be very similar to the solid curves at angles $\theta \leq 123^{o}$, but they represent the data better at the larger angles than the solid curves do.

As the values of Γ and Γ_{p_o} necessary to fit the data at most angles are the same for both sets of background phase shifts, Γ and Γ_{p_o} appear to be well determined. The values are: $\Gamma = 2.3 \pm 0.5$ keV and $\Gamma_{p_o} = 1.1 \pm 0.3$ keV. The errors have been estimated from the variation of anomaly sizes observed for changes in these parameters.

The difference in the character of the non-resonant phase shifts necessary to describe the background at the positions of the two T = 3/2 levels is somewhat disturbing. However, although the background does not change significantly over the widths of these narrow resonances, it does change considerably between them, due to the presence of the T = 1/2 resonances (see Figures 13 to 17). In any case, the possibility always exists that other sets of background phase shifts would also fit the angular distributions. For this reason, the accuracy of the Γ_{p_o} parameter rests primarily on the fits obtained in the region $\theta \leq 123^o$, where the anomaly shapes are least sensitive to the choice of background phase shifts.

No analysis was attempted for the inelastic scattering data. The 8.97-MeV level exhibits small anomalies in the p_o, p_1, and p_3 channels, whereas the 9.22 MeV level shows anomalies only in the p_o and p_1 channel. Transitions from the 9.22 MeV level to higher levels in ^{20}Ne and to $\alpha + {}^{17}$F(0.0) or $\alpha + {}^{17}$F(0.50) are inhibited by the Coulomb barrier, as may be seen from Table 4, which lists the penetrabilities calculated from $P_\ell = \frac{\rho}{F_\ell^2 + G_\ell^2}$, where F_ℓ and G_ℓ are the regular and irregular Coulomb functions and $\rho = kr$. Thus, it is

likely that Γ_{p_1} makes up most of the remainder of the width of the 9.22 MeV level, so $\Gamma_{p_1} \approx 1.2$ keV.

For the 8.97-MeV level, the ratio $\Gamma_{p_1}/\Gamma_{p_o}$ can be calculated from the energy spectrum of delayed protons following the β^+ decay of ^{21}Mg, presented by Hardy and Bell (1965). The calculation is complicated by the presence of contaminant groups due to delayed protons following the β^+ decay of ^{17}Ne, but a value $\Gamma_{p_1}/\Gamma_{p_o} = 2.5 \pm 0.6$ can be obtained after subtracting the contributions from the contaminant. Combining this number, and the present results for Γ_{p_o}, we obtain $\Gamma_{p_1} = 0.25 \pm 0.15$ keV.

The T = 1/2 levels in the observed energy range overlapped to such an extent that a single level approximation was not considered to be justified and no analysis was attempted for them.

E. Conclusions

In summary, the lowest two T = 3/2 levels in ^{21}Na were observed in the ^{20}Ne(p,p) and (p,p') reactions at excitation energies of 8.973 ± 0.007 MeV and 9.217 ± 0.007 MeV. From an analysis of the elastic scattering data the following parameters were extracted: for the 8.973 MeV state, $J^\pi = 5/2^+$ (or $3/2^+$), $\Gamma < 1.2$ keV, $\Gamma_{p_o} = 0.1 \pm 0.05$ keV and for the 9.217 MeV state, $J^\pi = 1/2^+$, $\Gamma = 2.3 \pm 0.5$ keV, $\Gamma_{p_o} = 1.1 \pm 0.3$ keV.

These results agree with, and are more accurate than, those obtained from the ^{19}F(^{3}He,n) reaction presented in Section II. By comparing the two reactions, one can readily see the selectivity

with which the (^{3}He,n) reaction populates the T = 3/2 levels in the presence of a large number of T = 1/2 levels.

The results obtained for the excitation energy of the lowest T = 3/2 level do not agree with the measurement by McPherson et al. (1965), of 8.90 ± 0.04 MeV nor with the results of Butler et al. (1968), 8.92 ± 0.03 MeV. This latter result has been recently revised to 8.97 ± 0.03 MeV (Brunnader et al. 1969) and is now in good agreement with the present results.

These levels have recently been seen as resonances in the ^{20}Ne(p,γ) reaction by Bearse et al. (1969). The observed branching ratios are in agreement with the assumption, that these levels are members of a K = 1/2 rotational band (Nilsson orbit number 6) with $J^{\pi} = 5/2^{+}$ and $1/2^{+}$, as discussed in Section II.

The ^{21}Na(T = 3/2) mass may be combined with the observed masses of the other members of the 3/2 multiplet to test the validity of the quadratic mass law. The most accurately determined values of these mass excesses are presented in Table 5 for the two lowest T = 3/2 levels. The ^{21}F ground state mass excess comes from Mattauch et al. (1965), and the excited state mass is the average of the results of Hinds et al. (1962), and Horvat (1964). The ^{21}Ne mass excesses are the results of Hensley (1969a) which are significantly more accurate than other determinations for ^{21}Ne. The ^{21}Na masses are from the present work, combined with the mass of ^{20}Ne obtained from Mattauch et al. (1965). The mass of ^{21}Mg is a recent result from Cerny (1969) which was obtained in a remeasurement of the result obtained by Butler et al. (1968), using the ^{24}Mg(^{3}He,^{6}He)

reaction. Butler et al. (1968), observed both the ground state of ^{21}Mg, with a mass excess of 10.62 ± 0.12 MeV and a first excited state at 0.22 ± 0.030 MeV, but the count rate from this very difficult experiment was so low that the statistical precision of the data was low. In the remeasurement, only one peak was observed, which is assumed to correspond to the ground state of ^{21}Mg (Hardy 1969c).

If the quadratic mass equation is fitted by least squares to the masses in Table 5 a chi-square value of 6×10^{-3} is obtained, which corresponds to a 94 percent statistical probability. Alternatively, if a cubic term dT_z^3 is added to the equation, d is determined to be -1.66 ± 20.5 keV. Deviations from the quadratic mass equation due to higher order perturbations are expected to be such that $|\frac{d}{c}| \lesssim \bar{Z}\,\alpha$ where $\bar{Z}$ is the average nuclear charge of the multiplet, and α is the fine structure constant. For this case, $c\bar{Z}\alpha$ = 19 ± 2.3 keV, which is about the same size as the error in d.

Another way to compare the masses in the T = 3/2 quartet is to use the mass excesses of ^{21}F, ^{21}Ne and ^{21}Na and the quadratic equation to predict the mass excess of ^{21}Mg; one obtains the equation:

$$M(^{21}\text{Mg}) = 3\,[M(^{21}\text{Na}) - M(^{21}\text{Ne})] + M(^{21}\text{F})$$

which predicts $M(^{21}\text{Mg})$ = 10.940 ± 0.029 MeV. Although the experimental result, 10.95 ± 0.12 MeV, is extremely close to this prediction, the error is as yet too large to provide a significant test of the quadratic mass equation.

The ^{21}Na (T = 3/2) masses from the present work have been used in a systematic investigation of displacement energies throughout the ($1d_{5/2}$) shell (Hardy 1969a). Formulae, calculated by including the Coulomb interaction to first order, for two limiting coupling schemes (Hecht 1967 and 1968), are expressed in terms of five parameters which are determined by a fit to the experimental data. The resultant fits, with 17 and 19 degrees of freedom, are reasonably good, as were other such fits in the (1p) and (1f) shells based on the same formulae (Jänecke 1968 and 1969).

The two-body Coulomb matrix elements, determined from the semi-empirical parameters, were in reasonable agreement with values calculated using harmonic oscillator wave functions. However, the simplifying assumptions underlying the theoretical equations did not permit the extraction of further information about other possible charge dependent interactions.

The narrow widths observed for the ^{21}Na (T = 3/2) levels suggest that the wave functions for these levels do not contain large isospin impurities. The striking differences observed in the isospin impurities of mirror T = 3/2 levels in A = 13 and 17, to be discussed in Section IV, suggest that an experimental study of the widths and decay properties of the corresponding T = 3/2 levels of ^{21}Ne would be very interesting. A search for these levels as isospin-forbidden resonances in the ^{17}O + α reaction might be difficult, since they would be expected to occur at incident alpha particle energies of about 2 MeV, which are below the Coulomb barrier. It appears that the reactions most likely to yield information about the decay

properties of these levels would be $^{22}Ne(^{3}He,\alpha)^{21}Ne^{*}$ (n) ^{20}Ne and $^{21}Ne(^{3}He,\alpha)^{21}Ne^{*}(\alpha)^{17}O$, using experimental methods similar to those described in Section IV.

IV. ISOSPIN-FORBIDDEN PARTICLE DECAYS OF THE LOWEST T = 3/2 LEVELS OF ^{17}O AND ^{17}F

A. Introduction

Recent measurements in this lab by Adelberger, Cocke, Davids, and the author (Adelberger et al. 1969a) have revealed quite striking differences in the isospin-forbidden particle decay properties of the lowest T = 3/2 levels in ^{13}C and ^{13}N.

The results of these studies are reproduced in Table 6 together with recent theoretical calculations by Arima and Yoshida (1969) which include isospin mixing due to the Coulomb interaction.

The magnitude of the effects in the mass-13 case and the apparent inadequacy of the theoretical explanation on the basis of Coulomb mixing alone, stimulated a similar study of the isospin-forbidden decays of the T = 3/2 levels in ^{17}O and ^{17}F to gain further information about the character of isospin impurities in higher-isospin levels.

The T = 3/2 levels of the mass 17 multiplet have been extensively studied in isospin-allowed reactions such as (t,p), (^{3}He,p), (^{3}He,α) and (^{3}He,n). Twenty-one levels in ^{17}N have been observed in the ^{15}N(t,p) reaction (Hart et al. 1965) and the ground state has been assigned $J^\pi = 1/2^-$ (Silbert and Hopkins 1964). Hensley (1969a) has reported the lowest T = 3/2 level in ^{17}O at an excitation energy of 11.075 ± 0.004 MeV and six other T = 3/2 levels seen in the $^{15}N(^3He,p)$ and $^{18}O(^3He,\alpha)$ reactions. Detraz and Duhm

(1969) have also observed these levels and an additional one at 15.101 MeV excitation, in the $^{18}O(^{3}He,\alpha)$ reaction. Adelberger and Barnes (1966) have observed the lowest T = 3/2 level in ^{17}F at an excitation energy of 11.195 ± 0.007 MeV and two other T = 3/2 levels, in the $^{15}N(^{3}He,n)^{17}F$ reaction.

These T = 3/2 levels in ^{17}F have also been reported as isospin-forbidden resonances in the $^{16}O(p,p)$ reaction (Patterson et al. 1967 and Temmer et al. 1967) and the lowest level has been found to have a width less than 1.2 keV. The spin and parity of the lowest T = 3/2 levels in ^{17}O and ^{17}F have been determined in all these reactions to be $1/2^{-}$. ^{17}Ne has also been studied (Hardy and Bell 1965; Braid et al. 1965; Esterlund et al. 1967) and recently the branching ratios for isospin-forbidden proton decays of the lowest T = 3/2 level in ^{17}F have been determined from the delayed-proton energy spectrum following the superallowed beta decay of ^{17}Ne (Hardy et al. 1969b).

Since the total widths of the lowest T = 3/2 levels in ^{17}O and ^{17}F have not been accurately determined, it was necessary to measure the branching ratios for decay to the ground state and to excited states of ^{16}O, so that ratios of reduced widths for the T = 3/2 two levels could be compared. In addition, the comparison of such ratios of reduced widths imposes restrictions on the form of isospin impurities in the T = 3/2 levels involved, as has already been pointed out in the A = 13 case (Adelberger et al. 1969a) and will be discussed in Section IV, D.

With these motivations, experiments were undertaken to determine the branching ratios for the proton decay of the lowest T = 3/2 level in ^{17}F(11.195 MeV) to the ground state and the 6.05 and 6.13 MeV levels of ^{16}O and for the neutron decay of the analogous T = 3/2 level in ^{17}O(11.075) to the same levels of ^{16}O.

These transitions are indicated on an isobar diagram in Figure 27.

B. Proton Decay of the Lowest T = 3/2 Level in ^{17}F

1. Apparatus

In order to measure the branching ratios (B.R.'s) for proton decay of the lowest T = 3/2 level in ^{17}F, the level was populated with the $^{15}N(^{3}He,n)^{17}F^{*}(p)^{16}O$ reaction, and the decay protons were detected in coincidence with the neutrons.

The neutron detector used was the same one described in Section II and slow channel energy discrimination was set as described there; hence the detector efficiency was as shown in Figure 3. Protons were detected by a 1000μ, silicon surface barrier detector mounted in a cylindrical brass scattering chamber of wall thickness 1/8", together with the ^{15}N gas cell.

The gas cell was designed so that the proton and neutron detectors both observed the total volume of interaction between the beam and target gas, as shown in Figure 28. The wall thickness of the stainless steel gas cell was 3/32" and the back of it was 0.02" tantalum to reduce the background counting rate. The beam entered

the cell through a 10,000 Å circular nickel foil which was offset from the axis of the gas cell, so that the proton detector could observe the total volume of interaction, as shown in Figure 28.

The 10,000 Å Ni foils were mounted on 0.02" tantalum frames with epoxy resin, and the frames were then attached to the gas cell. Foils which were "sandwiched" in this manner were found to be more reliable under bombardment and could withstand higher gas pressures than those which were simply glued to the front of the gas cell.

The beam passed through two collimators which restricted its diameter to 1/8" to reduce uncertainty in the solid angle subtended by the proton detector. The solid angle was defined by a rectangular opening whose dimensions were measured with a traveling microscope. The distance from the detector to the center of the gas cell was carefully measured with a ruler, and was estimated to be 0.81 ± 0.02" from a series of independent measurements. The resultant solid angle was $(1.71 \pm 0.2) \times 10^{-3}$ steradians, where the error includes the effect of the finite size of the beam spot.

Aluminum foil, 2.25 mil thick, was placed before the proton detector to stop elastically scattered ^{3}He particles.

The population of the lowest T = 3/2 level in ^{17}F by the $^{15}N(^{3}He,n)$ reaction was determined by observing a neutron time-of-flight spectrum, using a pulsed beam as described in Section II.

The apparatus used to measure neutron-proton coincidence is illustrated in Figure 29. Timing signals from the neutron detector were fed to the START side of an Ortec Model 437 time-to-amplitude converter (TAC). STOP pulses were derived from the silicon detector

by means of an Ortec Model 260 time pickoff circuit. The output of the TAC was fed to the Y axis of a 64 × 64 Nuclear Data multichannel analyzer, and the linear output of the silicon detector was amplified and fed to the X axis. In the following discussion, the Y axis will be referred to as the neutron axis and the X axis as the proton axis.

A linear signal, derived from dynode 11 of the photomultiplier was inspected by a discriminator. The discriminator level was set to eliminate phototube noise and small scintillator pulses which would have poor time resolution. Coincidences between the output of this discriminator and pulses from the TAC which fell in the 64 channels of interest on the neutron axis were used to gate the multichannel analyzer.

In this manner, two dimensional spectra of neutron flight time versus proton energy were accumulated, as illustrated in Figure 30.

In this figure neutron flight time increases from bottom to top, and proton energy from left to right. Gamma rays, which are also detected by the scintillator, have the shortest flight times, and produce a curve at the bottom of the figure. The deviation of this curve from a straight line is an indication of the variation of triggering time with pulse height from the proton detector, and its width is a measure of the overall time resolution. The midpoint of this curve is assumed to correspond to 3.3 ns/m, which then allows the zero point of the time scale to be determined without further corrections for the time-slewing of the proton detector. The time scale can then be calibrated from the separation of the neutron peak corresponding to the

lowest T = 3/2 state in ^{17}F from the gamma ray peak, in the pulsed-beam singles spectrum. The proton energy scale can be calibrated from the proton and deuteron peaks corresponding to known energy levels in ^{17}O and ^{16}O, after making the appropriate correction for energy loss in the aluminum foil.

The other curves which can be seen in the spectrum are the loci of allowed proton energies versus neutron flight times for the two cases where ^{16}O is left in its ground state, or in one of its first excited states at 6.05 and 6.13 MeV which are not resolved. These loci will be referred to as kinematic lines.

The decay of levels in ^{17}O or ^{17}F to these states in ^{16}O should be indicated by enhancements in the number of counts on the kinematic line, at the proton energy or neutron flight time appropriate to the population of the level in the primary (^{3}He,p) or (^{3}He,n) reaction.

To display the data and exhibit these enhancements more clearly, a number of channels in the proton (neutron) direction, centered on the kinematic line, are summed at each neutron (proton) channel and the results are displayed as a one dimensional spectrum of counts versus neutron (proton) channel number. A computer program was developed to process the data and provide such projections of kinematic lines on either the neutron or proton axis.

The background due to chance coincidences is uniform along the neutron flight time axis, but reflects the variation of count rate with particle energy on the other axis. The region of the spectrum between the gamma ray peak and the ground state kinematic

line should contain only chance coincident events and the average number of chance counts in each proton channel is determined from this region. The appropriate chance coincidence background is then subtracted from the entire spectrum by the computer. The positions of the kinematic lines are determined from the time scale and proton energy calibrations, incident energy, Q-values, particle masses, detector angles and neutron counter distance, and the calculated positions of the kinematic lines are indicated on the print-out of the spectrum for comparison with the observed lines.

In order to obtain the relative normalization of the coincidence spectra and the pulsed-beam singles spectra, the proton energy spectrum was simultaneously recorded in an RIDL 200 channel analyzer. The number of counts accumulated in an isolated peak produced by the $^{15}N(^{3}He,d_{o})^{16}O(0.0)$ reaction could be accurately determined for both runs, and served as a measure of the number of beam-target interactions, independent of beam fluctuations and gas pressure changes. A single channel analyzer was also set to cover this peak and its output was counted by a short dead-time scalar in order to provide a check on the loss of counts due to the larger dead-time of the multichannel analyzer.

2. Experimental Method

Since the lowest T = 3/2 level in ^{17}F has spin 1/2, its decay angular distributions are isotropic in the center of mass coordinate frame, and a measurement at one angle suffices to determine its branching ratio.

The main problem in the determination of the branching ratio is the identification of those enhancements on the kinematic lines of the coincidence spectrum, which can be unambiguously attributed to the decay of the ^{17}F level. There are two other ways in which genuine coincidence counts can be produced on the kinematic line:

1. From the reaction $^{15}N(^{3}He,np)^{16}O$, which does not proceed through a definite intermediate state, and may be assumed to have a smoothly varying cross section with neutron or proton energy.
2. From the reaction $^{15}N(^{3}He,p)^{17}O^{*}(n)^{16}O$ if there happens to be a state populated in ^{17}O within the appropriate energy range.

For this reason, it is necessary to have the greatest possible population of the ^{17}F (T = 3/2) level, together with good time resolution, and if possible, to choose the incident energy and the detector angles so that there are no ^{17}O energy levels which could produce enhancements at the same place on the kinematic line.

A computer program was written which calculated and plotted kinematic lines as a function of neutron flight time and proton energy, as well as marking the positions of the known energy levels of ^{17}F and ^{17}O on the kinematic line. The useable range of incident energies was chosen from previous investigations of the population of the T = 3/2 level by the $^{15}N(^{3}He,n)$ reaction (Adelberger et al. 1969).

The neutron detector angle was chosen to be 0^{o} since the angular distribution for the $(^{3}He,n)$ reaction is strongly forward peaked, and the detector was placed 1.5 meters from the target as a

compromise between good time resolution and reasonable solid angle.

Incident energies and proton detector angles were chosen so that the decay of the lowest T = 3/2 level of ^{17}F to the ground state of ^{16}O produced an enhancement on the kinematic line which lay between enhancements due to levels in ^{17}O at 4.55 and 5.08 MeV and could be resolved from them. The projection on the neutron axis of the kinematic line for this case is shown in Part (b) of Figure 31 and the enchancement resulting from the decay of the $^{17}F(T = 3/2)$ level is indicated by an arrow. Part (a) of the figure illustrates the spectrum obtained from a pulsed-beam, single-counting measurement of the $(^3He,n)$ reaction on ^{15}N, at the same incident energy, detector angle, and time scale, and the enhancement in Figure 31 (b) can be seen to appear at the same flight time as the peak due to the T = 3/2 level.

Three other coincidence and singles spectra were taken at an incident energy of 8.25 MeV and angles of 90^o, 110^o, and 120^o. The ^{17}F enhancement was observed at the correct neutron energy in all runs and was found to be isotropic within the errors.

For decays of the $^{17}F(T = 3/2)$ level to the 6.05 and 6.13 MeV levels of ^{16}O, the density of interfering ^{17}O levels is quite high, so that it is impossible to resolve the ^{17}F (T = 3/2) decays from them. However, it is found that the levels are so dense as to produce a rather uniform background upon which the ^{17}F enhancement appears. This is illustrated in Figure 32 which shows the projection on the neutron axis of the kinematic line corresponding to the 6.05 and 6.13 MeV levels of ^{16}O. Parts a, b, and c correspond

to ^{3}He incident energies of 9.18, 9.03 and 8.93 MeV, respectively. Enhancements due to the neutron decay of levels in ^{17}O are expected to occur at a constant neutron flight time, determined by the energy available for the ^{17}O decay, and the ^{17}O center of mass energy, which is not strongly dependent on the beam energy. On the other hand, enhancements due to the proton decay of the ^{17}F (T = 3/2) level occur at a neutron flight time appropriate to the $^{15}N(^{3}He,n)$ $^{17}F(11.195)$ reaction, and have different flight times at the three different incident energies. Two peaks may be observed in the spectra, one of which remains fixed at a position corresponding to a level in ^{17}O at 11.6 MeV. The other has a centroid which occurs at the expected position of the ^{17}F (T = 3/2) level as determined from pulsed-beam, single-counting spectra at the three energies and is assumed to be an enhancement due to the proton decay of the $^{17}F(T = 3/2)$ level.

The number of counts in the peaks was determined for runs (b) and (c) and a linear background was subtracted, as shown in the figure. The branching ratios could then be calculated as:

$$\text{B.R. } (\%) = \frac{N_p \times \text{C.M.F.} \times 4\pi \times N_{mon}\ (\text{SING.})}{N_n \times \Omega_p \times N_{mon}\ (\text{COINC.})}$$

where $N_p \equiv$ number of counts in enhancement on kinematic line,

$N_n \equiv$ number of neutrons in T = 3/2 peak in singles spectrum,

$\text{C.M.F.} \equiv d\Omega_{LAB}/d\Omega_{CM}$,

$\Omega_p \equiv$ solid angle subtended by the proton detector (steradians),

N_{mon}(COINC.) = number of counts in the d_o peak in the coincidence run,

N_{mon}(SING.) = number of counts in the d_o peak in the singles run.

3. Branching Ratios

The ground state branching ratio was determined from five separate coincidence spectra and associated singles spectra. The results are listed in Table 7A.

The errors in each run are the square root of the sum of the squares of contributions from the following sources:

1. Statistical errors in the number of counts within the peak region including the error due to subtraction of the chance coincidence background.
2. The error due to uncertainty in the background under the enhancement on the kinematic line.
3. The error in the solid angle subtended by the proton detector, including the effect of the finite size of the beam spot.
4. Errors due to incorrect counting of the number of counts in the d_o monitor peak. The number of counts contained within the monitor peak in the RIDL analyzer was found to correspond with the number counted in the scaler, once a correction was made for the dead time of the analyzer. However, at the count rates used in the proton counter for the coincidence runs (as high as 20×10^3 sec^{-1}) a small amount of pileup was observed to occur.

By observing the number of counts obtained in the d_o peak for a fixed total charge at various rates, it was estimated that about 5 % of the counts in the d_o peak were lost through pile-up. It was assumed that this effect would affect the T = 3/2 enhancement in the same way, and the number of counts in the d_o peak, above the flat background due to the pile-up, was taken as a measure of the total number of monitor counts for both the singles and coincidence runs. The error arising from this source is certainly less than 5 % and can therefore be neglected in comparison with errors such as 1 and 2.

The branching ratio to the combined 6.05 and 6.13 MeV states of ^{16}O was determined from the two coincidence runs (b) and (c) of Figure 31, and corresponding single-counting runs. The results and errors are listed in Table 7B.

C. Neutron Decay of the Lowest T = 3/2 Level in ^{17}O

1. The $^{15}N(^3He,p)^{17}O^*(n)^{16}O$ Reaction

An attempt was made to measure the neutron decays of the $^{17}O(11.075;\ T = 3/2)$ level from the $^{15}N(^3He,p)^{17}O^*(n)^{16}O$ reaction by methods similar to those described in Section IV,B. The proton detector was positioned at 0^o where the yield is a maximum in the $^{15}N(^3He,p)$ reaction, which populates the level (Hensley 1969a).

The gas cell which was used was a 1/2" diameter stainless steel cylinder with 1/16" wall thickness. The beam entered through a 10,000 Å nickel foil and the protons left the cell through a 2 mil

Cu foil, which was sufficiently thick to prevent the beam from reaching the detector. The resultant resolution in the proton detector was 250 keV full width at half maximum for the proton peak corresponding to the $^{17}O(11.075)$ level. The population of this level was difficult to determine from the silicon detector spectrum because of the poor resolution and the presence of peaks from other particles, such as deuterons. Therefore, the 24" magnetic spectrometer was used to determine the population of the $^{17}O(11.075)$ level, relative to the peak from the $^{15}N(^{3}He,d)^{16}O(7.12\ MeV)$ reaction. This latter peak was the most prominent feature in the silicon detector spectrum and could be compared with the d_o peak which had been monitored. A direct comparison was impossible as the energy of the d_o peak was above the range of the magnetic spectrometer.

The effect of the brass target chamber on neutron detection efficiency was determined by accumulating a spectrum from the $^{16}O(^{3}He,n)^{18}Ne$ reaction using the pulsed beam at 10 MeV and a thin-walled gas target. This spectrum was compared with one accumulated for the same integrated charge, with a 1/8" sheet of brass between the target and the neutron detector to simulate the effect of the target chamber walls. The spectrum contained five neutron groups with energies ranging from 1 to 7 MeV. The reduction in counts in each peak was 8 ± 1% due to the introduction of the brass absorber and it was assumed that the brass target chamber wall reduced the overall neutron detection efficiency by this amount.

To measure the branching ratios for the neutron decay, a series of neutron-proton coincidence spectra were taken at various incident energies and neutron angles. Figure 30 shows a typical two-dimensional coincidence spectrum. An enhancement on the ground state kinematic line can be observed at the expected position of the $^{17}O(T = 3/2)$ level.

Figure 33 shows projections on the neutron axis for the kinematic line corresponding to the 6.05 and 6.13 MeV states of ^{16}O. Enhancements due to the neutron decay of levels in ^{17}O are expected to occur at nearly the same neutron flight time, for each of the three incident energies illustrated. No such constant peak is observed with a centroid corresponding to the correct neutron flight time for the decay of the $^{17}O(11.075; T = 3/2)$ level to either the 6.05 or 6.13 MeV state of ^{16}O. However, a peak was observed which corresponds to the decay of a level in ^{17}O at 11.02 MeV to the 6.13 MeV level of ^{16}O, or of a 10.94 MeV level decaying to $^{16}O(6.05)$.

No such levels were previously reported in the $^{15}N(^{3}He,p)^{17}O$ reaction, nor were any other levels observed within 250 keV of the T = 3/2 level (Hensley 1969b). Because of this discrepancy, Hensley and Nettles undertook a re-examination of this region of the proton spectrum from the $^{15}N(^{3}He,p)$ reaction, with better resolution than was used in the original investigation (Hensley 1969a). The use of 5,000 Å nickel foils on the ^{15}N gas cell, (rather than 10,000 Å) as well as lower gas pressure, and a reduction of the entrance slits on the 24" magnetic spectrometer,

provided sufficient resolution to observe an ^{17}O level at 11.023 MeV, as shown in Figure 34(a). The presence of this level made it impossible to determine the B.R.'s of the ^{17}O(11.075; T = 3/2 level) accurately from the $^{15}N(^{3}He,p)^{17}O^{*}(n)^{16}O$ reaction, by the methods described previously, since the 11.023 and 11.075 MeV levels could not be resolved in the degraded spectrum of the proton detector.

Using data similar to those displayed in Figure 33, it was possible to set upper limits for the B.R. for decay of the ^{17}O(11.075;T = 3/2) level to the 6.05 and 6.13 MeV levels of ^{16}O of 10% and 15% , respectively.

The decay of the combination of the 11.075 and 11.023 MeV levels of ^{17}O to the ground state of ^{16}O was quite well determined from coincidence spectra similar to those shown in Figure 35. From a knowledge of the relative populations of these two levels in the $^{15}N(^{3}He,p)$ reaction it was possible to set a lower limit on the B.R. of ^{17}O(11.075) to ^{16}O(0.0) + n of 48%.

These numbers are so inaccurate that it was decided to try again to measure the neutron decays, using the $^{18}O(^{3}He,\alpha)^{17}O$ reaction which does not populate the ^{17}O(11.023;T = 1/2) level, but does populate the ^{17}O(11.075;T = 3/2) level.

2. The $^{18}O(^{3}He,\alpha)^{17}O^{*}(n)^{16}O$ Reaction

a. Apparatus

The $^{18}O(^{3}He,\alpha)^{17}O$ reaction is very selective in populating the 11.075;T = 3/2 level in ^{17}O as may be seen in Figure 34(b), which is a plot of α particle count rate versus NMR frequency

obtained with the CIT-ONR 24" magnetic spectrometer. The target used was a 1000 Å Ni foil which had been oxidized by heating in an $^{18}O_2$ atmosphere.

Hensley (1969a) determined that the width of this level is less than 20 keV, and has seen no evidence for population of the 11.023 MeV level by this reaction, even in high-resolution spectra. This feature makes the $^{18}O(^3He,\alpha)^{17}O^*(n)^{16}O$ reaction a suitable choice for studying the neutron decays of the lowest T = 3/2 level in ^{17}O, without interference from T = 1/2 levels.

The differential cross section of the $^{18}O(^3He,\alpha)$ reaction populating the $^{17}O(11.075;T = 3/2)$ level is peaked at about 10^o, and is lower by at least a factor of 5 at all angles greater than 40^o. Unfortunately, the yield of ^3He particles scattered from the target is so large at angles less than 40^o that it is not practicable to use the approach and methods described in Section IV,B due to excessive count rates in the silicon detector. The 24" spectrometer magnet with a 140 micron thick silicon detector in the focal plane was therefore used to detect the α particles without interference from the elastically scattered ^3He.

The neutron detector used the same scintillator and photomultiplier as described in Section II,B. It was mounted in a cylindrical lead shield, 2 inches thick, with 1/2 inch of lead covering the front surface of the scintillator. The detector was mounted on a stand so that it pointed directly at the 90^o port of the magnetic spectrometer target chamber. The "blank off" cap on the port was 1/8" thick aluminum and the distance from the target

to the mid-point of the scintillator was measured to be 0.52 ± 0.005 meters. With this geometry, neutrons traveling in a straight line from the target to the detector passed only through the 1/8" thick aluminum cap and the 1/2" piece of lead immediately in front of the detector.

A block diagram of the electronic apparatus is shown in Figure 36. A timing signal was derived from the α detector by means of an ORTEC Model 260 time pickoff and fed to the START input of an ORTEC Model 437 time-to-amplitude converter (TAC). A fast signal from the anode of the XP1040 photomultiplier was inverted, clipped and fed to an ORTEC Model 417, fast, zero-crossing discriminator. The output of this discriminator went to the STOP input of the TAC.

A linear signal derived from the 11th dynode of the XP1040 photomultiplier was amplified and inspected by a discriminator. The discriminator threshold was set so that it accepted all pulses which exceeded 1/10 the size of the mid-point of the Compton edge for 662 keV gamma rays from a ^{137}Cs source rather than 1/8, as was used in the previous experiments; this increased the detection efficiency for 0.8 MeV neutrons, corresponding to the decays of ^{17}O(T = 3/2) to the 6.05 and 6.13 MeV levels of ^{16}O. The detection efficiency for 6.8 MeV neutrons, corresponding to decays to the ground state of ^{16}O, was found to be unaffected by the change in discriminator threshold. The efficiency for detection of 0.8 MeV neutrons, with the threshold set at 1/10, was determined in the "cannon mount", by comparison with the known value for 6.8 MeV neutrons, using the values for the 0° cross sections of the

$t(p,n)^3He$ reaction at the two energies, presented by Seagrave (1960).

The energy signal from the silicon detector was amplified and fed to a single-channel analyzer (SCA) which was centered on the alpha-particle peak in the charged particle spectrum. The output of this SCA was counted by a scalar which measured the total number of α-particles detected.

The outputs of the two SCA's were fed to an ORTEC Model 409 slow coincidence unit and its output was used to gate the RIDL multichannel analyzer, which was analyzing the spectrum from the TAC. In this manner, a time of flight spectrum was obtained for all detected neutrons which were in coincidence with α-particles counted in the magnetic spectrometer.

b. Experimental Details

The difference in path length between particles which transverse the magnet on paths with the maximum and minimum accepted radii of curvature is 0.6 meters. For a 12 MeV incident energy, the alpha particles corresponding to the 11.075 MeV level in ^{17}O have a reciprocal velocity of 40 nanoseconds (ns) per meter, so that the maximum spread in transit times through the magnet is 24 ns. It was therefore necessary to reduce the "Ø" entrance slits of the magnet, restricting the accepted paths through the magnet, to improve the time resolution.

A pulsed beam was used and a time spectrum was observed from the TAC, which was started by pulses from the alpha-counter time pickoff, and stopped by signals derived from the beam-pulsing

system in the usual manner. The full width at half maximum (FWHM) of the observed peak was found to decrease nearly linearly with the angular opening of the magnetic spectrometer and a FWHM of 3 ns was obtained for $\emptyset$ slit settings of $\pm$ 4.5($\Delta\emptyset = 2^{o}$). The time resolution was found to be insensitive to the angular aperture in the θ-direction and so the θ-slits were opened to their maximum values ($\pm 2^{o}$).

The magnet was set at 10^{o}, which was found to be the maximum yield point on the α-particle angular distribution. The neutron detector was then at 80^{o} from the beam axis, and on the opposite side from the magnet. With the entrance slit settings as described above, and a 2000 $\mathring{A}$ $Ni^{18}O_2$ target the $^{17}O(11.075)$ peak was three times as broad as that shown in Figure 34b. The only other observable level nearby was due to the $^{12}C(^{3}He,\alpha)^{11}C(0.0)$ reaction, from carbon contamination in the target, and this level is bound to neutron decay so that it will not contribute to the neutron spectrum.

For this reason poorer α-particle energy resolution was quite acceptable, and a 1/2"-slit was used in the focal plane in order to obtain larger counting rates.

A coincidence run of twelve hours duration was taken with the magnet set on the $^{17}O(T = 3/2)$ peak and a five-hour run was taken for the background on each side of the peak.

A flat background due to chance coincidence events was observable in all the spectra and could be determined from the average number of counts in the region of the spectrum corresponding

to flight times faster than gamma rays (3.3 ns/m). This average random-coincidence background was subtracted from all spectra. The two real-coincidence background spectra were added, and normalized to the same integrated charge as the spectrum taken on the $^{17}O(T = 3/2)$ peak. This summed and normalized background spectrum was then subtracted from the spectrum obtained on the peak, and the result is shown in Figure 37.

The time scale was determined by the use of the 150 ns calibrated cable described in Section II,D,4, but a problem arose in the determination of the zero point of the time scale.

Hensley and Nettles (1969) have studied the energy spectrum of gamma rays in coincidence with alpha particles populating the $^{17}O(T = 3/2)$ level, and they see very few events which can be attributed to gamma rays de-exciting this level. Therefore, the usual method of determination of the zero point of the time scale, from a peak produced by gamma rays from reactions in the target, is not useful here.

From the information already obtained in the $^{15}N(^{3}He,p)$ $^{17}O^{*}(n)^{16}O$ reaction, it was expected that the $^{17}O(11.075)$ level would decay predominantly to the $^{16}O(0.0)$ level, with a branching ratio greater than 48%. Only one peak in the spectrum corresponds to a branching ratio this large, and, if it is assumed to be the peak from $^{17}O(11.075) \rightarrow {}^{16}O(0.0) + n$, the resulting time-zero is consistent in the following ways:

1. The zero of time is near the position calculated from a knowledge of the lengths of cables from the detectors to the TAC,

the flight time for alpha-particles through the magnet and the approximately-known delay time in the photomultiplier.

2. A peak is observed at flight times slightly larger than those expected for prompt gamma rays from the target, but consistent with gamma rays produced by inelastic neutron scattering in the walls of the target chamber.
3. The major peak has a line shape consistent with that expected for neutrons of about 6 MeV energy, as will be discussed below.
4. The only other observed peak in the spectrum, which may be seen above the tail of the major peak, is found to occur near the expected flight time of neutrons from the decay of the T = 3/2 level to the 6.05 and 6.13 MeV levels of ^{16}O.

For these reasons, the above interpretation of the observed neutron spectrum appears to be unambiguous, and the two peaks marked by arrows in Figure 37 were used to determine the branching ratios for neutron decay of the $^{17}O(T = 3/2)$ state.

c. Line Shapes

The magnitude of the "tail" on the peak corresponding to decays of the $^{17}O(T = 3/2)$ level to the ground state of ^{16}O (ground state peak) makes it necessary to determine the true line shape for neutrons of this energy rather carefully, in order to determine the branching ratios.

As the "tail" is undoubtedly due to neutrons scattered into the detector by surrounding material, the line shape may be dependent

on the angular distribution of neutrons from the reaction used to study it. Since the $^{17}O(T = 3/2)$ decay angular distribution is isotropic (except for small center-of-mass corrections), a reaction was sought which produced neutrons of approximately the correct energy, did not produce other neutron groups with energies within 6 MeV of the primary group, and had an angular distribution which was as close as possible to isotropic. The $^{13}C(\alpha,n)^{16}O(0.0)$ reaction satisfies all of these requirements at an incident energy of 4.70 MeV, corresponding to a compound-nucleus resonance with an excitation energy of 9.95 MeV in ^{17}O. The angular distribution for this energy, has been studied by Morris (1967) and was found to be reasonably isotropic over the angular range from 20^{o} to 160^{o}. This angular region comprises about 65% of the total neutron cross section at this energy.

The solid curve in Figure 37 is the neutron line shape obtained from the $^{13}C(\alpha,n)^{16}O(0.0)$ reaction, normalized to fit the data at the peak. It appears to fit the data reasonably well over a wide range of flight times and it may thus be used to remove the contribution from the tail of the ^{16}O ground state peak in the region of the peak due to the ^{16}O 6.05 and 6.13 MeV levels. A similar determination of the line shape for the peak corresponding to decays to ^{16}O (6.05) and (6.13) was made using the $t(p,n)^{3}He$ reaction at 1.7 MeV incident energy, which also exhibits a nearly isotropic angular distribution; the observed shape is presented as the darker dashed curve in Figure 37.

The efficiency of the neutron detector has been well

determined by measurements made with the detector mounted inside the "cannon" mount described earlier. Peaks obtained with this geometry however, show small amounts of "tail" compared to that shown for the ground state peak in Figure 37.

Therefore, in order to determine the effective efficiency of the neutron detector in the geometry of the $^{16}O(^{3}He,\alpha)^{17}O^{*}(n)^{16}O$ coincidence runs, spectra were obtained from the $^{13}C(\alpha,n)$ and $t(p,n)$ reactions in this geometry and in the cannon mount. Figure 38 shows the spectra obtained for the $^{13}C(\alpha,n)$ reaction in the two geometries, and the arrows indicate the region which was summed in the two spectra to measure the relative detector efficiency.

d. Branching Ratios

From the measured data and efficiencies, the branching ratios were calculated from the following expression:

$$B.R.(\%) = \frac{N_n}{N_\alpha} \times \frac{4\pi}{\Omega_n \times \eta_{rel} \times \eta_{abs}}$$

where

N_n = number of counts in the region of the peak in the coincidence spectra which was used in the determination of the relative detector efficiency.

η_{rel} = ratio of neutron detector efficiency in the magnetic-spectrometer geometry to that obtained in the cannon mount.

η_{abs} = absolute detector efficiency measured in the cannon mount geometry.

Ω_n = neutron detector solid angle, in steradians.

N_α = total number of α-particles detected during the run with the magnetic-spectrometer set on the peak, minus the number obtained in the normalized background runs.

From this expression, the branching ratio for decay to the ground state of ^{16}O was determined to be 91 ± 15%. The major source of error was the uncertainty in the determination of the detector efficiency in the magnet geometry, estimated to be ± 15%; the absolute neutron-detector efficiency in the cannon mount geometry is known only to ± 10%, and there were additional uncertainties involved in the comparison with the magnet geometry arising from beam current integration and target uniformity.

For the determination of the branching ratio to the first two excited states of ^{16}O, there was an additional uncertainty caused by the lack of an accurate knowledge of the background underneath the peak. The $^{13}C(\alpha,n)$ line shape passed through the error bars on the data points, in the neutron energy region $1.2\ \text{MeV} < E_n < 4\ \text{MeV}$, but was generally lower than the actual data points. This line was therefore assumed to be a lower limit on the background level. An upper limit was estimated from a parallel line which passed through the majority of the error bars but fell generally above the data points in the region $1.2\ \text{MeV} < E_n < 4\ \text{MeV}$, as shown by the lighter dashed curve in Figure 37. This uncertainty is unavoidable since the ground-state calibration line-shape was obtained for neutrons 1 MeV lower in energy than those from the

$^{17}O(T = 3/2)$ state, and the angular distributions were not identical in the two cases.

The resulting branching ratio for decay of the $^{17}O(T = 3/2)$ state to the unresolved 6.05 and 6.13 MeV levels of ^{16}O was 5 ± 2%. The error was calculated as the square root of the sum of the squares of errors resulting from the counting statistics and the uncertainties in detector efficiency and background subtraction discussed above.

It is interesting to compare these results with those obtained from the $^{15}N(^{3}He,p)^{17}O^{*}(n)^{16}O$ reaction, which was described in Section IV,C,1. Now that further knowledge of the branching ratio of the 11.075 MeV (T = 3/2) level in ^{17}O to $^{16}O(6.05 + 6.13)$ has been obtained, it is possible to determine the branching ratio of the 11.023 MeV level to these levels, from the data illustrated in Figure 33. Taking possible errors into account, a lower limit of 25% is obtained for decay of the 11.023 level of ^{17}O to the 6.05 and 6.13 MeV levels of ^{16}O.

The remainder of the decay of the 11.023 MeV level may proceed by neutron decay to the ground state of ^{16}O, or by alpha particle decay to the ground state or first excited state of ^{13}C. The determination of the branching ratio of the 11.075 MeV ^{17}O level to the ground state of ^{16}O is thus uncertain due to the contribution of a possible 75% branching ratio from the less-strongly-populated 11.023 MeV level. The resultant limits on the branching ratio for the 11.075 MeV level to the ground state of ^{16}O are

$54 < BR(\%) < 100$, consistent with the more precise determination $91 \pm 15\%$, obtained in the study of the $^{18}O(^{3}He,\alpha)^{17}O^{*}(n)^{16}O$ reaction.

D. Conclusions

The results for the neutron and proton branching ratios of the lowest T = 3/2 levels in ^{17}O and ^{17}F are summarized in Table 8. These results for ^{17}F are in good agreement with recent measurements by Hardy et al. (1969b), who measured $12 \pm 4\%$ for the decay to the ground state of ^{16}O, $26 \pm 8\%$ for the decay to the 6.05 MeV level and set an upper limit of 10% for the decay to the 6.13 MeV level.

The branching ratios for ^{17}F and ^{17}O are considerably different, but the energies available for decay are also quite different as may be seen from Figure 27. To make a meaningful comparison, it is necessary to remove the effects due to differences in phase space and barrier penetration. These penetrabilities were calculated as $P_{\ell} = \rho/F_{\ell}^{2} + G_{\ell}^{2}$ where F_{ℓ} and G_{ℓ} are the regular and irregular Coulomb functions, respectively. The penetrabilities for the neutron case were obtained by assuming a very small charge (0.001e) for the neutron, which effectively removes the Coulomb effects. The ground state and 6.05 MeV state of ^{16}O have $J^{\pi} = 0^{+}$ and the 6.13 level is 3^{-} so penetrabilities were calculated with $\ell = 1$ and 2, respectively, for the transitions from the $1/2^{-}$, T = 3/2 levels. A radius of 4.4 fm was used in the calculations.

Reduced widths, θ^{2}, were calculated by dividing the branching ratios by the pentrabilities. For the decays to the two unresolved excited states, the θ^{2}'s were calculated by assuming that

the decay went entirely to one or the other of the states. The ratios of these reduced widths to that for the ground state decays, are tabulated in Table 8, and may be seen to be quite different for the two mirror T = 3/2 levels, independent of the assumption of ^{16}O final state.

The difference in the ratio of reduced widths observed here is, in fact, larger than that observed in the mass 13 case (see Table 6). It is interesting to note that in the mass 17 case the larger ratio is observed for the neutron rich member whereas the opposite is true for mass 13.

Arima and Yoshida (1969) have calculated decay widths for the mass 13 case and the results are listed in Table 6. They calculated transition matrix elements for a Hamiltonian containing a charge independent nuclear potential and a Coulomb potential. The wave functions for the T = 3/2 levels were obtained by calculating isospin impurities in first order perturbation approximation, using the charge independent wave functions of Cohen and Kurath (1965) as a basis. The final state wave function was determined in a similar fashion but included the scattering particle wave function distorted by an optical potential. As may be seen from the table, they did obtain correct orders of magnitude for the widths and found differences for the partial widths of the two mirror T = 3/2 levels, although detailed agreement is not good. As the calculation is based on the mixing of T = 1/2 levels whose positions have been predicted theoretically, it is likely that the results could be improved if experimental information becomes available on the excitation energies of these levels.

It is interesting that differences in the ratios of reduced widths can be produced solely by charge independent nuclear forces and the Coulomb interaction, but it remains to be seen whether the extent of the observed differences can be explained on this basis alone. It is hoped that a similar calculation will be performed for the mass 17 case.

A considerable amount of information can be obtained regarding the form of the isospin violating interaction causing these effects by considering the formula for the ratio of the reduced widths, in first order perturbation approximation.

The wave functions for the initial mass 17, (T = 3/2) and final (^{16}O + nucleon) states may be written as the sum of a dominant T = 3/2 part and a T = 1/2 isospin impurity, in the following manner:

$$|i\rangle = |a;\ T = 3/2,\ T_z\rangle + \sum_i \beta_i(T_z)\ |b_i;\ T = 1/2,\ T_z\rangle$$

$$|f\rangle = \left\{|c;\ T = 0,0\rangle + \sum_j \delta_j |d_j;\ T = 1,\ 0\rangle\right\}\ |T = 1/2,\ T_z\rangle$$

where the sums run over all the states of the same spin and parity which could be admixed. a, b_i, c, and d_j characterize all the other properties of the levels and the β_i (or δ_j) can be written explicitly as

$$\beta_i(T_z) = (E_a - E_b)^{-1} < b_i,\ T_z|H_{NC}|a,\ T_z >$$

where E_a, E_b are the energies of the states a, b_i and H_{NC} is the isospin-nonconserving Hamiltonian operator which is being treated

as the perturbation.

For the Coulomb interaction, or any two-body charge dependent interaction, H_{NC} may be written as a sum of spherical tensor operators of rank ≤ 2.

$$H_{NC} = T^0 + T^1 + T^2$$

Using the Wigner-Eckart theorem, we can write

$$< b_i,\ T = 1/2,\ T_z = \pm 1/2 |\ H_{NC}|\ a,\ T = 3/2,\ T_z = \pm 1/2 >$$

$$= (3/2\ 0\ T_z\ 0|\ 1/2\ T_z) < b_i \| T^0 \| a > + (3/2\ 1\ T_z\ 0|\ 1/2\ T_z) \times$$

$$< b_i \| T^1 \| a > + (3/2\ 2\ T_z\ 0|\ 1/2\ T_z) < b_i \| T^2 \| a >$$

$$= 0 - \sqrt{1/3} < b_i \| T^1 \| a > \mp \sqrt{2/5} < b_i \| T^2 \| a >$$

Therefore,

$$\beta_i\ (T_z = \pm 1/2) =$$

$$(E_a - E_b)^{-1} \left\{ - \sqrt{1/3} < b_i \| T^1 \| a > \mp \sqrt{2/5} < b_i \| T^2 \| a > \right\}$$

and there are two ways in which the T = 1/2 admixture in the T = 3/2 levels can be different for $T_z = \pm 1/2$:

1. The proximity of admixed T = 1/2 levels may be different so that $(E_a - E_b)^{-1}$ is different for $T_z = \pm 1/2$.
2. The reduced matrix elements of T^1 and T^2 may be of comparable size so that β_i is affected by the **sign** of the T^2 term.

We can write the ratio of reduced widths to the two final states $C(^{16}O(0.0))$ and $C'(^{16}O(6.05 \text{ or } 6.13))$ as

$$\theta_c^2/\theta_{c'}^2 = |\langle f|i\rangle / \langle f'|i\rangle|^2$$

For $T_z = \pm 1/2$

$$\langle f|i\rangle = \sum_i \beta_i (T_z) \langle c;\ T = 1/2|\ b_i;\ T = 1/2\rangle + (2/3)^{1/2} \sum_j \delta_j^* \langle d_j;\ T = 3/2|\ a;\ T = 3/2\rangle + \text{terms of order } \beta\delta, \text{ to be neglected.}$$

So,

$$\frac{\theta_c^2}{\theta_{c'}^2} = \left| \frac{\sum_i \beta_i(T_z) \langle c|b_i\rangle + (2/3)^{1/2} \sum_j \delta_j^* \langle d_j|a\rangle}{\sum_i \beta_i(T_z) \langle c'|b_i\rangle + (2/3)^{1/2} \sum_j \delta_j^{*\prime} \langle d_j'|a\rangle} \right|$$

From this expression it may be seen that isospin impurities must be significant in the T = 3/2 levels to produce a difference in the ratio of reduced widths. $\beta(T_z)$ is the only T_z dependent quantity, so the observed effect requires that it is not negligible.

The calculations by Arima and Yoshida (1969) indicated that the matrix elements of the isospin impurities in the initial and final states were of the same order of magnitude. In this case, the observed differences could be produced by the admixture of just one T = 1/2 level into the T = 3/2 levels and $\beta(T_z)$ may be dependent on the position of the T = 1/2 level relative to the T = 3/2 level in the two nuclei. In fact, in the mass 13 case, the shell model calculations by Cohen and Kurath (1965), which were used by Arima and Yoshida (1969), predict a T = 1/2, $J^{\pi} = 3/2^-$ state very near the

$T = 3/2$, $J^{\pi} = 3/2^-$ level. As a result, Arima and Yoshida (1969) observed a strong admixture of this level. In calculations for mass 17, (Margolis 1966) no $1/2^-$, $T = 1/2$ levels are predicted which are particularly close to the lowest $T = 3/2$ level.

In a recent paper considering the effects of second order perturbations due to the Coulomb interaction, Jänecke (1969) has calculated the magnitudes of the off-diagonal isovector and isotensor matrix elements necessary to explain the deviations of the masses of the members of the mass 9 multiplet from the values expected from first order perturbations. Assuming that the only level which is mixed into the $T = 3/2$ levels is a $T = 1/2$ level at lower excitation, he calculated an isovector matrix element about 35 times the size of the isotensor term. In the present formulation, this would suggest that $\beta(-1/2) \approx \beta(+1/2)$ and large differences would not be predicted for the ratios of branching ratios for particle decays of the $T_z = \pm 1/2$ members of the mass 9 multiplet.

Although experimental uncertainties are larger for higher mass multiplets, Jänecke discussed a trend observable in the second order perturbations which suggests that the perturbations result mostly from one or several states with $T = 1/2$ at lower excitation energies than the $T = 3/2$ levels. He suggests a possible explanation of such a trend based on the strong admixture of so-called "anti-analogue" states, with similar space structure and $T = 1/2$, which would be expected at lower excitation energies. As the Coulomb interaction has only a weak spatial dependence, the similar space structure of these levels could lead to large matrix elements connecting with the

T = 3/2 levels.

Two particle transfer reactions have been found to populate T = 3/2 levels strongly due to their simple structure and such reactions would also be expected to populate these anti-analogue levels. It is interesting to re-examine spectra from (^{3}He,n) reactions (see Adelberger et al. (1969), to look for such levels. In most of the nuclei examined a relatively strongly populated level which appears to have an angular distribution similar to the lowest T = 3/2 level occurs at lower excitation energy. In ^{9}B, a prominant T = 1/2 level is observed near 12 MeV, in ^{13}N at 3.51 MeV ($3/2^{+}$) and in ^{17}F at 3.10 MeV ($1/2^{+}$), although other levels are populated whose spins and parities have not been determined.

The feasibility of further, more precise, calculations of isospin mixing in T = 3/2 levels, appears to depend upon the determination of the positions and structure of T = 1/2 levels of the same spin and parity. Further experimental studies of such levels would be of considerable interest.

Until these more accurate calculations are performed it will not be possible to say whether the observed large differences in the ratios of reduced widths will require the introduction of a specifically nuclear charge-dependent force for their explanation.

REFERENCES

Adelberger,E.G. and C.A. Barnes 1966, Phys. Lett. 23, 474.

Adelberger,E.G. 1967, Ph.D. Thesis, California Institute of Technology (unpublished).

Adelberger,E.G. 1967a, Nuc. Inst. and Meth. 47, 327.

Adelberger,E.G., A.B. McDonald and C.A. Barnes 1969, Nuc. Phys.A124, 49.

Adelberger,E.G., C.L. Cocke, C.N. Davids and A.B. McDonald 1969a, Phys. Rev. Letters 22, 352.

Ajzenberg-Selove, F. and T. Lauritsen 1959, Nuc. Phys. 11, 1.

Arima, A. and S. Yoshida 1969, Proc. of the Second Conf. on Nuclear Isospin, Asilomar, California (to be published).

Barnes, C.A., E.G. Adelberger, D.C. Hensley and A.B. McDonald 1967, Proc. International Conf. on Nuclear Physics, Gatlinberg, Academic Press,New York, p. 261.

Bassel, R.H., D.H. Drisko and G.R. Satchler 1962, Oak Ridge National Laboratory Report ORNL-3240 (unpublished).

Bearse, R.C., G.C. Morrison, J.C. Legg and R.E. Segel 1969, Bull. Am. Phys. Soc. 14, 124.

Bhatt, K.H. 1962, Nuc. Phys. 39, 375.

Birnbaum, J. 1965, Ph.D. Thesis, Yale University (unpublished).

Bloch, R., T. Knellwolf and R.E. Pixley 1967, Helv. Phys. Acta 40, 348.

Bloch, R., R.E. Pixley and P. Truöl 1967a, Phys. Letters 25B, 215.

Braid, T.H., A.M. Freidman and R.W.Fink 1965, Bull. Am. Phys. Soc. 10, 120 and 658.

Brolley, J.E. and J.L. Fowler 1960, Fast Neutron Physics, ed. by J.B. Marion and J.L. Fowler, Interscience, New York, p. 73.

Brunnader, H., J.C. Hardy and J. Cerny 1969, Phys. Rev. 174, 1247.

Butler, G.W., J. Cerny, S.W. Cosper and R.L. McGrath 1968, Phys. Rev. 166, 1096.

Cerny, J., 1969, Bull. Am. Phys. Soc. 14, 85.

Cerny, J. 1969a, Ann. Rev. Nuclear Sci. 18, 27.

Cohen, S. and D. Kurath 1965, Nuc. Phys. 73, 1.

Demirlioglu, D. and W. Whaling 1962, California Institute of Technology (unpublished).

Detraz, C. and H. H. Duhm 1969, Phys. Letters 29B, 29.

Dietrich, F. S. 1964, Ph.D. Thesis, California Institute of Technology (unpublished).

Dietrich, F. S. 1965, Nuc. Phys. 69, 49.

Dietrich, F. S., M. Suffert, A. V. Nero and S. S. Hanna 1968, Phys. Rev. 168, 1169.

Endt, P. M. and C. Van der Leun 1967, Nuc. Phys. A105, 1.

Esterlund, R.A., R. McPherson, A. M. Poskanzer and P. L. Reeder 1967, Phys. Rev. 156, 1094.

Feshbach, H. 1960, Nuclear Spectroscopy Part B, ed. by F. Ajzenberg-Selove, Academic Press, New York, p. 625.

Glover, R. N. and A. D. W. Jones 1966, Nuc. Phys. 81, 268 and 277.

Goldberg, M. D., J. D. Anderson, J. P. Stoering and C. Wong 1961, Phys. Rev. 122, 1510.

Goosman, D. R. 1967, Ph. D. Thesis, California Institute of Technology (unpublished).

Groce, D. E. 1963, Ph.D. Thesis, California Institute of Technology (unpublished).

Hardie, G., R.L. Dangle and L. D. Oppliger 1963, Phys. Rev. 129, 353.

Hardy, J. C. and R. E. Bell 1965, Can. J. Phys. 43, 1671.

Hardy, J. C., H. Brunnader, J. Cerny and J. Jänecke 1969a, University of California report UCRL-18566 and to be published.

Hardy, J. C., J. E. Esterl, R.G. Sextro and J. Cerny 1969b, Proc. of the Second Conf. on Nuclear Isospin, Asilomar, Calif., (to be published).

Hardy, J. C. 1969c, private communication.

Hart, V. P., E. Norbeck and R. R. Carlson 1965, Phys. Rev. 137, B17.

Hecht, K. T. 1967, Nuc. Phys. A102, 11.

Hecht, K. T. 1968, Nuc. Phys. A114, 280.

Henley, E. M. 1966, Isobaric Spin in Nuclear Physics, ed. by John D. Fox and Donald Robson, Academic Press, New York, p. 3.

Hensley, D. C. 1968, Phys. Lett. 27B, 644.

Hensley, D. C. 1969a, Ph.D. Thesis, California Institute of Technology (unpublished).

Hensley, D. C. 1969b, private communication.

Hensley, D. C. and P. H. Nettles 1969, private communication.

Hinds, S., H. Marchant and R. Middleton 1962, Nuc. Phys. 31, 118.

Horvat, P. 1964, Nuc. Phys. 52, 410.

Jänecke, J.1968, Nuc. Phys. A114, 433.

Jänecke, J. 1969, Proc. of the Second Conf. on Nuclear Isospin, Asilomar, Calif. (to be published).

Jänecke, J. 1969a, Nuc. Phys. A128, 632.

Kienle, P. and K. Wien 1963, Nuc. Phys. 41, 608.

Kuan, H. M., D. W. Heikkinen, K. A. Snover, F. Reiss and S. S. Hanna 1967, Phys. Letters 25B, 217.

Lane, A. M. and R. G. Thomas 1958, Revs. Modern Phys. 30, 257.

Lauritsen, T. and F. Ajzenberg-Selove 1966, Nuc. Phys. 78, 1.

Levine, M. J., and P.D. Parker 1967, Proc. Int. Conf. on Nuclear Structure, Tokyo, Japan, ed. by J. Sanada, Physical Society of Japan, p. 703.

Levine, M. J. 1968, Ph. D. Thesis, Yale University (unpublished).

Margolis, B. and N. DeTakasy 1966, Can. J. Phys. 44, 1431.

Matous, G. M., G. H. Herling and E. A. Woliki 1966, Phys. Rev. 152, 908.

Mattauch, J. H. E., W. Thiele and A. H. Wapstra 1965, Nuc. Phys. 67,1.

McDonald, A. B. and E. G. Adelberger 1968, Phys. Letters 26B,380.

McPherson, R. and J. C. Hardy 1965, Can. J. Phys. 43, 1.

Miller, R. G. and R. W. Kavanagh 1966, Bull. Am. Phys. Soc. 11,315.

Morris, J. M. 1967, Ph.D. Thesis, Australian National University, Canberra (unpublished).

Nettles, P. H., D. C. Hensley and T. A. Tombrello 1969, Proc. Second Conf. on Nuclear Isospin, Asilomar, Calif., (to be published).

Patterson, J. R., H. Winkler and C. S. Zaidins 1967, Phys. Rev. 163, 1051.

Paul, E. B. 1957, Phil. Mag. 2, 311.

Pearson, J. D. 1963, Ph.D. Thesis, California Institute of Technology (unpublished).

Reiss, F., W. J. O'Connell, D. W. Heikkinen, H. M. Kuan, S. S. Hanna 1967, Phys. Rev. Letters 19, 367.

Seagrave, J. D. 1960, Nuclear Forces and the Few Nucleon Problem, ed. by T. C. Griffith and E. A. Power, Pergammon Press, New York, p. 583.

Silbert, M. G. and J. C. Hopkins 1964, Phys. Rev. 134, B16.

Snover, K. A., E. G. Adelberger and F. Reiss 1968, Bull. Am. Phys. Soc. 13, 1662.

Temmer, G. M. and R. Van Bree 1966,Proc. of the Int. Conf. on Nuclear Physics, Gatlinberg, Academic Press, New York, p. 880.

Temmer, G. M. B. Teitelman, R. Van Bree and H. Ogata 1967, Proc. of the Int. Conf. on Nuclear Structure, Tokyo, Japan, ed. by J. Sanada, Physical Society of Japan, p. 299.

Weinberg, S. and S. B. Treiman 1959, Phys. Rev. 116,465.

Wigner, E. P., 1958,Proc. of the R.A. Welch Found. Conf. on Chem. Res. I. The Structure of The Nucleus, Houston, Texas, p. 67.

Wilkinson, D. H. 1964, Phys. Rev. Letters 13, 571.

Wilkinson, D. H. 1966, Isobaric Spin in Nuclear Physics, ed. by J. D. Fox and D. Robson, Academic Press, New York, p. 30.

TABLE 1

Saxon - Woods Parameters used in DWBA Calculations

(see page 17).

$$V(r) = \frac{-U}{1 + e^{x_u}} - \frac{iW}{1 + e^{x_w}}$$

$$\chi u = \frac{r - r_u A^{1/3}}{a_u} \qquad x_W = \frac{r - r_w A^{1/3}}{a_w}$$

	U (MeV)	W (MeV)	r_u (fm)	r_w (fm)	a_u (fm)	a_w (fm)
$^{19}F + {}^{3}He$	201.55	25.90	1.05	1.81	0.829	0.592
$^{21}Na + n$	54.4	20.0	1.2	1.2	0.51	0.30

TABLE 2

$T = 1/2$ Levels in ^{21}Na Observed in the Excitation Energy Range from 8.87 to 9.42 MeV. (See page 31)

E_p(MeV) (lab) (± 0.010)	E_x(MeV) (± 0.011)	Γ_{total}(keV)
6.825	8.928	24 ± 7
6.913	9.012	34 ± 9
6.972	9.068	30 ± 8
7.077	9.168	13 ± 4
7.024	9.289	29 ± 7
7.284	9.365	30 ± 7

TABLE 3

A. Values of Real, ℓ-dependent Background Phase Shifts Used to Calculate Solid Lines in Figure 22. (See Page 34.)

E_p^{lab}	δ_0	δ_1	δ_2	δ_3
6.872	-28^o	-2^o	0^o	6^o
7.128	-116^o	-10^o	-16.5^o	-4^o

B. Values of Complex, J-dependent Background Phase Shifts Used to Calculate Dashed Line in Figure 22. (See Page 37.)

E_p^{lab}	δ_0	δ_1^-	δ_1^+	δ_2^-	δ_2^+
7.128	57.3^o	165.3^o	$39.2^o+i58.0^o$	$-15.2^o+i14.3^o$	$-18.2^o+i16.3^o$

TABLE 4

Penetrabilities for the Decay of ^{21}Na (9.217)[a]

(see Page 38.)

Final State	ℓ	P_ℓ[b]
$p + {}^{20}Ne$ (0.0) (0^+)	0	2.07
(1.63)(2^+)	2	0.625
(4.25)(4^+)	4	0.00043
(4.97)(2^-)	1	0.147
(5.63)(3^-)	3	0.00011
(5.80)(1^-)	1	0.013
$\alpha + {}^{17}F$ (0.0) $(5/2^+)$	2	0.074
(0.50)$(1/2^+)$	0	0.053

a - Calculated for $R = 1.3(A_1^{1/3} + A_2^{1/3})$

b - $P_\ell = \rho/F_\ell^2 + G_\ell^2$

TABLE 5

Mass Excess (keV) of T = 3/2 Quartets in Mass 21[a]

^{21}F	^{21}Ne	^{21}Na	^{21}Mg	^{21}Mg (predicted)[b]
-46 ± 7	3126 ± 6	6788 ± 7	10950±120	10940 ± 29
233 ± 9	3409 ± 6	7033 ± 7	-	11105 ± 29

a - For references, see Page 40.

b - $3[M(^{21}Na) - M(^{21}Ne)] + M(^{21}F)$.

TABLE 6

Decay Properties of the Lowest T = 3/2 States in Mass 13

(see Pages 44, 70)

	$^{13}N(15.07) \rightarrow {}^{12}C + p$	$^{13}C(15.11) \rightarrow {}^{12}C + n$
$BR(^{12}C(0.0))$	0.202 ± 0.020	0.065 ± 0.014
$BR(^{12}C(4.43))$	0.121 ± 0.015	0.250 ± 0.036
$\theta^2(0.0)/\theta^2(4.43)$	1.18 ± 0.11	0.17 ± 0.03
Γ (keV)	1.17 ± 0.21	6.2 ± 1.1
Γ_{p_o} or Γ_{n_o} (keV)(EXPER)	0.24 ± 0.05	0.40 ± 0.11
Γ_{p_o} or Γ_{n_o} (keV)(THEOR)[a]	0.21	0.13
Γ_{p_1} or Γ_{n_1} (keV)(EXPER)	0.14 ± 0.03	1.55 ± 0.35
Γ_{p_1} or Γ_{n_1} (keV)(THEOR)[a]	0.46	0.39

a. Arima and Yoshida (1969).

TABLE 7

Branching Ratios for the Proton Decay of the Lowest T = 3/2 Level in ^{17}F From the $^{15}N(^{3}He,n)^{17}F^{*}(p)^{16}O$ Reaction (See Page 54.)

A. $^{17}F(11.195) \rightarrow {}^{16}O(0.0) + p$

$E_{^3He}$	θ_p	BR(%)
8.44	135^{o}	10.2 ± 2.8
8.25	90^{o}	11.3 ± 5.0
8.25	110^{o}	8.0 ± 3.2
8.25	120^{o}	7.0 ± 3.0
	Weighted Ave:	8.8 ± 1.6

B. $^{17}F(11.195) \rightarrow {}^{16}O(6.05 + 6.13) + p$

$E_{^3He}$	θ_n	BR(%)
8.93	145^{o}	25.0 ± 6.8
9.03	145^{o}	20.3 ± 5.3
	Weighted Ave:	22.1 ± 4.2

TABLE 8

Decay Properties of Lowest T = 3/2 Levels in Mass 17

(See Page 69)

	$^{17}F(11.195)$	$^{17}O(11.075)$
	$^{15}N(^{3}He,n)^{17}F\ (p)^{16}O$	$^{15}N(^{3}He,p)^{17}O(n)^{16}O$
BR($^{16}O(0.0)$)	0.088 ±0.016	0.91 ±0.15
BR($^{16}O(6.05 + 6.13)$)	0.22 ± 0.04	0.05 ±0.02
$\theta^2(0.0)/\theta^2(6.05)$	0.16 ±0.05	3.4 ± 1.4
$\theta^2(0.0)/\theta^2(6.13)$	0.066 ± .019	0.32 ±0.14

FIGURE 1

Schematic diagram of the beam pulsing system for the Model FN tandem accelerator, discussed on Page 7. The JN is a Van de Graaf accelerator used to produce 0.5 MeV beams of $^{3}He^{++}$ or $^{4}He^{++}$ ions, which are velocity modulated in Buncher No. 1, neutralized in the adder canal, and then drift to the center terminal of the tandem accelerator where they are again converted to positive ions and accelerated. Buncher No. 2 is used for velocity modulation of negative ion beams. The items enclosed within the dashed line are located in the control room.

BEAM PULSING SYSTEM FOR CIT/ONR TANDEM

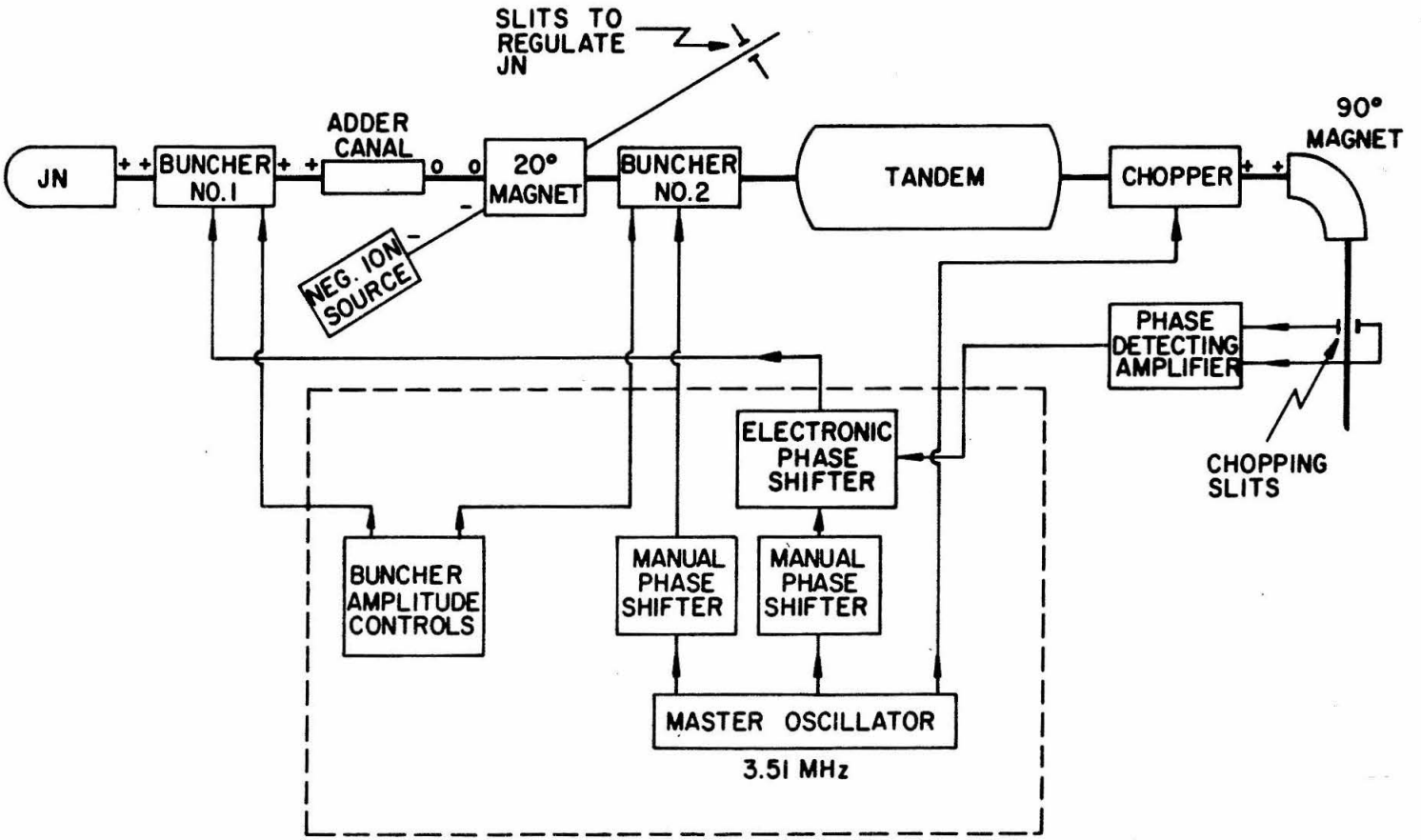

FIGURE 2

Block diagram of the electronic apparatus used to measure neutron flight times (see Page 10). The commercially available instruments symbolized by the blocks are:

1. Time-to-pulse height converter — Ortec Model 437.
2. Amplifier — discriminator — Ortec Models 410 and 420.
3. Fast amp No. 1 — Hewlett-Packard Model 460 BR.
4. Fast amp No. 2 — Nanosecond Systems Model 281.
5. Fast discriminator — Nanosecond Systems Model 205 FG.
6. Multichannel Analyzer — RIDL 400 Channel.

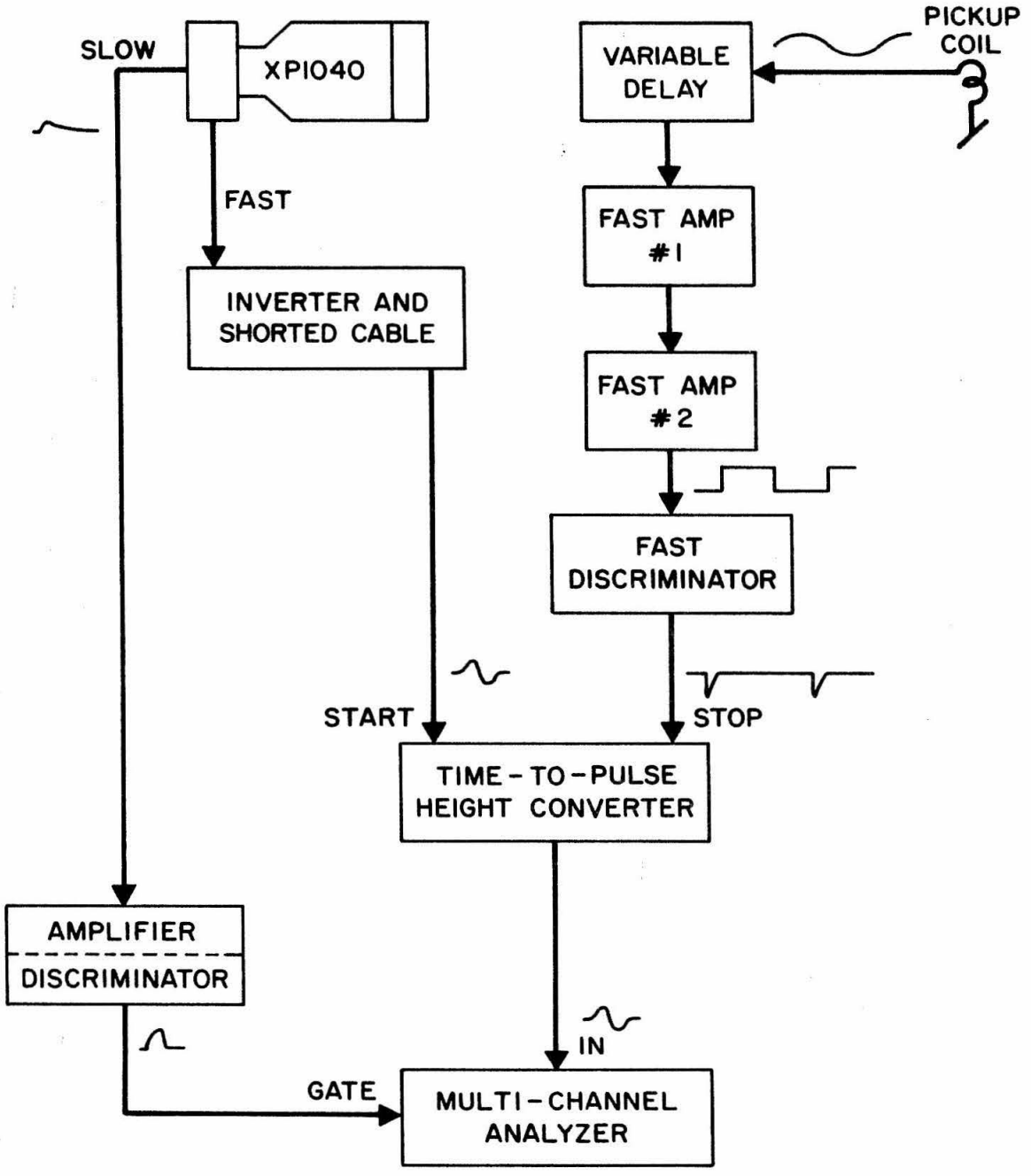
SLOW
XP1040
FAST
INVERTER AND SHORTED CABLE
VARIABLE DELAY
PICKUP COIL
FAST AMP #1
FAST AMP #2
FAST DISCRIMINATOR
START
STOP
TIME-TO-PULSE HEIGHT CONVERTER
AMPLIFIER
DISCRIMINATOR
IN
GATE
MULTI-CHANNEL ANALYZER

FIGURE 3

Detection efficiency of the neutron detector, determined from the d(d,n) and t(p,n) reactions, discussed on Page 12. In addition to the errors indicated, there is an overall error of ± 10% in the absolute efficiency. The solid curve is computed from an expression quoted by Dietrich (1964), neglecting multiple scattering, scattering from carbon, and scattering and absorption in the shield and collimator. The reduction in efficiency at low neutron energy is due to the slow-channel discriminator, which is assumed in the calculation to be set at a threshold of 450 keV proton energy. The dashed lines are approximations to the data, used for interpolation. In all results presented, the detection efficiency has been taken from the dashed lines, with an assumed relative error of ± 5%.

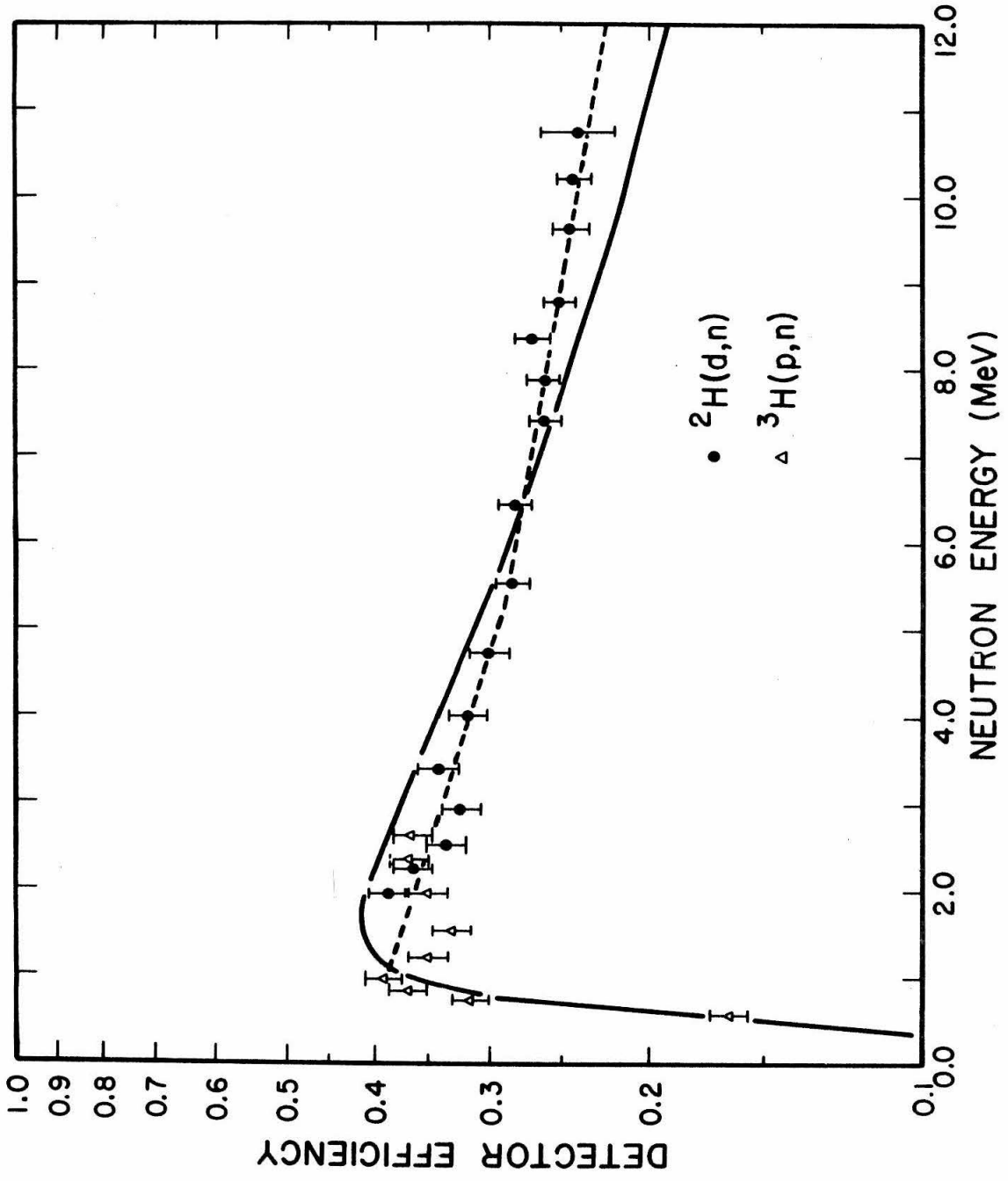
DETECTOR EFFICIENCY
NEUTRON ENERGY (MeV)
• $^{2}H(d,n)$
△ $^{3}H(p,n)$
1.0
0.9
0.8
0.7
0.6
0.5
0.4
0.3
0.2
0.1
0.0
2.0
4.0
6.0
8.0
10.0
12.0

FIGURE 4

Experimental line shape observed for 6.8 MeV neutrons produced by the $^{13}C(\alpha,n)^{16}O(0.0)$ reaction at 4.7 MeV incident energy. The neutron detector was at 0^{o}, at a distance of 1.1 meters from the target. For the discussion on Page 13, the triangle indicated by the solid lines was used to approximate the "main peak" and the remaining counts were assumed to make up the "tail" due to the collimator and shielding.

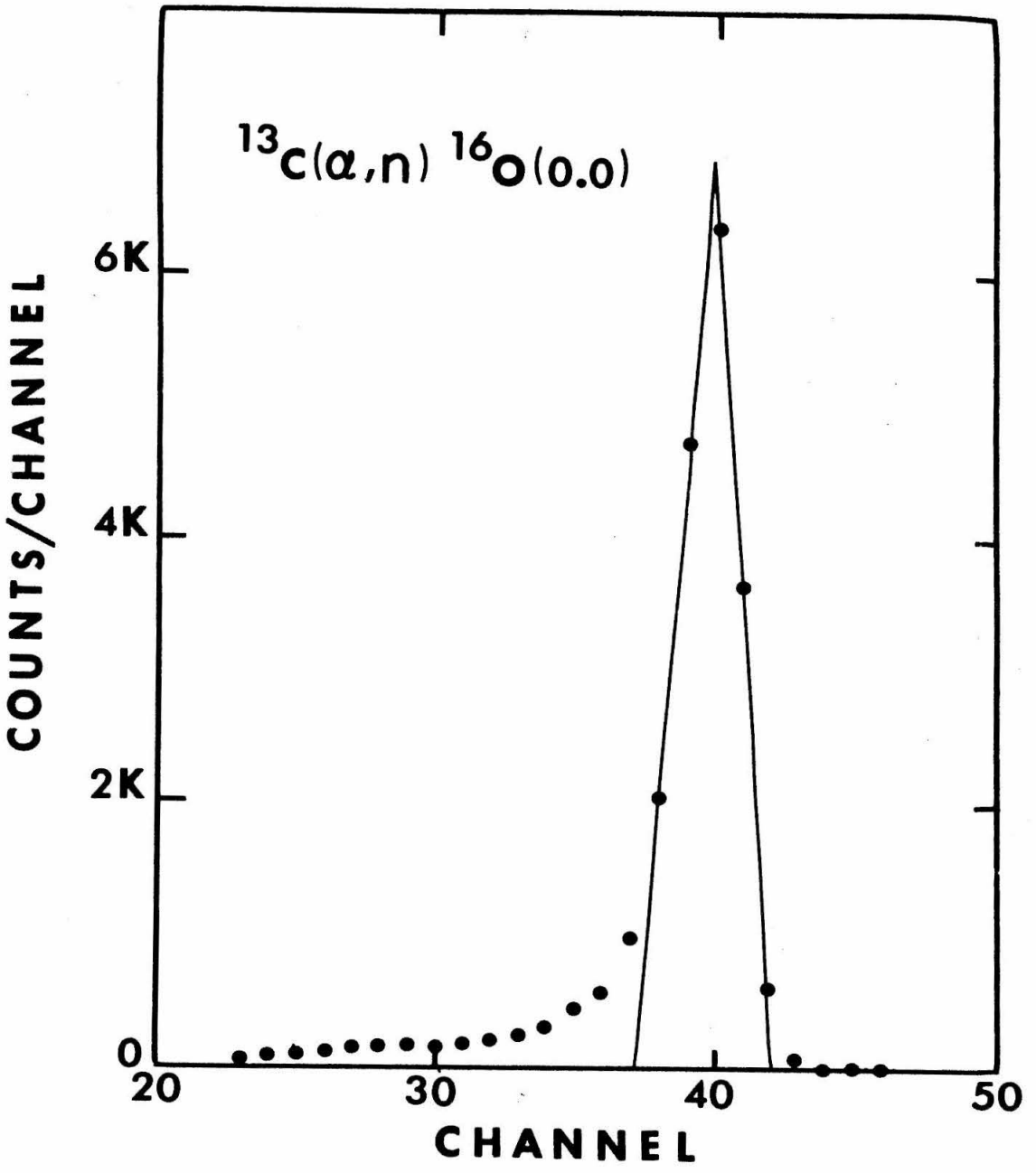
$^{13}C(\alpha,n)\ ^{16}O(0.0)$
COUNTS/CHANNEL
6K
4K
2K
0
20
30
40
50
CHANNEL

FIGURE 5

A comparison of the energies of 5.6 MeV ^{3}He particles, elastically scattered at 90^{o} from a clean piece of tantalum and from the tantalum backing of a CaF_2 target, used to determine the energy loss of ^{3}He particles in the CaF_2 layer. (See Page 15.)

a. A plot of the number of ^{3}He particles detected in the 24" radius magnetic spectrometer as a function of NMR frequency, for scattering from a clean piece of tantalum inclined at 45^{o} to the beam.

b. A similar plot for ^{3}He particles which have to traverse the CaF_2 coating on a tantalum backing.

The energy loss in the CaF_2 layer is determined from the difference in the energies of the midpoints (indicated by arrows) of the edges.

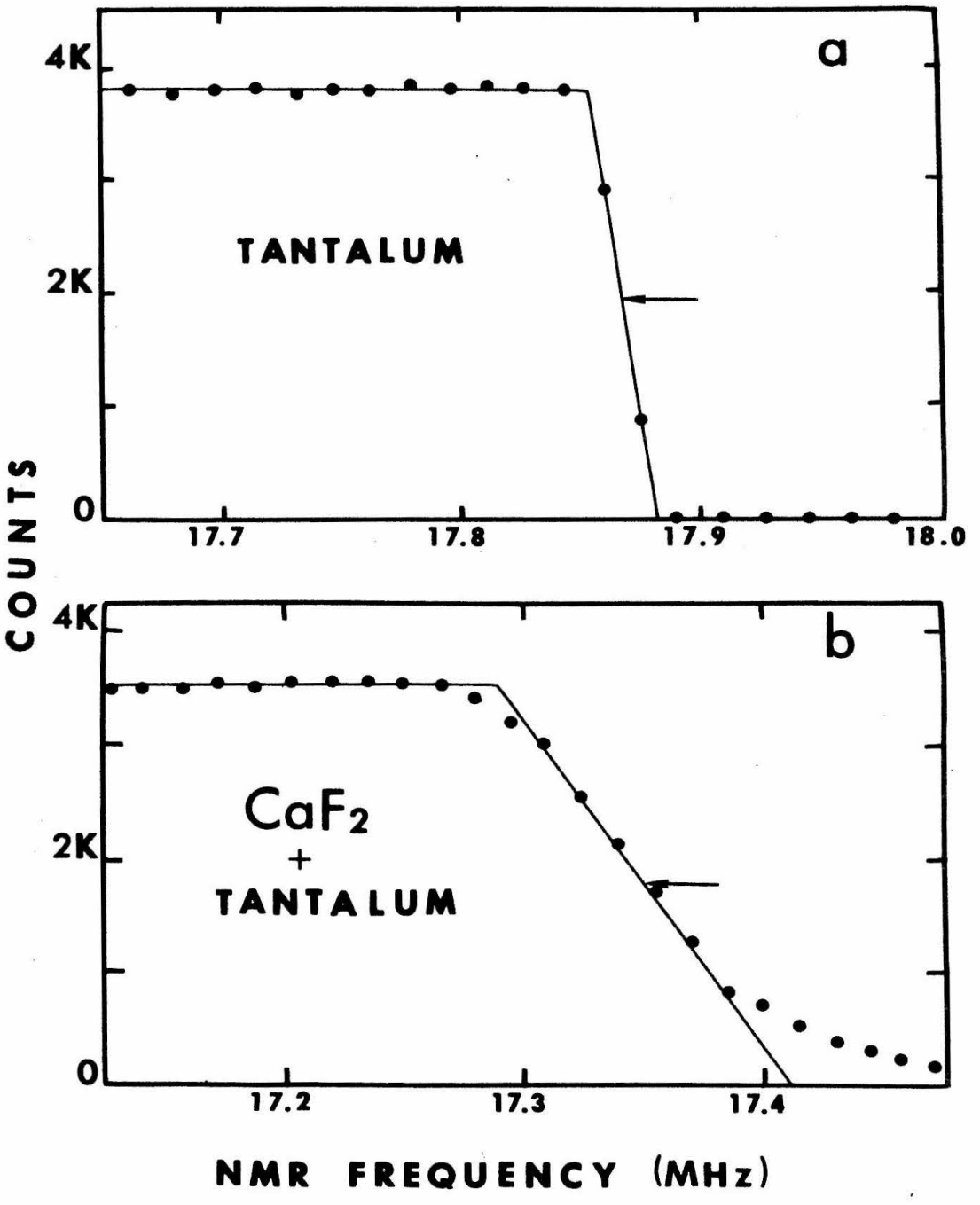
a
4K
2K
0
TANTALUM
17.7
17.8
17.9
18.0
b
4K
2K
0
CaF2
+
TANTALUM
17.2
17.3
17.4
COUNTS
NMR FREQUENCY (MHz)

FIGURE 6

Neutron time-of-flight spectrum from the $^{19}F(^{3}He,n)^{21}Na$ reaction at 5.855 MeV incident energy for $\theta_{LAB} = 0^{o}$. The intense peak near channel 190 is caused by prompt gamma rays. Neutron flight time increases from right to left and the time scale is approximately one nanosecond per channel. The peak labeled $^{14}O(0.0)$ is produced by the $^{12}C(^{3}He,n)$ reaction on carbon contamination in the target. For further discussion see Page 15.

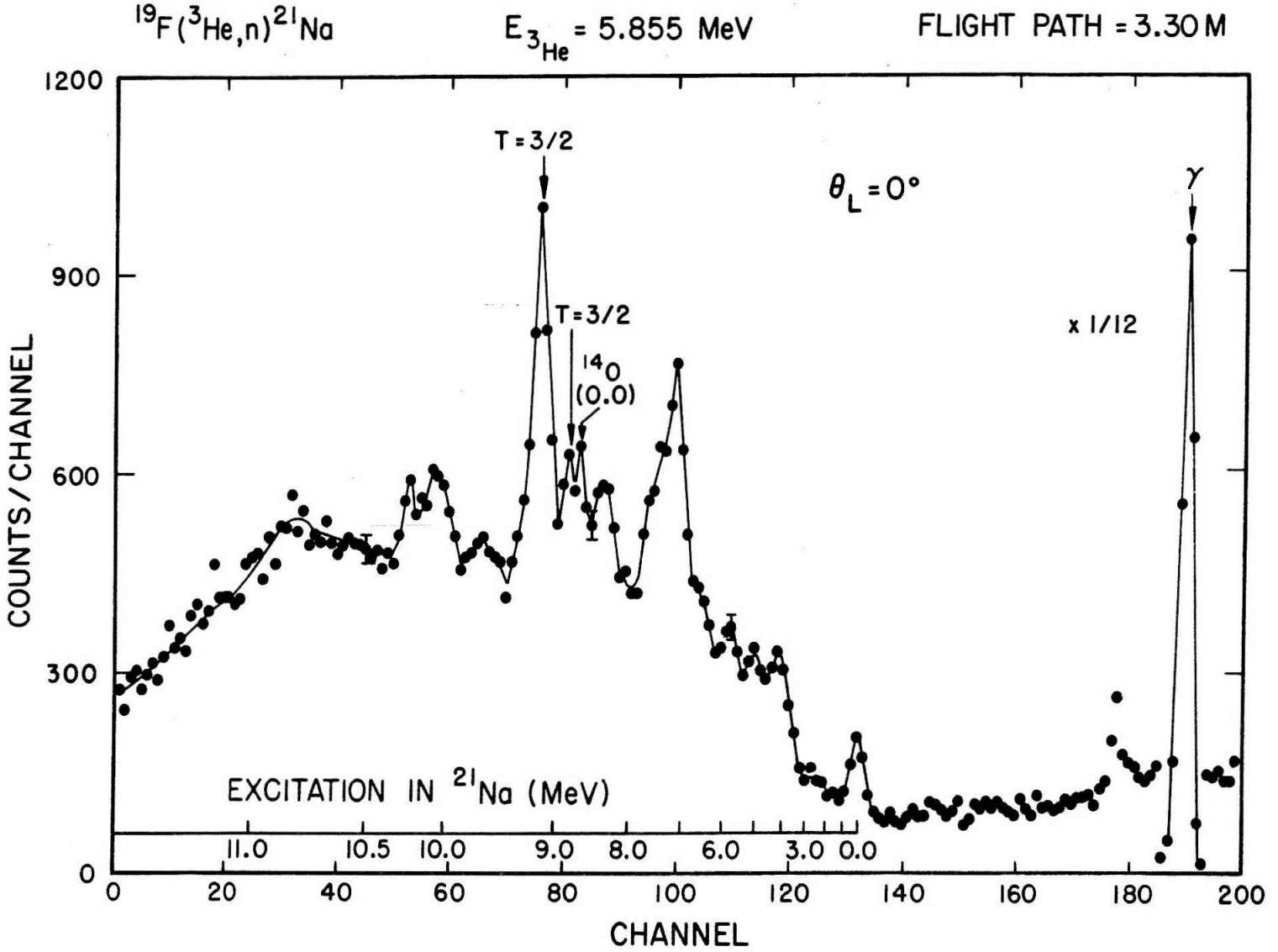
$^{19}F(^{3}He,n)^{21}Na$
$E_{^{3}He}$ = 5.855 MeV
FLIGHT PATH = 3.30 M
$\theta_L = 0°$
T = 3/2
T = 3/2
^{14}O (0.0)
γ
x 1/12
COUNTS / CHANNEL
CHANNEL
EXCITATION IN ^{21}Na (MeV)
11.0
10.5
10.0
9.0
8.0
6.0
3.0
0.0
0
300
600
900
1200
0
20
40
60
80
100
120
140
160
180
200

FIGURE 7

Angular distribution of neutrons from the $^{19}F(^{3}He,n)^{21}Na$ (9.221) reaction at 5.86 MeV incident energy. Error bars indicate statistical errors and uncertainties in background subtraction. There is an additional uncertainty of ± 20% in the absolute cross section due to uncertainties in target thickness, detector efficiency and charge integration.

The smooth curves are DWBA calculations using the optical model potentials listed in Table 1, with only the normalization treated as a free parameter. For further discussion, see Page 16.

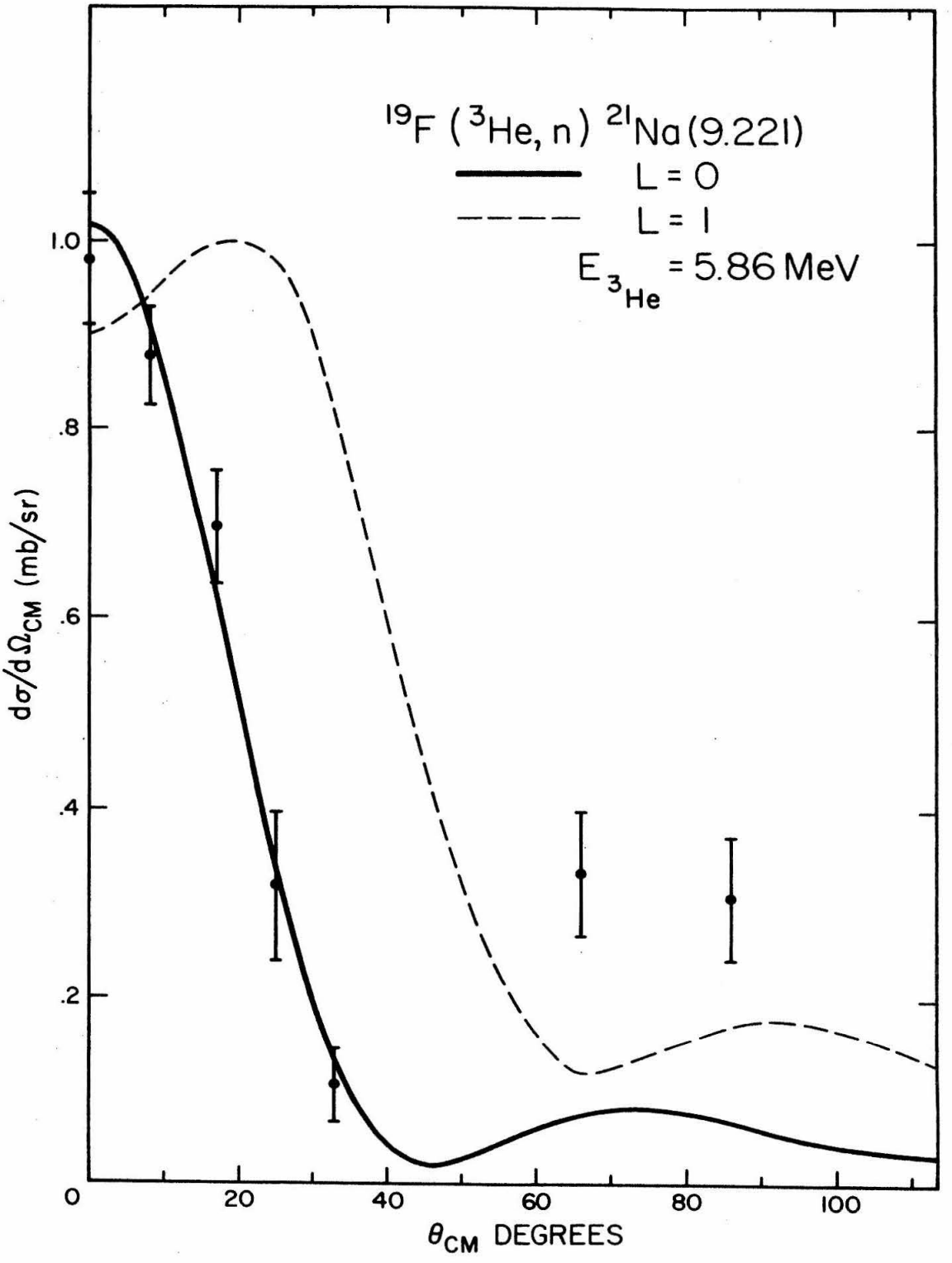
$^{19}F\ (^{3}He, n)\ ^{21}Na(9.221)$
L = 0
L = 1
$E_{^{3}He}$ = 5.86 MeV
1.0
.8
.6
.4
.2
0
20
40
60
80
100
$d\sigma/d\Omega_{CM}$ (mb/sr)
θ_{CM} DEGREES

FIGURE 8

Neutron time spectrum from the $^{19}F(^{3}He,n)^{21}Na$ reaction at 5.855 MeV incident energy, for $\theta_{LAB} = 60^{o}$. The peaks labeled T = 3/2 correspond to excitation energies of 8.99 and 9.22 MeV in ^{21}Na. The peak corresponding to the 8.99 MeV level contains less than 20% contribution from the $^{12}C(^{3}He,n)^{14}O(0.0)$ reaction. For further discussion, see Page 17.

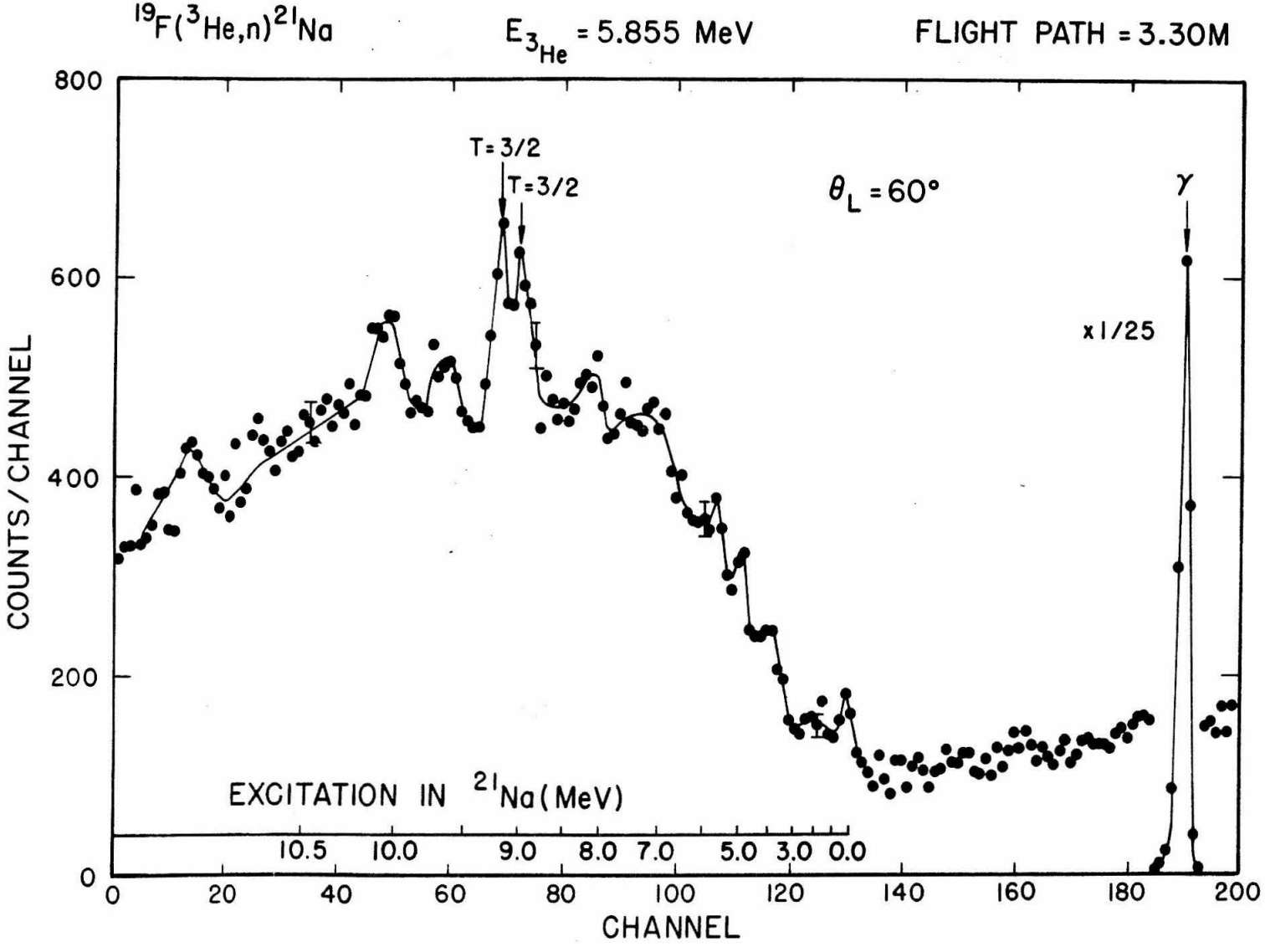
$^{19}F(^{3}He,n)^{21}Na$
$E_{^{3}He}$ = 5.855 MeV
FLIGHT PATH = 3.30M
T=3/2
T=3/2
θ_L = 60°
γ
x1/25
COUNTS/CHANNEL
CHANNEL
EXCITATION IN ^{21}Na(MeV)
10.5 10.0 9.0 8.0 7.0 5.0 3.0 0.0
0 200 400 600 800
0 20 40 60 80 100 120 140 160 180 200

FIGURE 9

Demonstration that the peak ascribed to a 9.221 MeV level in ^{21}Na was in fact produced by the $^{19}F(^{3}He,n)$ reaction. Q-values were computed from the series of runs making up the angular distribution of Figure 7, assuming various target masses. The χ^2 value for a fit to a constant Q-value is plotted as a function of assumed target mass. For further discussion, see Page 23.

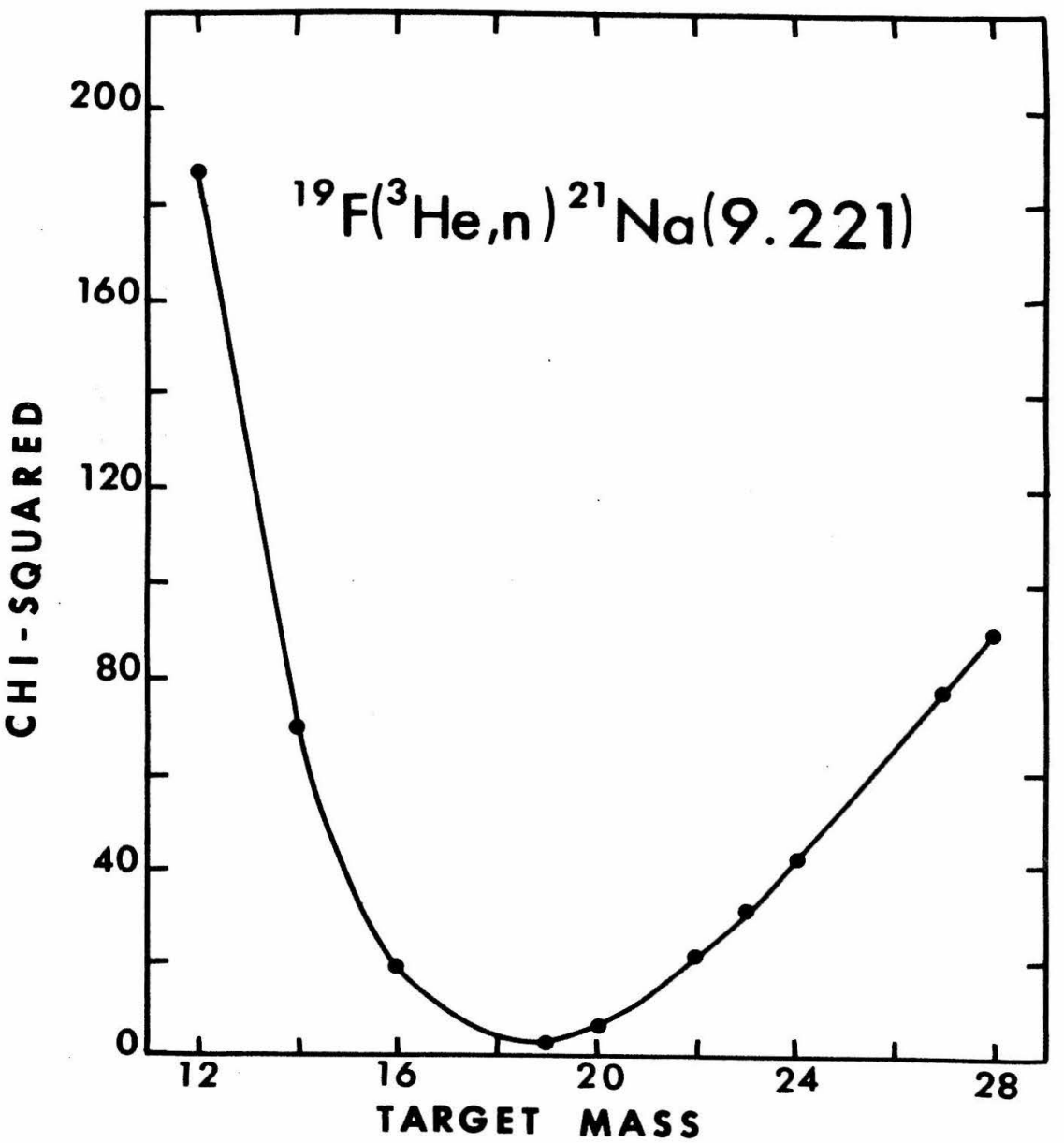
$^{19}F(^{3}He,n)^{21}Na(9.221)$
CHI-SQUARED
200
160
120
80
40
0
12
16
20
24
28
TARGET MASS

FIGURE 10

A = 21 isobar diagram. Information for ^{21}F levels comes from Horvat (1964); for ^{21}Ne from Hensley (1969a) and Ajzenberg-Selove and Lauritsen (1959); for ^{21}Na from the present work and Endt and Van der Leun (1967); for ^{21}Mg from Cerny (1969). To facilitate comparison of multiplets, energy scales have been shifted relative to ^{21}Na, to take into account the neutron-hydrogen mass difference and the Coulomb energy, the latter calculated from $E_c = 0.60\ Z(Z-1)/A^{1/3}$(MeV), as suggested by Lauritsen and Ajzenberg-Selove (1966). Since the lowest T = 1 level in ^{20}Ne occurs at an excitation energy of 10.27 MeV, and the lowest T = 3/2 level in ^{17}F occurs at an excitation energy of 11.20 MeV, the lowest two T = 3/2 levels in ^{21}Na are bound with respect to isospin conserving particle decays.

(See Page 25.)

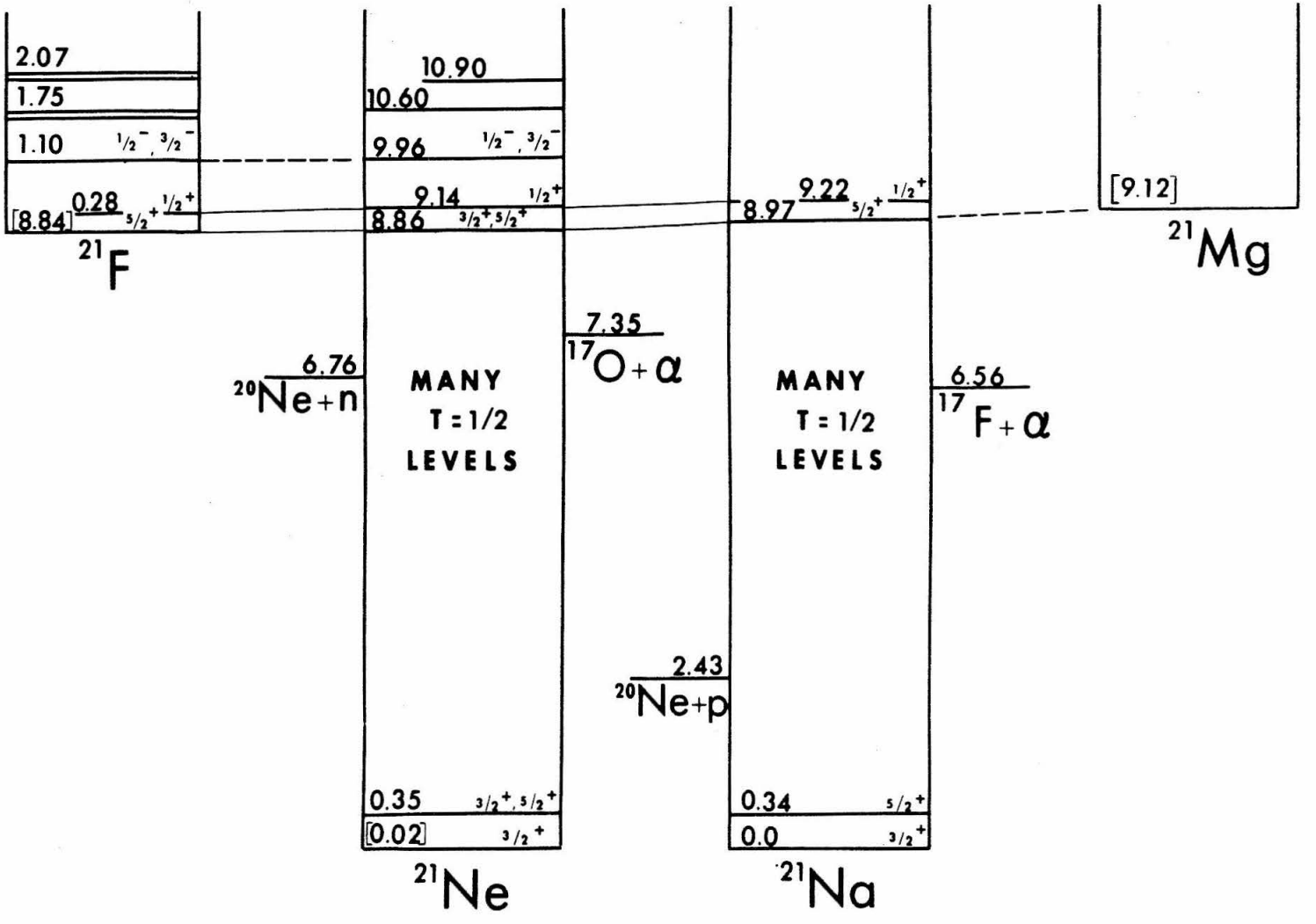
2.07
1.75
1.10 1/2⁻, 3/2⁻
[8.84] 0.28 5/2⁺ 1/2⁺
21F
10.90
10.60
9.96 1/2⁻, 3/2⁻
9.14 1/2⁺
8.86 3/2⁺, 5/2⁺
6.76
20Ne+n
MANY T = 1/2 LEVELS
7.35
17O+α
0.35 3/2⁺, 5/2⁺
[0.02] 3/2⁺
21Ne
9.22 5/2⁺ 1/2⁺
8.97
MANY T = 1/2 LEVELS
6.56
17F+α
2.43
20Ne+p
0.34 5/2⁺
0.0 3/2⁺
21Na
[9.12]
21Mg

FIGURE 11

Differentially-pumped gas target system, which was mounted inside a 60 cm. diameter scattering chamber. Cross hatched sections are aluminum; the entrance canals are brass. Note the lucite base used to insulate the target for application of the compensation voltage. The beam was collected in a Farraday cup about 20 cm. from the Havar exit foil. For further description, see Page 27.

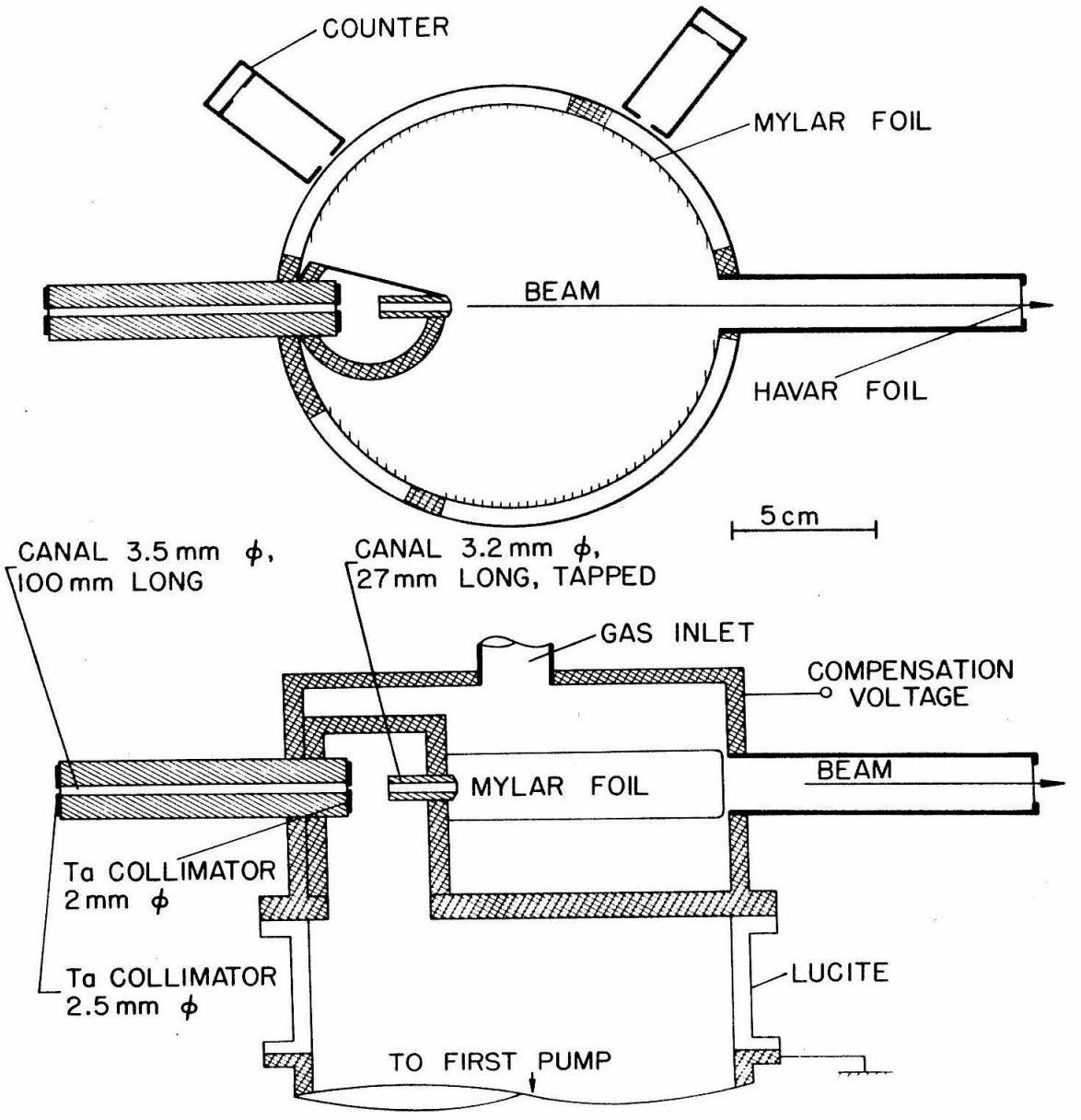
COUNTER
MYLAR FOIL
BEAM
HAVAR FOIL
5 cm
CANAL 3.5 mm ϕ,
100 mm LONG
CANAL 3.2 mm ϕ,
27 mm LONG, TAPPED
GAS INLET
COMPENSATION
VOLTAGE
MYLAR FOIL
BEAM
Ta COLLIMATOR
2 mm ϕ
Ta COLLIMATOR
2.5 mm ϕ
LUCITE
TO FIRST PUMP

FIGURE 12

Energy spectrum of elastically scattered particles from the neon gas target, obtained at E_p = 7.11 MeV with a 1.5 mm thick silicon counter at 35^o (lab). The excitation energies of the final states in ^{20}Ne and ^{22}Ne are given in MeV. The elastic scattering peak contains a contribution from the 10% natural abundance of ^{22}Ne. The rise in the spectrum at low energies is due to neutron and gamma-ray background. For further discussion, see Page 29.

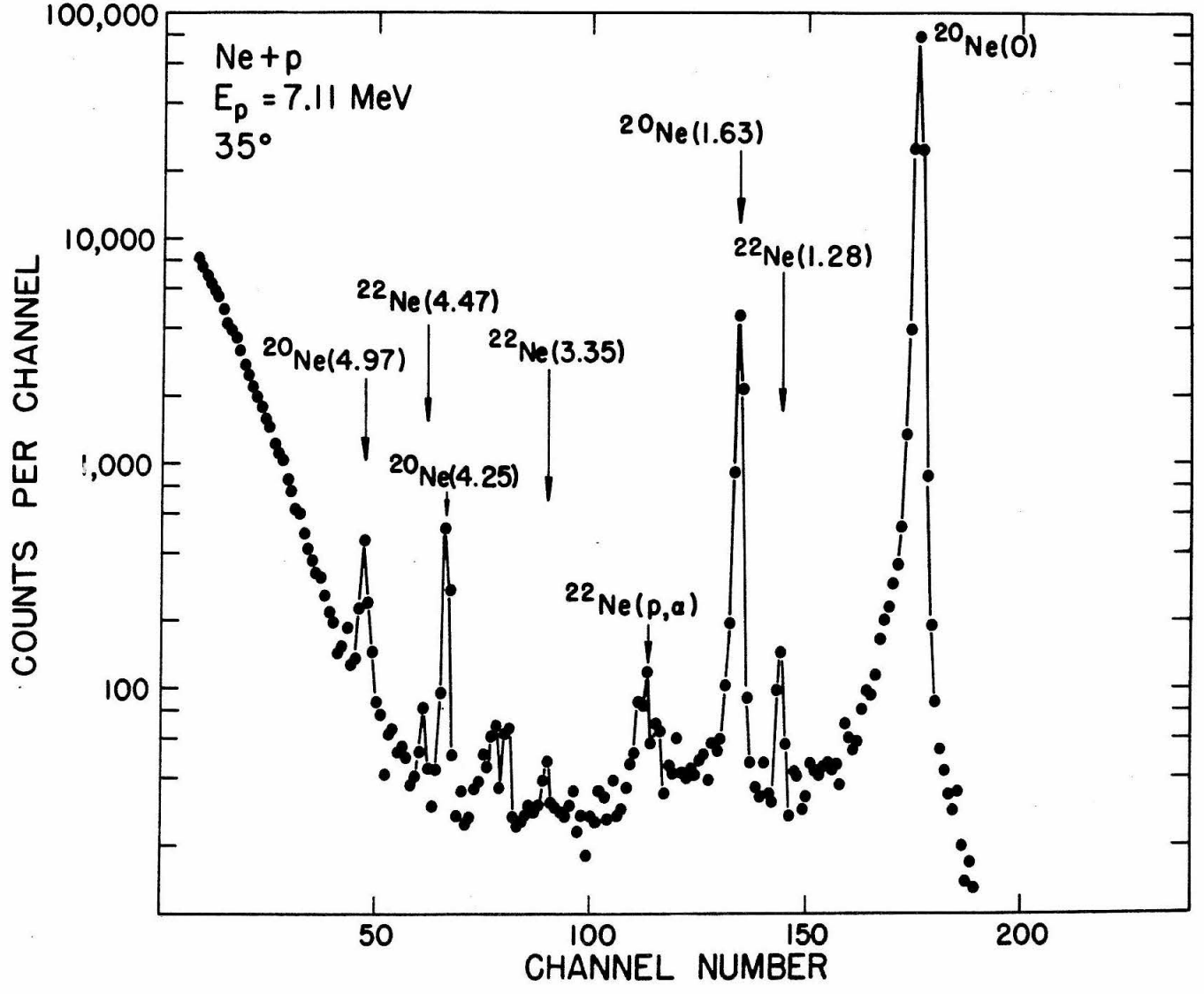
Ne + p
E_p = 7.11 MeV
35°
^{20}Ne(0)
^{20}Ne(1.63)
^{22}Ne(1.28)
^{22}Ne(4.47)
^{20}Ne(4.97)
^{22}Ne(3.35)
^{20}Ne(4.25)
^{22}Ne(p,α)
100,000
10,000
1,000
100
COUNTS PER CHANNEL
50
100
150
200
CHANNEL NUMBER

FIGURE 13

Excitation function for $^{20}Ne(p,p)$ elastic scattering at $\theta_{CM} = 55^{o}$. The horizontal bars show the expected positions of the T = 3/2 levels as determined in Section II. Statistical errors are less than the size of the points. There is an uncertainty of ± 20% in the absolute normalization. See Page 30 for further discussion.

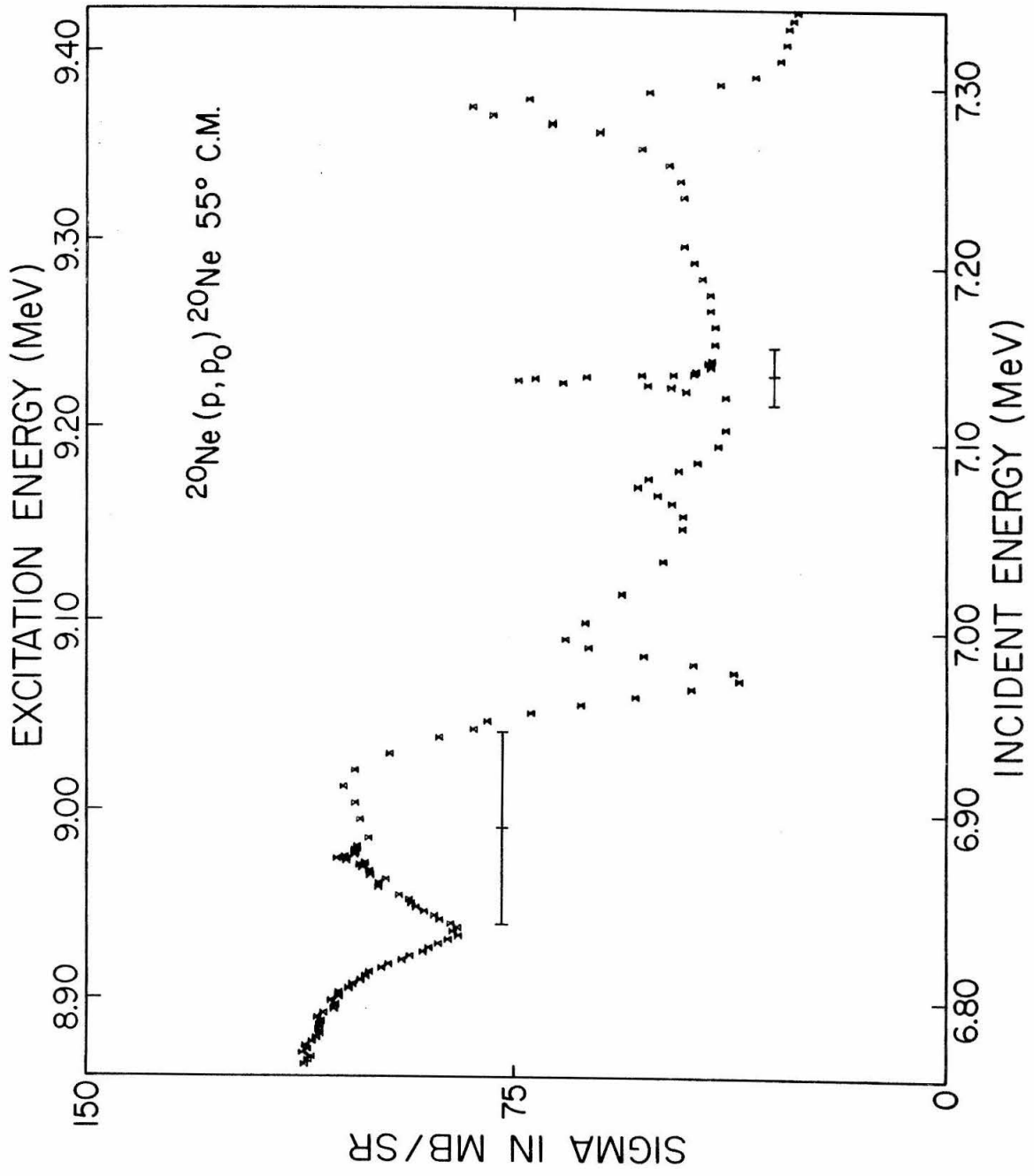
$^{20}Ne\,(p,p_0)\,^{20}Ne$ 55° C.M.
EXCITATION ENERGY (MeV)
8.90
9.00
9.10
9.20
9.30
9.40
INCIDENT ENERGY (MeV)
6.80
6.90
7.00
7.10
7.20
7.30
SIGMA IN MB/SR
150
75
0

FIGURE 14

Excitation function for $^{20}Ne(p,p)$ elastic scattering at $\theta_{CM} = 93^{o}$. The horizontal bars show the expected positions of the T = 3/2 levels as determined in Section II. Statistical errors are less than the size of the points. There is an uncertainty of ± 20% in the absolute normalization. See Page 30 for further discussion.

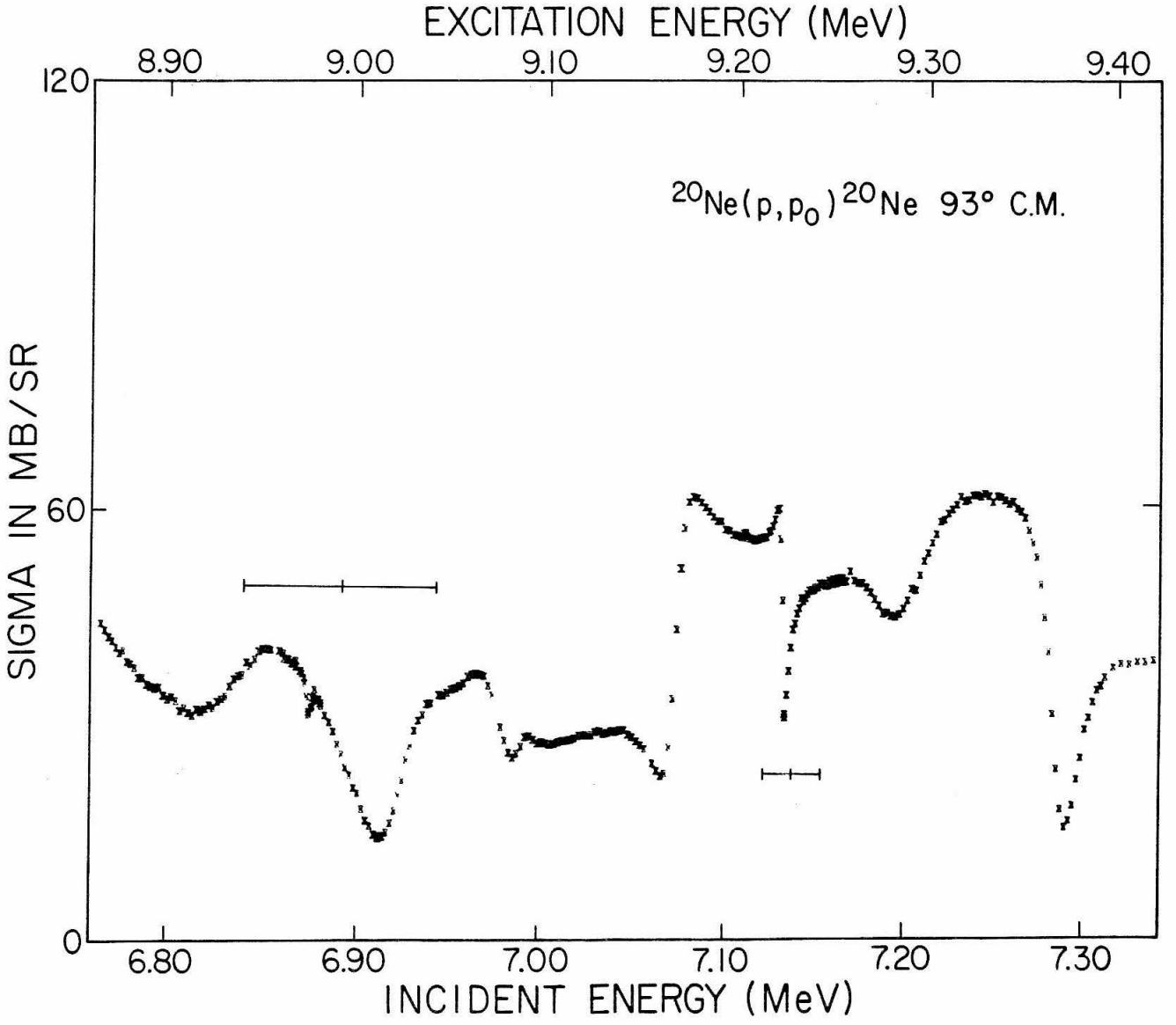
EXCITATION ENERGY (MeV)
8.90
9.00
9.10
9.20
9.30
9.40
120
60
0
SIGMA IN MB/SR
$^{20}Ne(p,p_0)^{20}Ne$ 93° C.M.
6.80
6.90
7.00
7.10
7.20
7.30
INCIDENT ENERGY (MeV)

FIGURE 15

Excitation function for $^{20}Ne(p,p)$ elastic scattering at $\theta_{CM} = 109^{o}$. The horizontal bars show the expected positions of the T = 3/2 levels as determined in Section II. Statistical errors are less than the size of the points. There is an uncertainty of ± 20% in the absolute normalization. See Page 30 for further discussion.

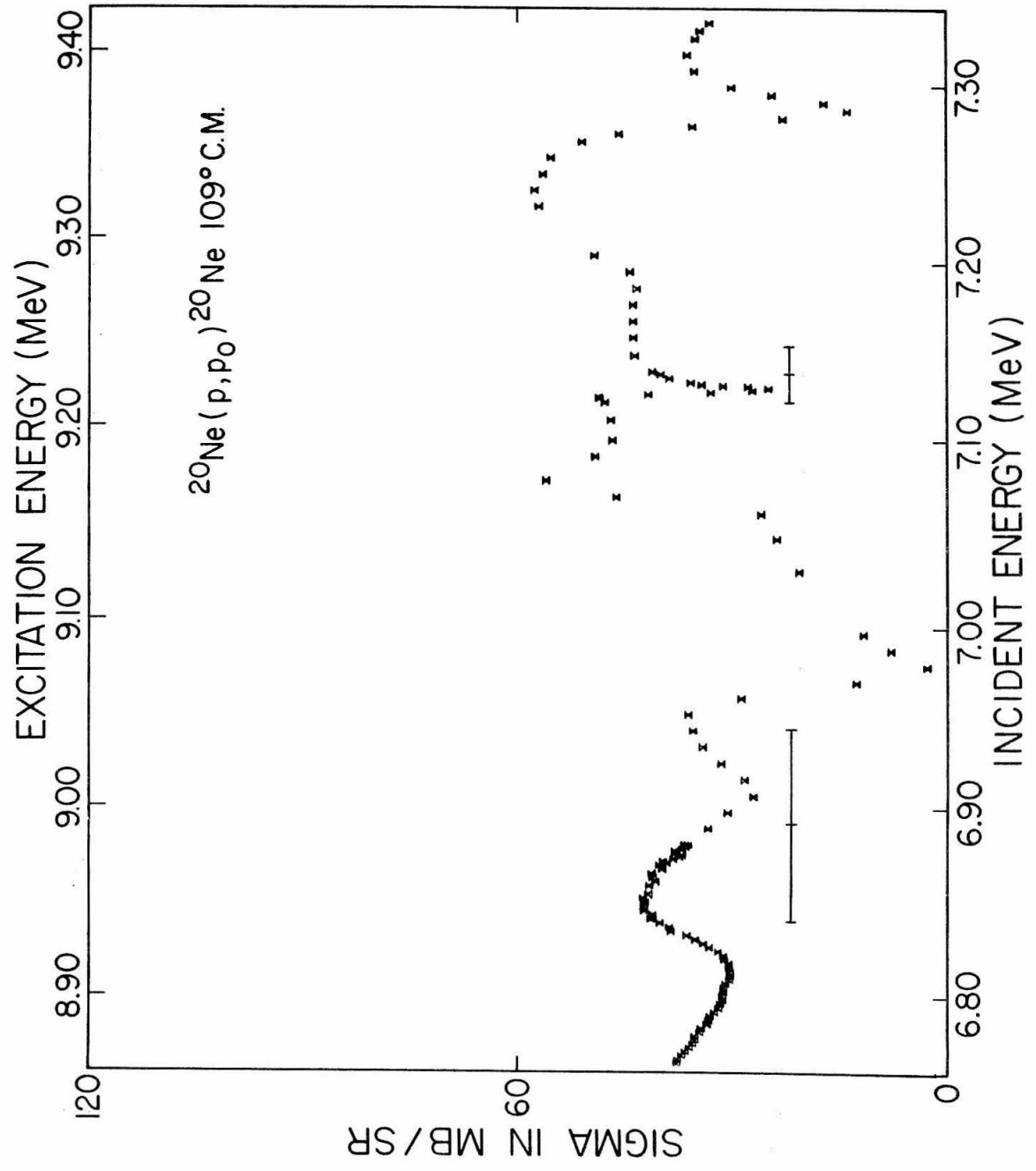
$^{20}Ne(p,p_0)^{20}Ne$ 109° C.M.
EXCITATION ENERGY (MeV)
8.90
9.00
9.10
9.20
9.30
9.40
INCIDENT ENERGY (MeV)
6.80
6.90
7.00
7.10
7.20
7.30
SIGMA IN MB/SR
0
60
120

FIGURE 16

Excitation function for $^{20}Ne(p,p)$ elastic scattering at $\theta_{CM} = 143^{o}$. The horizontal bars show the expected positions of the T = 3/2 levels as determined in Section II. Statistical errors are less than the size of the points. There is an uncertainty of ± 20% in the absolute normalization. See Page 30 for further discussion.

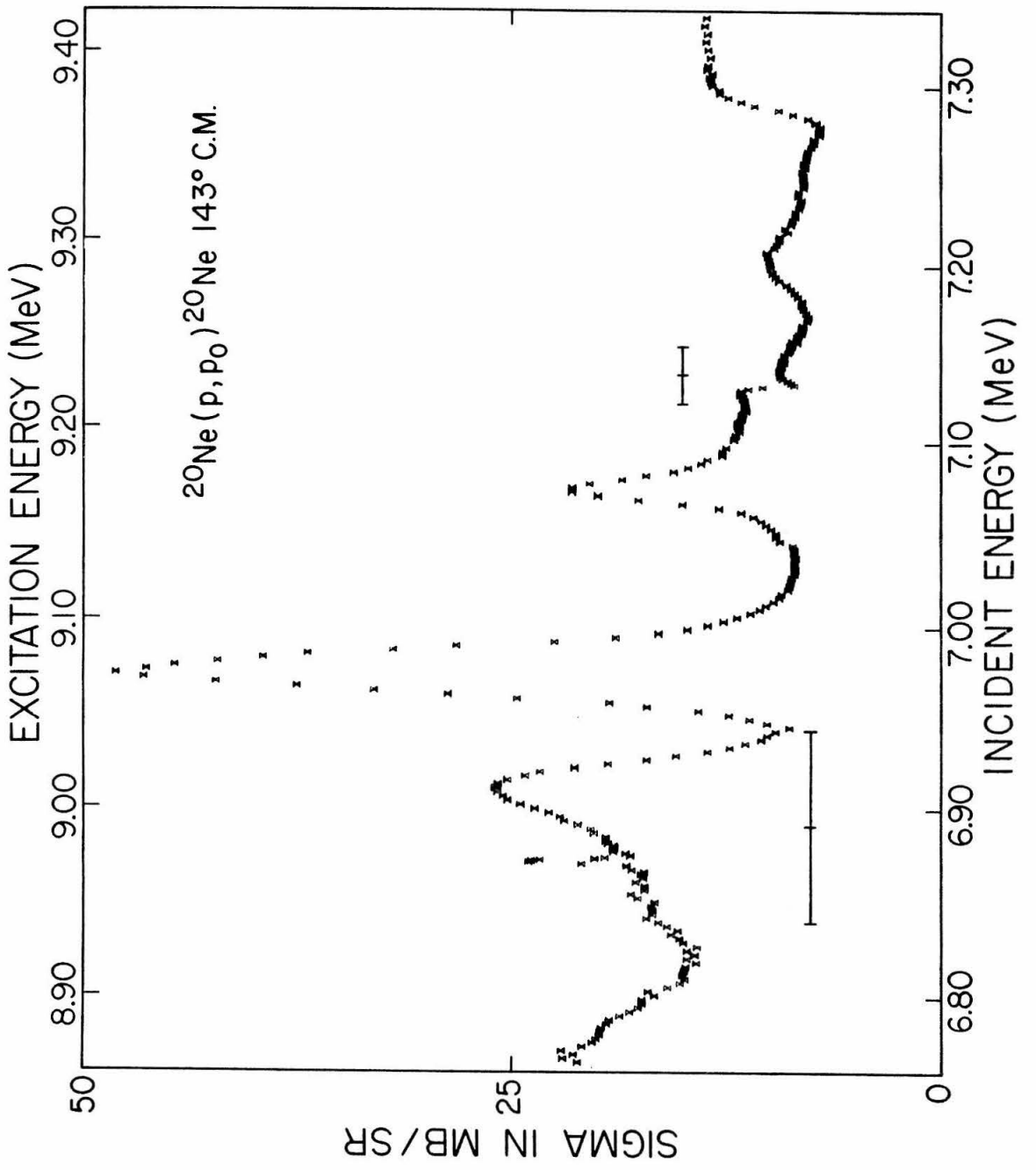
EXCITATION ENERGY (MeV)
8.90
9.00
9.10
9.20
9.30
9.40
$^{20}Ne(p,p_0)^{20}Ne$ 143° C.M.
SIGMA IN MB/SR
50
25
0
INCIDENT ENERGY (MeV)
6.80
6.90
7.00
7.10
7.20
7.30

FIGURE 17

Excitation function for $^{20}Ne(p,p)$ elastic scattering at $\theta_{CM} = 163^{o}$. The horizontal bars show the expected positions of the T = 3/2 levels as determined in Section II. Statistical errors are less than the size of the points. There is an uncertainty of ± 20% in the absolute normalization. See Page 30 for further discussion.

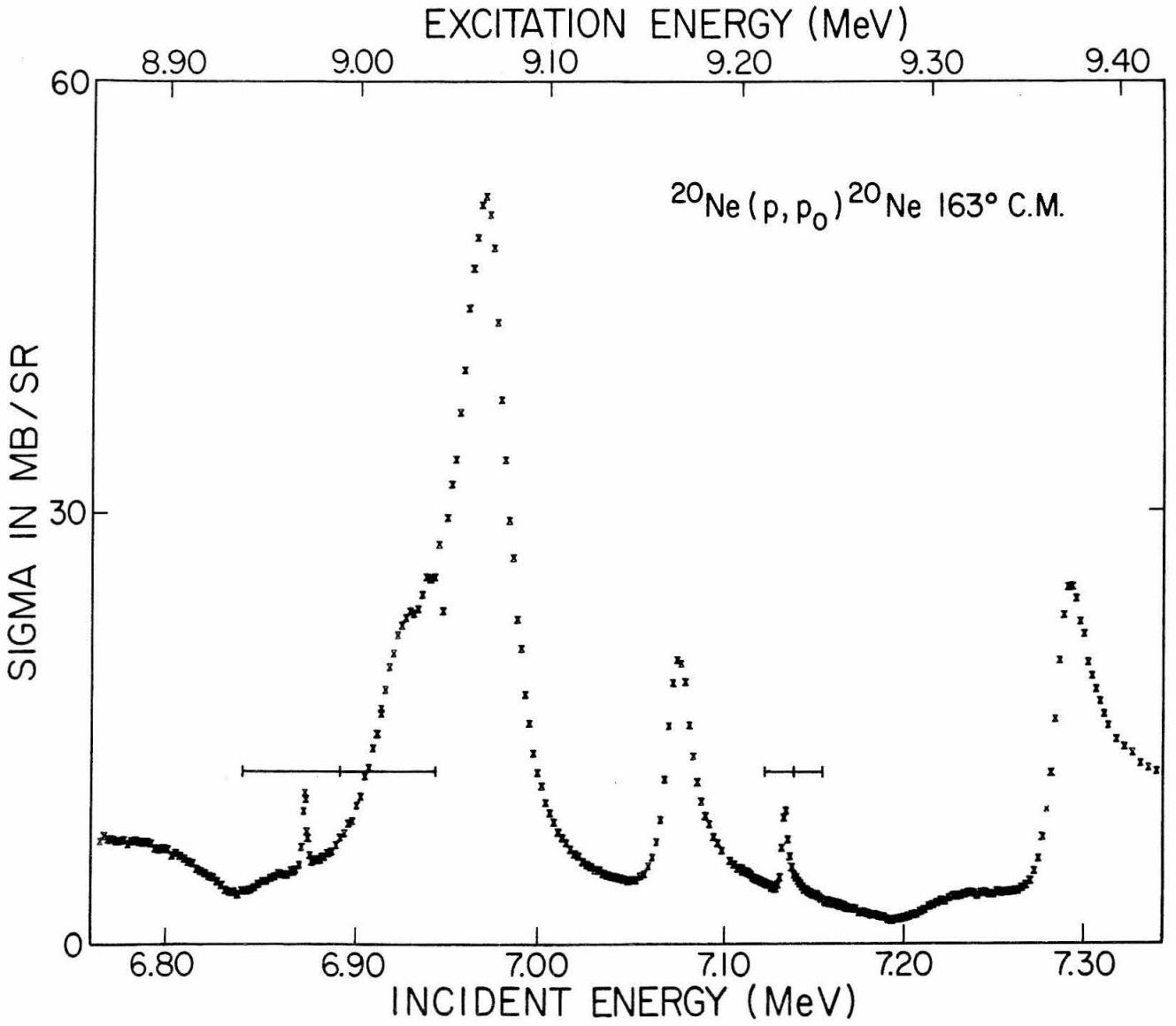
EXCITATION ENERGY (MeV)
8.90
9.00
9.10
9.20
9.30
9.40
60
30
0
SIGMA IN MB/SR
$^{20}Ne(p,p_0)^{20}Ne$ 163° C.M.
6.80
6.90
7.00
7.10
7.20
7.30
INCIDENT ENERGY (MeV)

FIGURE 18

Excitation functions for the $^{20}Ne(p,p_1)^{20}Ne$ (1.63) reaction over the regions of incident energy covering the resonances corresponding to the lowest two T = 3/2 levels in ^{21}Na (see Page 31). The resonances were observed at 6.872 ± 0.005 MeV and 7.128 ± 0.005 MeV incident energy in the elastic scattering data. There is an uncertainty of ± 20% in the absolute normalization.

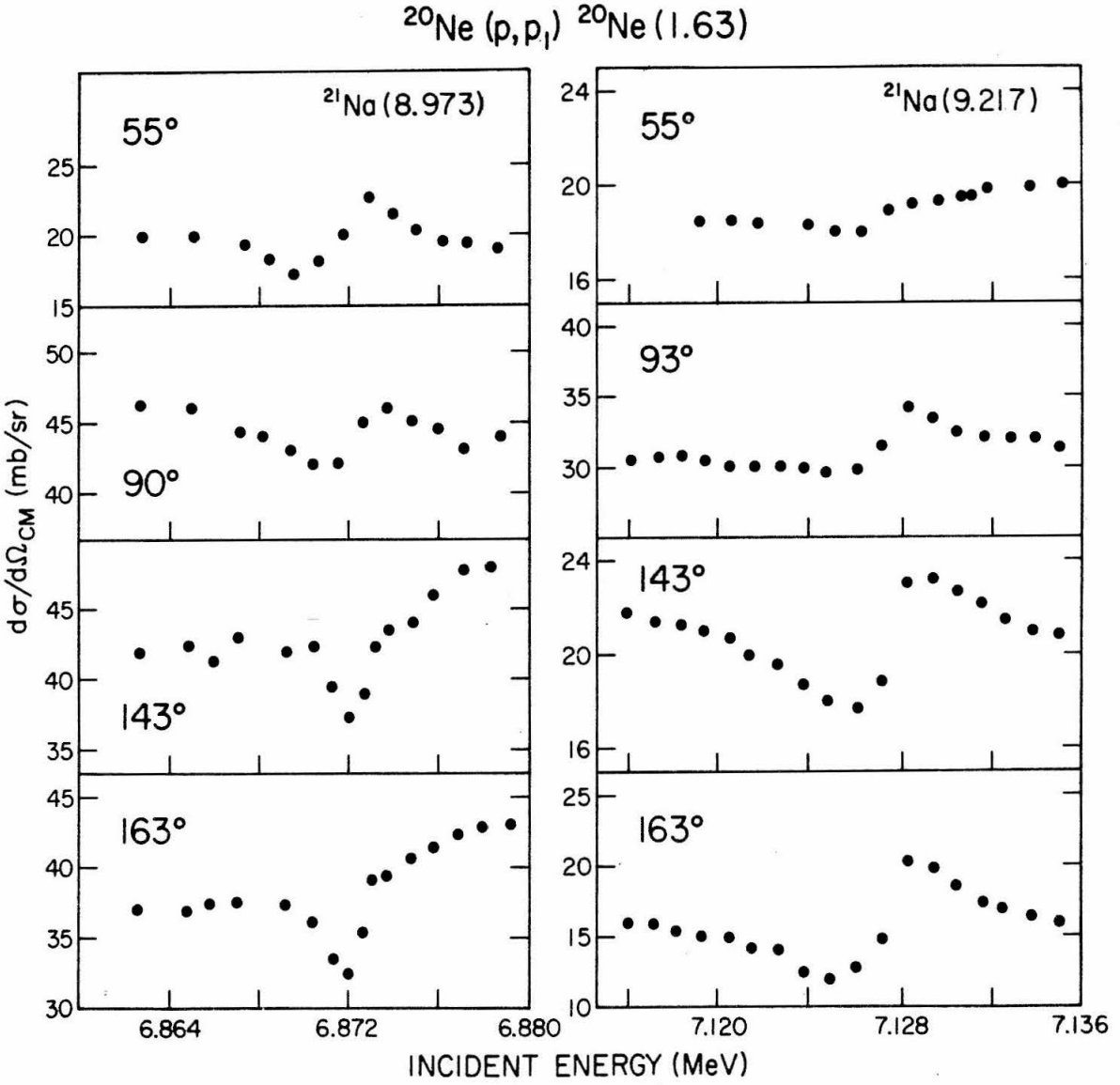
^{20}Ne (p, p$_1$) ^{20}Ne (1.63)
^{21}Na (8.973)
^{21}Na (9.217)
55°
55°
90°
93°
143°
143°
163°
163°
dσ/dΩ$_{CM}$ (mb/sr)
INCIDENT ENERGY (MeV)
6.864
6.872
6.880
7.120
7.128
7.136

FIGURE 19

Excitation function for the $^{20}Ne(p,p_2)^{20}Ne$ (4.25) reaction over the regions of incident energy covering the resonances corresponding to the lowest two T = 3/2 levels in ^{21}Na (see Page 31). The resonances were observed at 6.872 ± 0.005 MeV and 7.128 ± 0.005 MeV incident energy in the elastic scattering data. The data include a contribution from the background due to neutrons and gamma rays in the energy spectra from the silicon detector (see Figure 12).

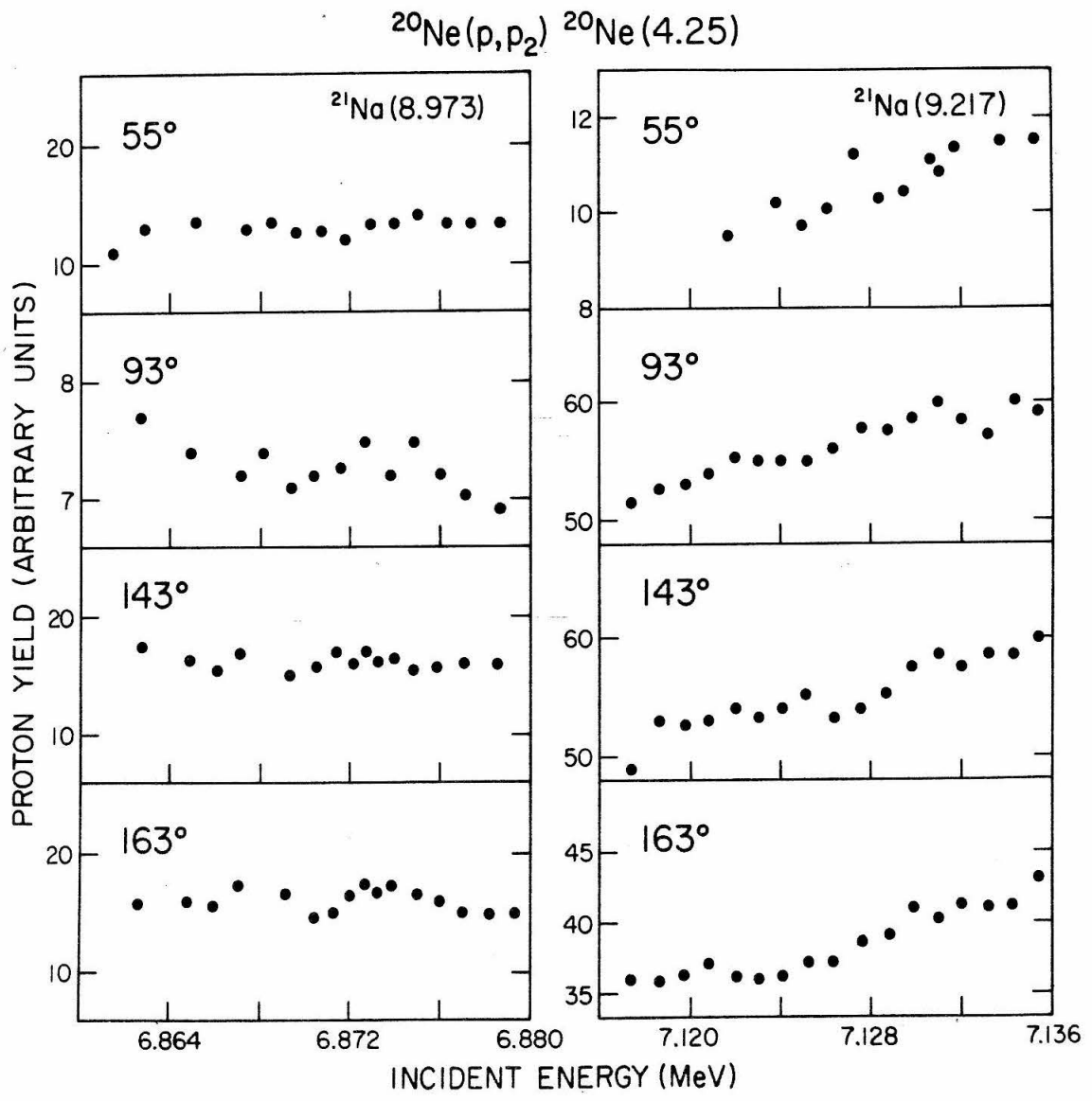
$^{20}Ne(p,p_2)\ ^{20}Ne(4.25)$
$^{21}Na(8.973)$
$^{21}Na(9.217)$
55°
93°
143°
163°
PROTON YIELD (ARBITRARY UNITS)
INCIDENT ENERGY (MeV)
6.864
6.872
6.880
7.120
7.128
7.136

FIGURE 20

Excitation function for the $^{20}Ne(p,p_3)^{20}Ne$ (4.97) reaction over the regions of incident energy covering the resonances corresponding to the lowest two T = 3/2 levels in ^{21}Na (see Page 31). The resonances were observed at 6.872 ± 0.005 MeV and 7.128 ± 0.005 MeV incident energy in the elastic scattering data. The data include a contribution from the background due to neutrons and gamma rays in the energy spectra from the silicon detector (see Figure 12).

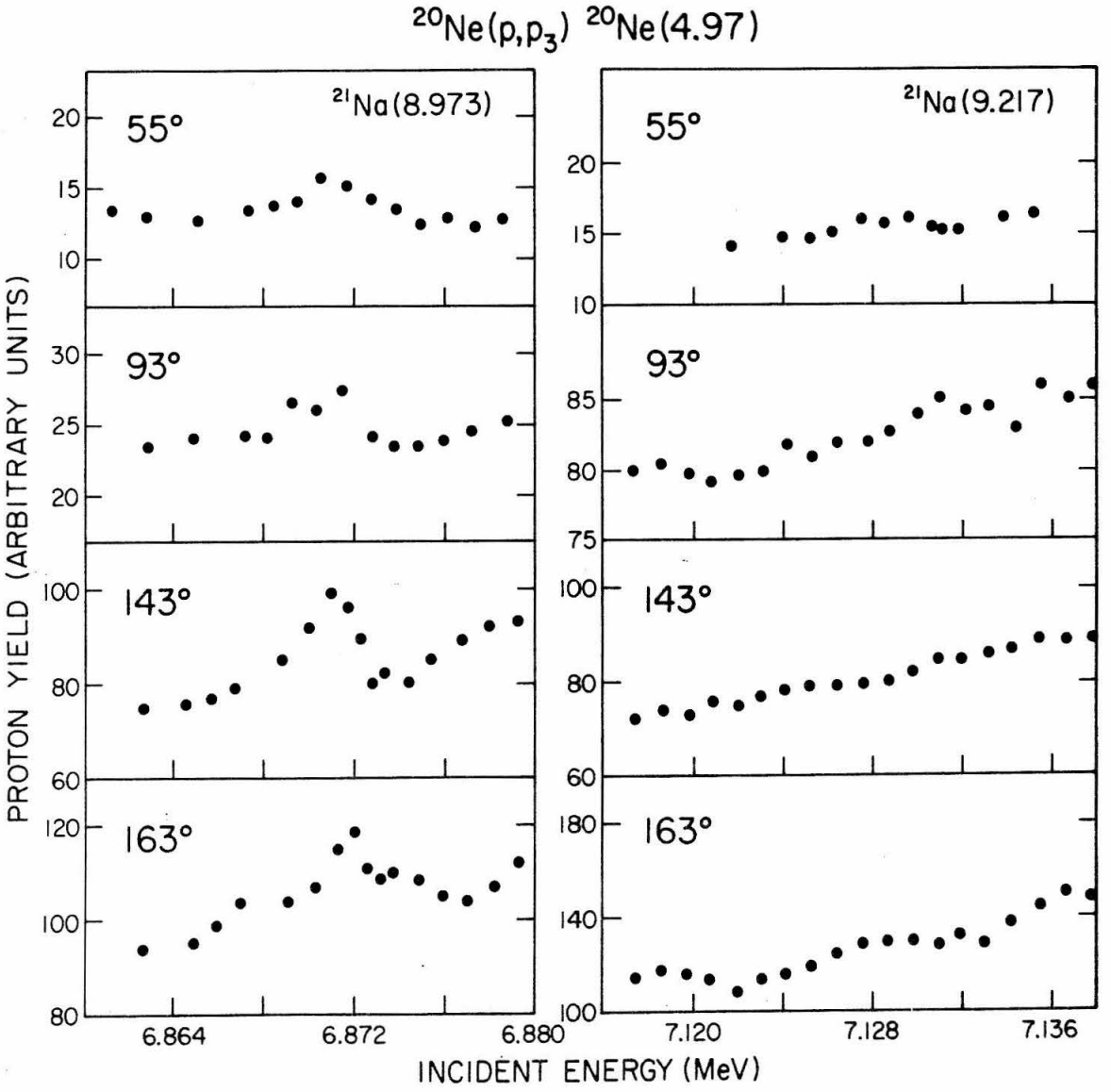
$^{20}Ne(p,p_3)$ $^{20}Ne(4.97)$
$^{21}Na(8.973)$
$^{21}Na(9.217)$
55°
93°
143°
163°
PROTON YIELD (ARBITRARY UNITS)
INCIDENT ENERGY (MeV)
6.864
6.872
6.880
7.120
7.128
7.136

FIGURE 21

Excitation functions for (A) the $^{20}Ne(p,p_1)^{20}Ne(1.63)$ reaction and (B) the $^{20}Ne(p,p_2)^{20}Ne(4.25)$ reaction at 163^{o} (C.M.) (see Page 31). The data in Part (B) include a contribution from the background due to neutrons and gamma rays in the energy spectra from the silicon detector (see Figure 12). The absolute normalization is accurate to ± 25%.

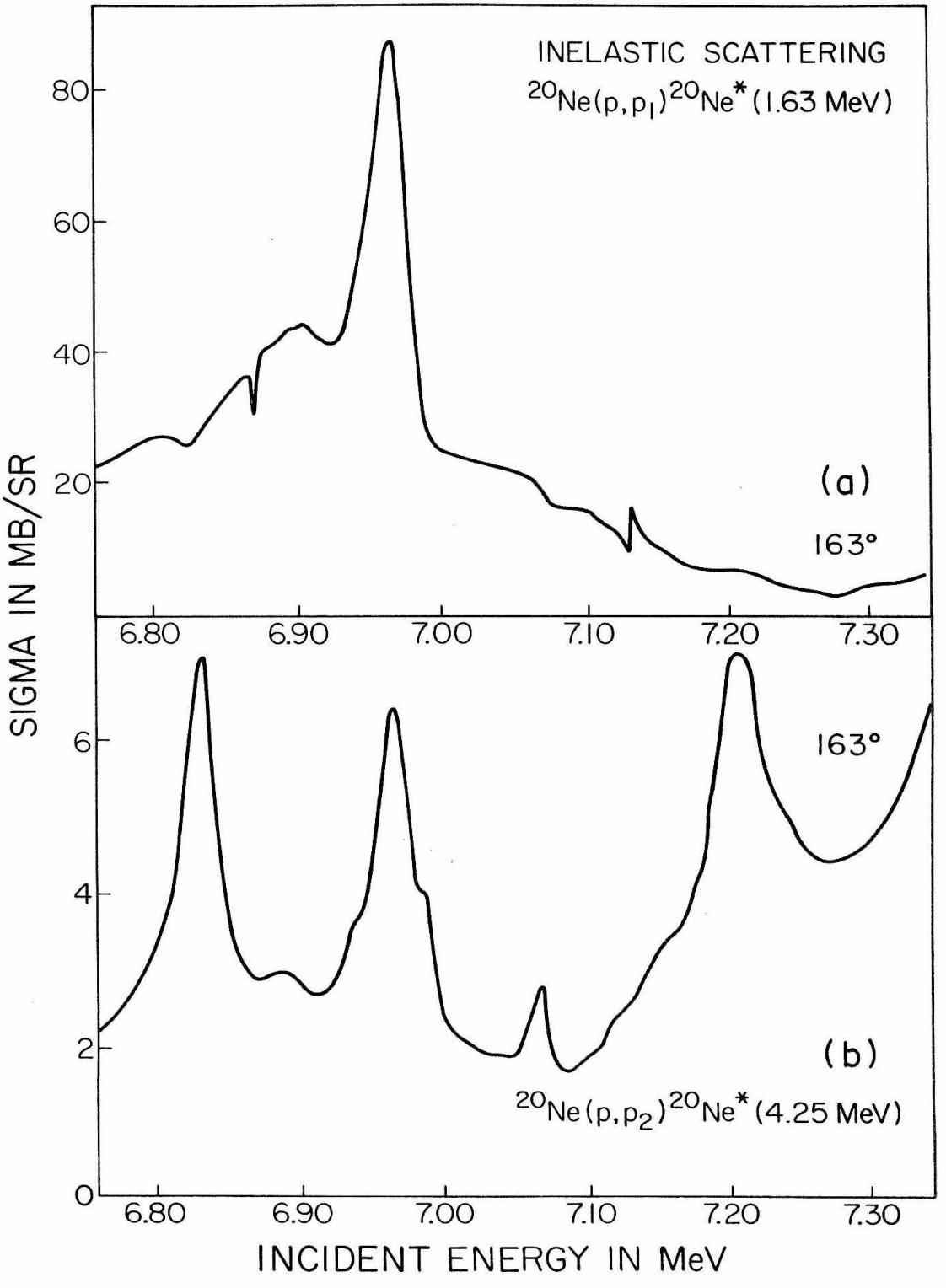
INELASTIC SCATTERING
$^{20}Ne(p,p_1)^{20}Ne^*$ (1.63 MeV)
(a)
163°
(b)
163°
$^{20}Ne(p,p_2)^{20}Ne^*$ (4.25 MeV)
SIGMA IN MB/SR
INCIDENT ENERGY IN MeV
0
2
4
6
20
40
60
80
6.80
6.90
7.00
7.10
7.20
7.30

FIGURE 22

Angular distributions measured on either side of the two T = 3/2 anomalies. The statistical errors in the data are less than the size of the points; the absolute error is ± 20%. The arrows indicate the angles at which the elastic scattering data presented in Figures 13 to 17 were taken. The solid curves are calculated from the real, ℓ-dependent background phase shifts listed in Table 3, A. The dashed curve is calculated from the complex, J-dependent phase shifts listed in Table 3, B. For further discussion, see Page 33.

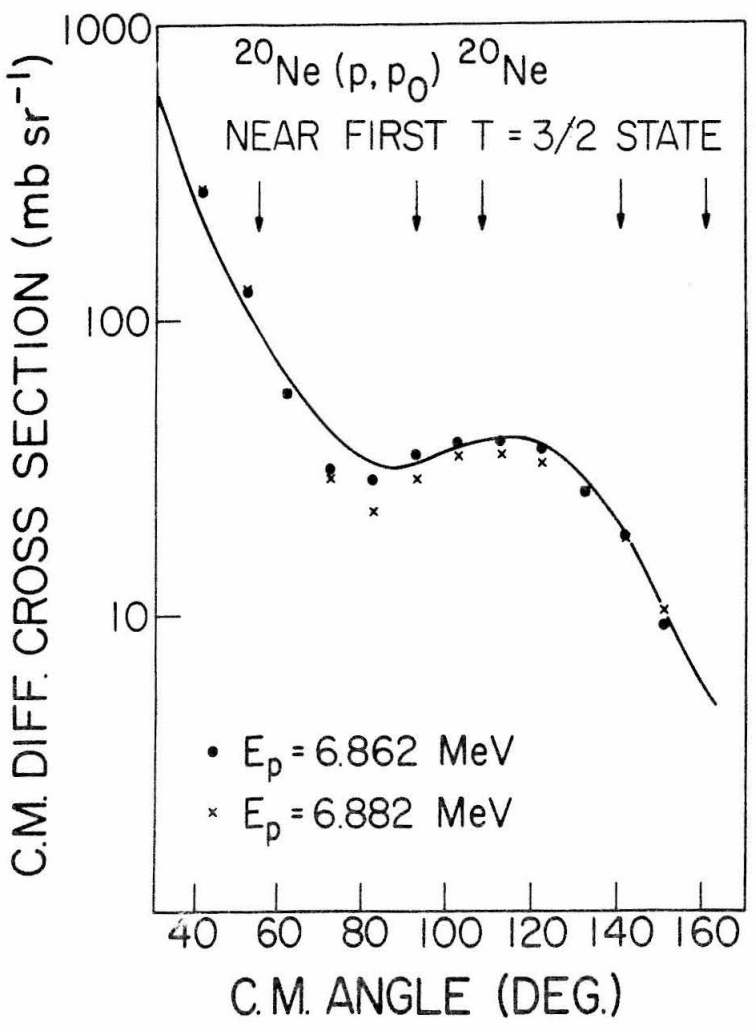
^{20}Ne (p, p$_0$) ^{20}Ne
NEAR FIRST T = 3/2 STATE
C.M. DIFF. CROSS SECTION (mb sr^{-1})
1000
100
10
• E$_p$ = 6.862 MeV
× E$_p$ = 6.882 MeV
40 60 80 100 120 140 160
C.M. ANGLE (DEG.)

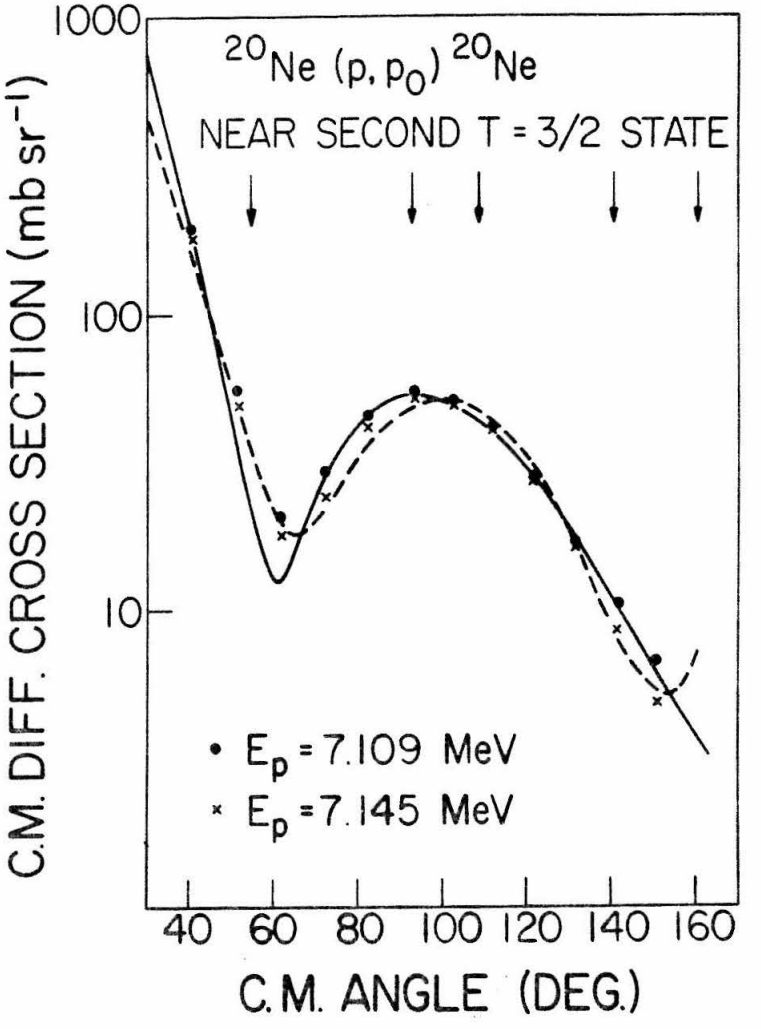
^{20}Ne (p, p$_0$) ^{20}Ne
NEAR SECOND T = 3/2 STATE
C.M. DIFF. CROSS SECTION (mb sr^{-1})
1000
100
10
• E$_p$ = 7.109 MeV
× E$_p$ = 7.145 MeV
40 60 80 100 120 140 160
C.M. ANGLE (DEG.)

FIGURE 23

Single level resonance shapes for the $^{20}Ne(p,p_o)^{20}Ne$ reaction at E_p = 7.1 MeV and 55^o, 93^o, 143^o and 163^o (C.M.) for all the values of J^π formed with $\ell \leq 4$. The real, ℓ-dependent background phase shifts used were: $\delta_0 = -63^o$, $\delta_1 = -30^o$, $\delta_2 = -8.6^o$, $\delta_3 = -1.4^o$ and $\delta_4 = -0.2^o$. The individual shapes have been normalized to have the value 100 at the resonance energy. For further discussion, see Page 34.

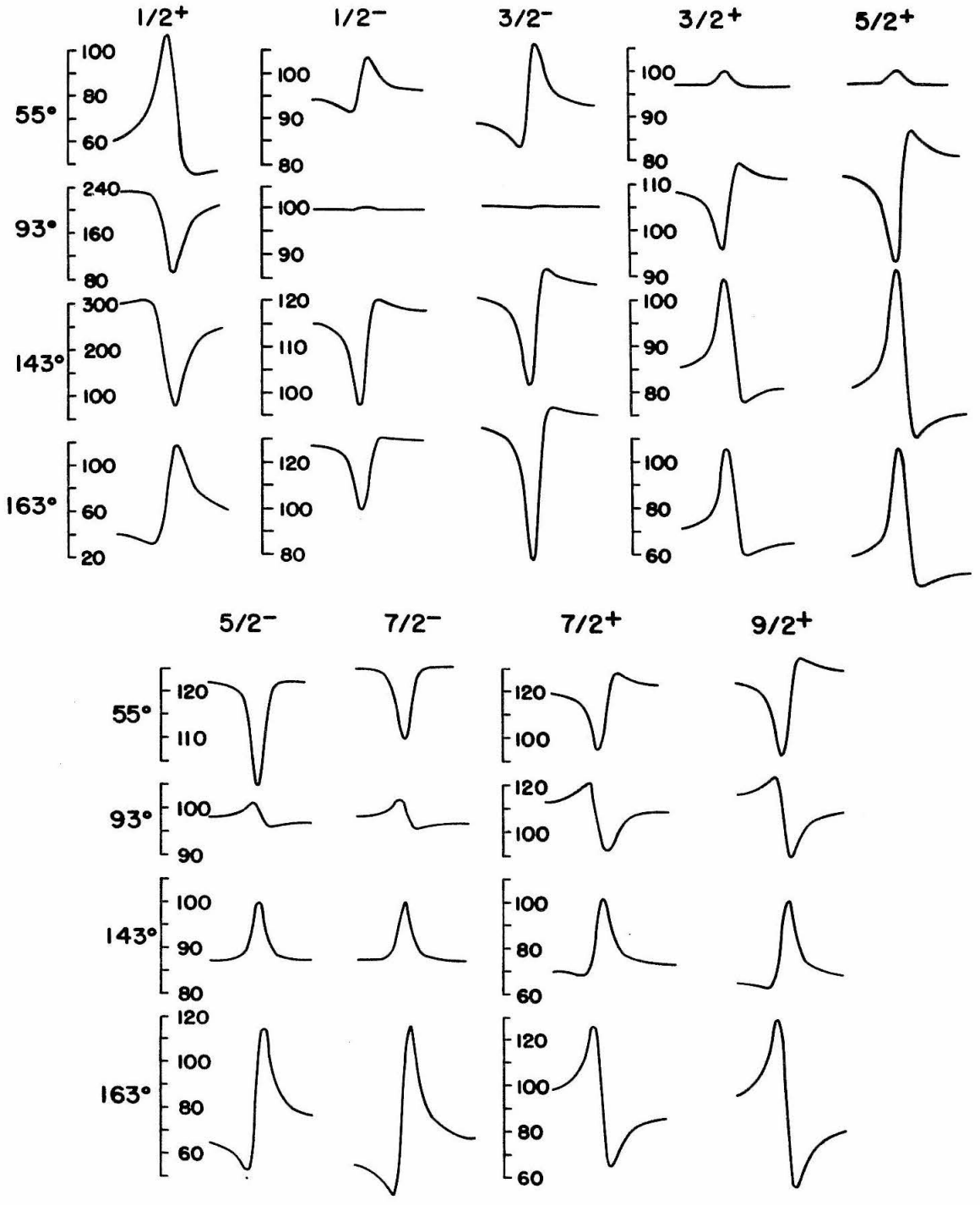

RESONANCE SHAPES FOR $^{20}Ne(p,p)$ AT $E_p = 7$ MeV

FIGURE 24

Excitation functions for the $^{20}Ne(p,p_o)^{20}Ne$ reaction over the resonance corresponding to the 8.973, T = 3/2 level of ^{21}Na. Statistical errors in the data are less than the size of the points; there is an uncertainty in the absolute normalization of ± 20%. The solid curves are calculated from the expressions discussed on Page 31, with $J^{\pi} = 5/2^{+}$, $E_o^{lab} = 6.872$ $\Gamma = 0.5$ keV, $\Gamma_{p_o} = 0.1$ keV, R = 2.0 keV, using the non-resonant background phase shifts listed in Table 3, A. For further discussion, see Page 35.

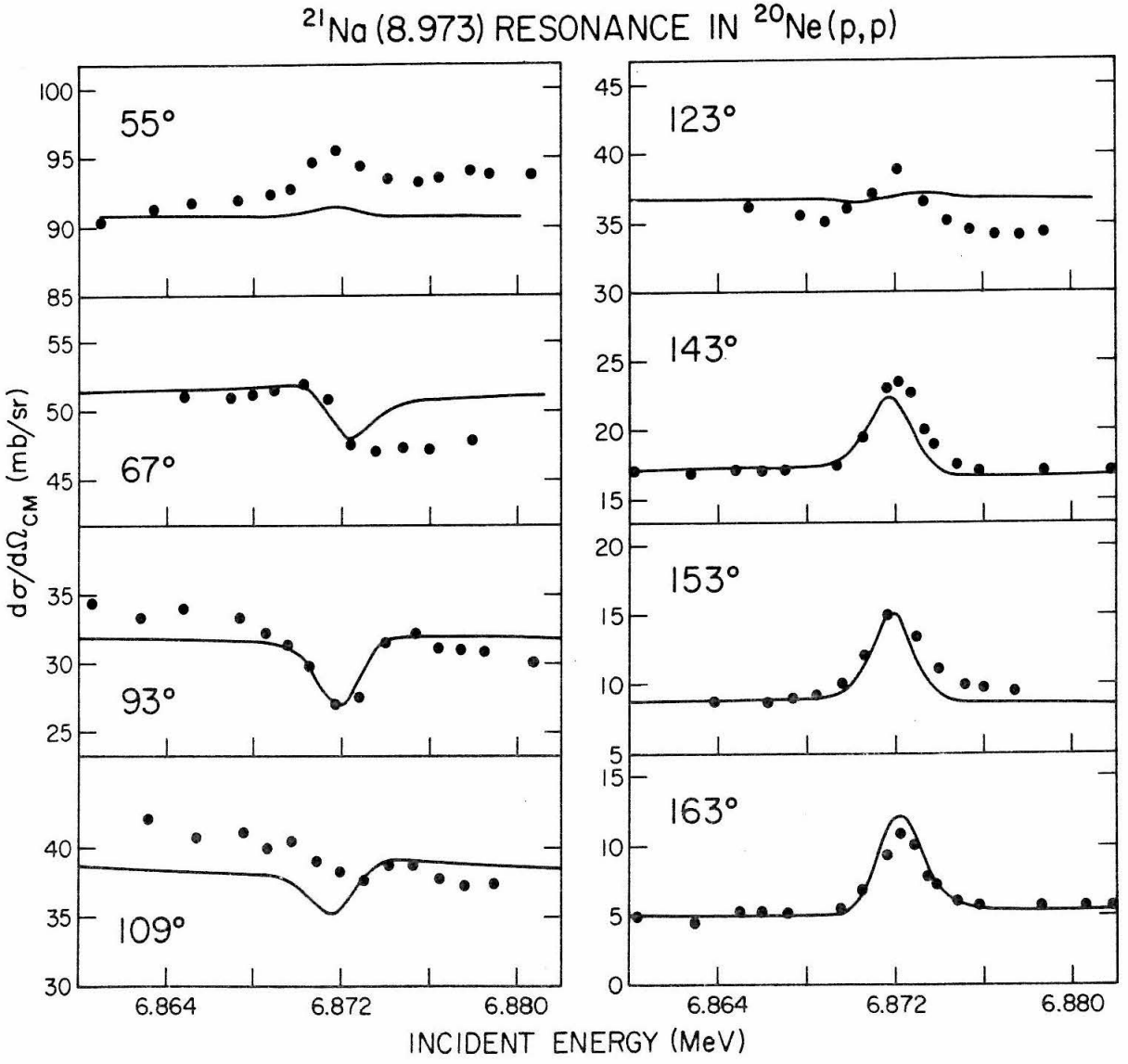
^{21}Na (8.973) RESONANCE IN ^{20}Ne(p,p)
55°
67°
93°
109°
123°
143°
153°
163°
dσ/dΩ$_{CM}$ (mb/sr)
INCIDENT ENERGY (MeV)
6.864
6.872
6.880

FIGURE 25

Excitation functions for the $^{20}Ne(p,p_o)^{20}Ne$ reaction over the resonance corresponding to the 9.217 MeV, T = 3/2 level of ^{21}Na. Statistical errors in the data are less than the size of the points; there is an uncertainty in the absolute normalization of ± 20%. The curves are calculated from the expressions discussed on page 31, with $J^{\pi} = 1/2^{+}$, $E_o^{lab} = 7.128$, $\Gamma = 2.3$ keV, $\Gamma_{p_o} = 1.1$ keV, R = 2 keV. The solid curves are calculated using the real, ℓ-dependent background phase shifts listed in Table 3, A and the dashed curves are calculated using the complex, J-dependent background phase shifts listed in Table 3, B. For further discussion, see Page 36.

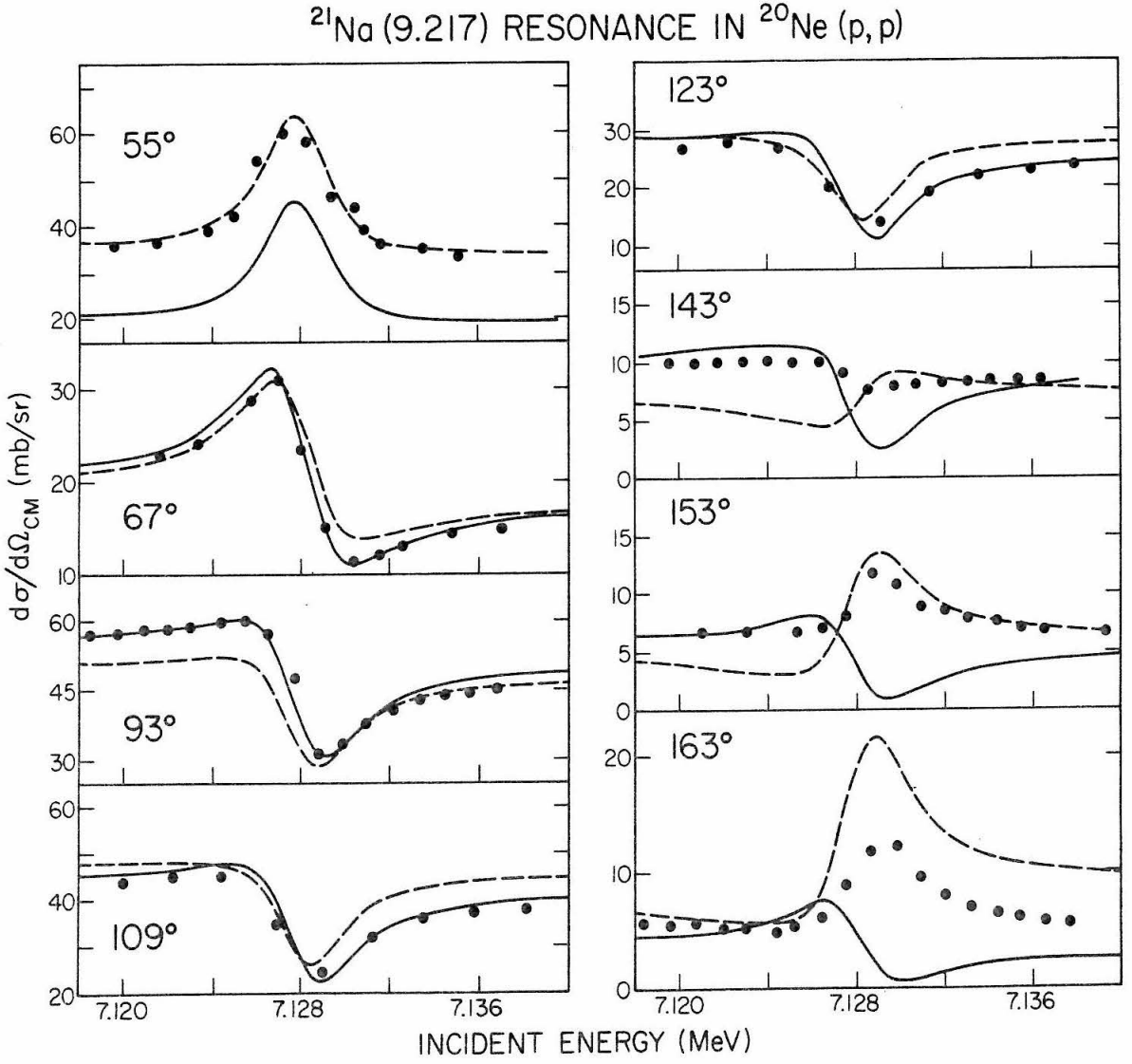
^{21}Na (9.217) RESONANCE IN ^{20}Ne (p, p)
55°
67°
93°
109°
123°
143°
153°
163°
dσ/dΩ$_{CM}$ (mb/sr)
INCIDENT ENERGY (MeV)
7.120
7.128
7.136

FIGURE 26

Excitation functions for the $^{20}Ne(p,p_o)^{20}Ne$ reaction at 163^o and 143^o (C.M.) over the resonance corresponding to the 8.973 MeV, T = 3/2 level of ^{21}Na, using the energy-compensation system described on page 28. Statistical errors in the data are less than the size of the points; there is an overall uncertainty of ± 20% in the absolute normalization. The solid curves are calculated from the expressions presented on Page 31, with $J^{\pi} = 5/2^+, E_o^{lab} = 6.872$, $\Gamma = 1.2$ keV, $\Gamma_{p_o} = 0.15$ keV, R = 0.7 keV, using the background phase shifts tabulated in Table 3, A. For further discussion, see Page 35.

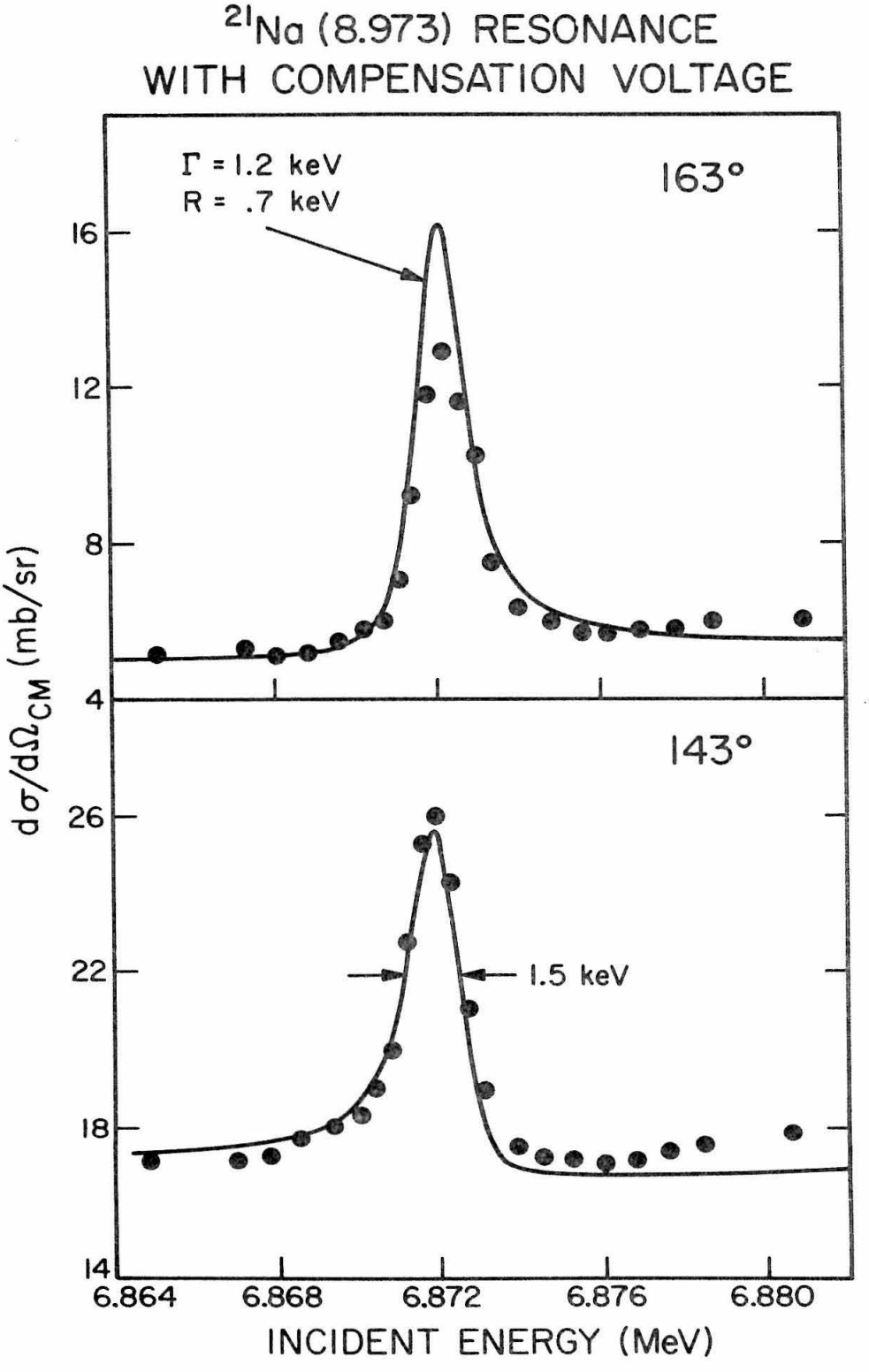
^{21}Na (8.973) RESONANCE
WITH COMPENSATION VOLTAGE
Γ = 1.2 keV
R = .7 keV
163°
143°
1.5 keV
16
12
8
4
26
22
18
14
6.864
6.868
6.872
6.876
6.880
INCIDENT ENERGY (MeV)
dσ/dΩ$_{CM}$ (mb/sr)

FIGURE 27

Mass 17 isobar diagram, illustrating some available modes for particle decay of the lowest T = 3/2 levels of ^{17}O and ^{17}F. For further discussion, see Pages 46 and 69.

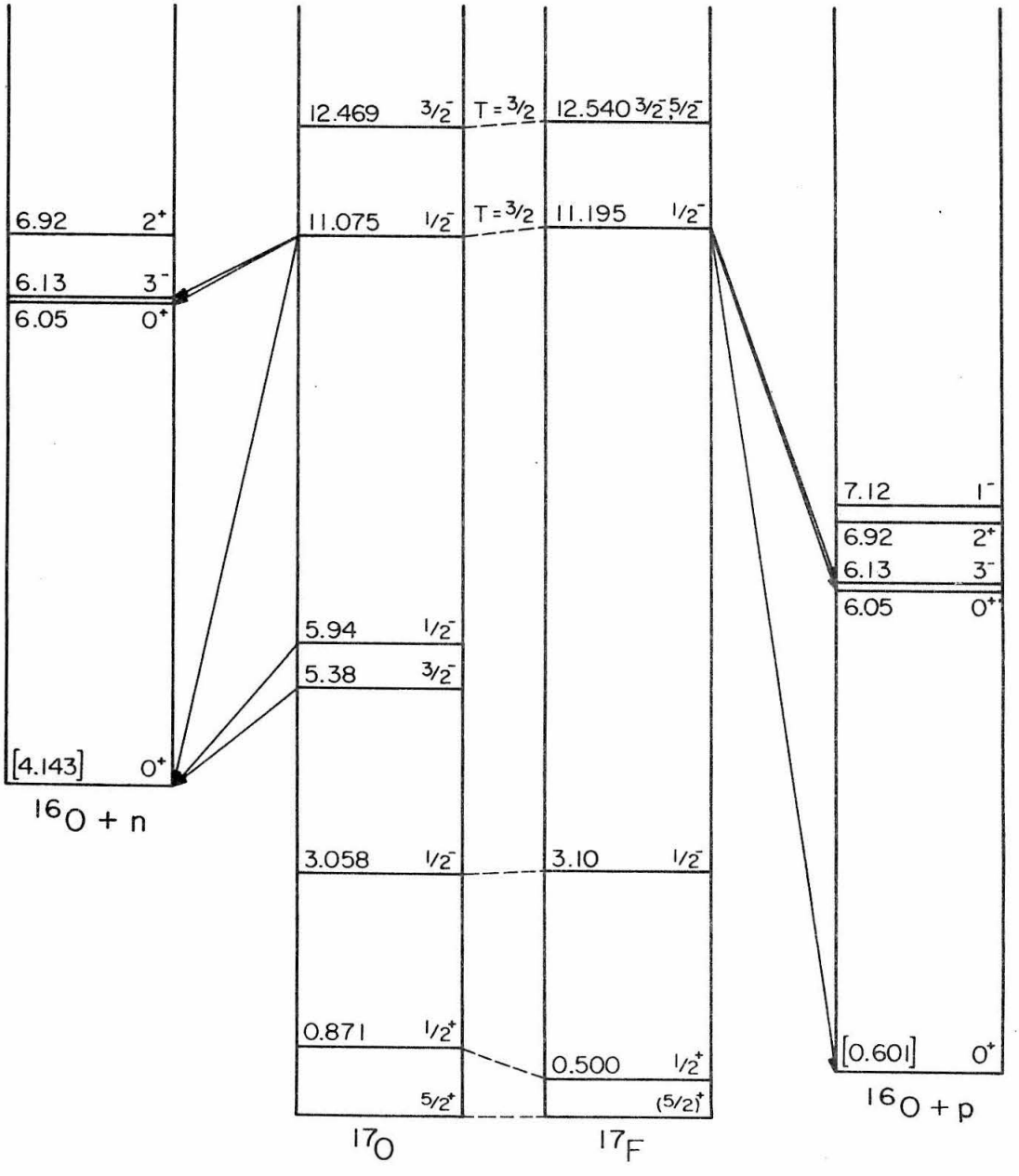
12.469 3/2⁻
T = 3/2
12.540 3/2⁻, 5/2⁻
6.92 2⁺
11.075 1/2⁻
T = 3/2
11.195 1/2⁻
6.13 3⁻
6.05 0⁺
7.12 1⁻
6.92 2⁺
6.13 3⁻
6.05 0⁺
5.94 1/2⁻
5.38 3/2⁻
[4.143] 0⁺
3.058 1/2⁻
3.10 1/2⁻
0.871 1/2⁺
0.500 1/2⁺
5/2⁺
(5/2)⁺
[0.601] 0⁺
16O + n
17O
17F
16O + p

FIGURE 28

The gas target cell used for the $^{15}N(^{3}He,n)^{17}F^{*}(p)^{16}O$ experiment described in Section IV. The 10,000 Å Ni foil was mounted off center so that the proton and neutron detectors both viewed the total volume of interaction between the beam and target gas. For further description see Page 46.

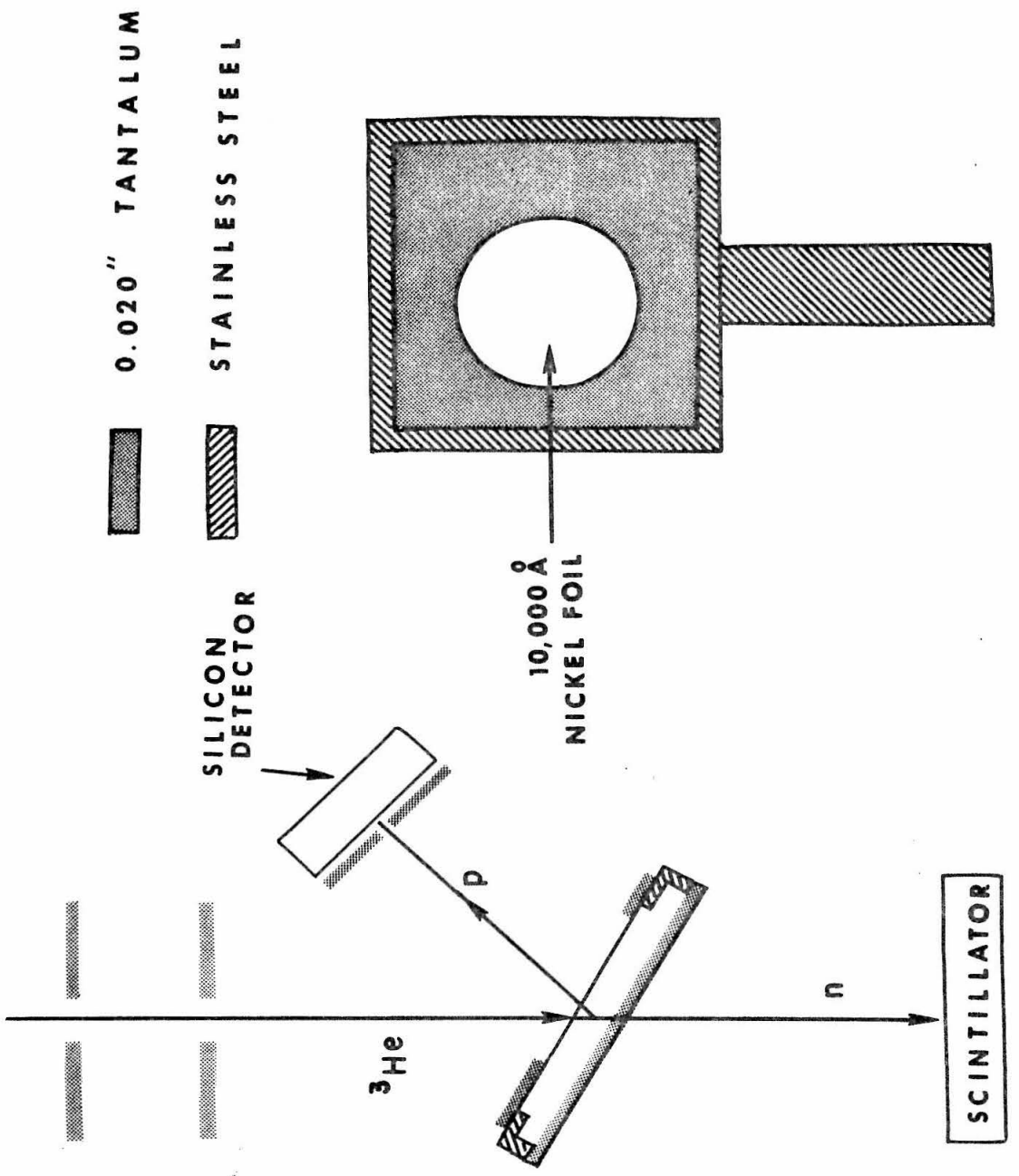
0.020" TANTALUM
STAINLESS STEEL
SILICON DETECTOR
10,000 Å NICKEL FOIL
p
^{3}He
n
SCINTILLATOR

FIGURE 29

Block diagram of the electronic circuitry used in the study of the $^{15}N(^{3}He,np)^{16}O$ reaction, described in Section IV. The commercially available instruments symbolized by the boxes are:

1. Time pick-off — Ortec Model 290.
2. Time-to-pulse-height converter — Ortec Model 437.
3. ddl amplifier — Ortec Model 410.
4. Single channel analyzer — Ortec Model 420.
5. Discriminator — Ortec Model 420.
6. Charge sensitive preamp — Ortec Model 109A.
7. Multichannel analyzer — Nuclear Data 64 × 64.
8. Slow coincidence — Ortec Model 409.

This circuitry is discussed on Page 47.

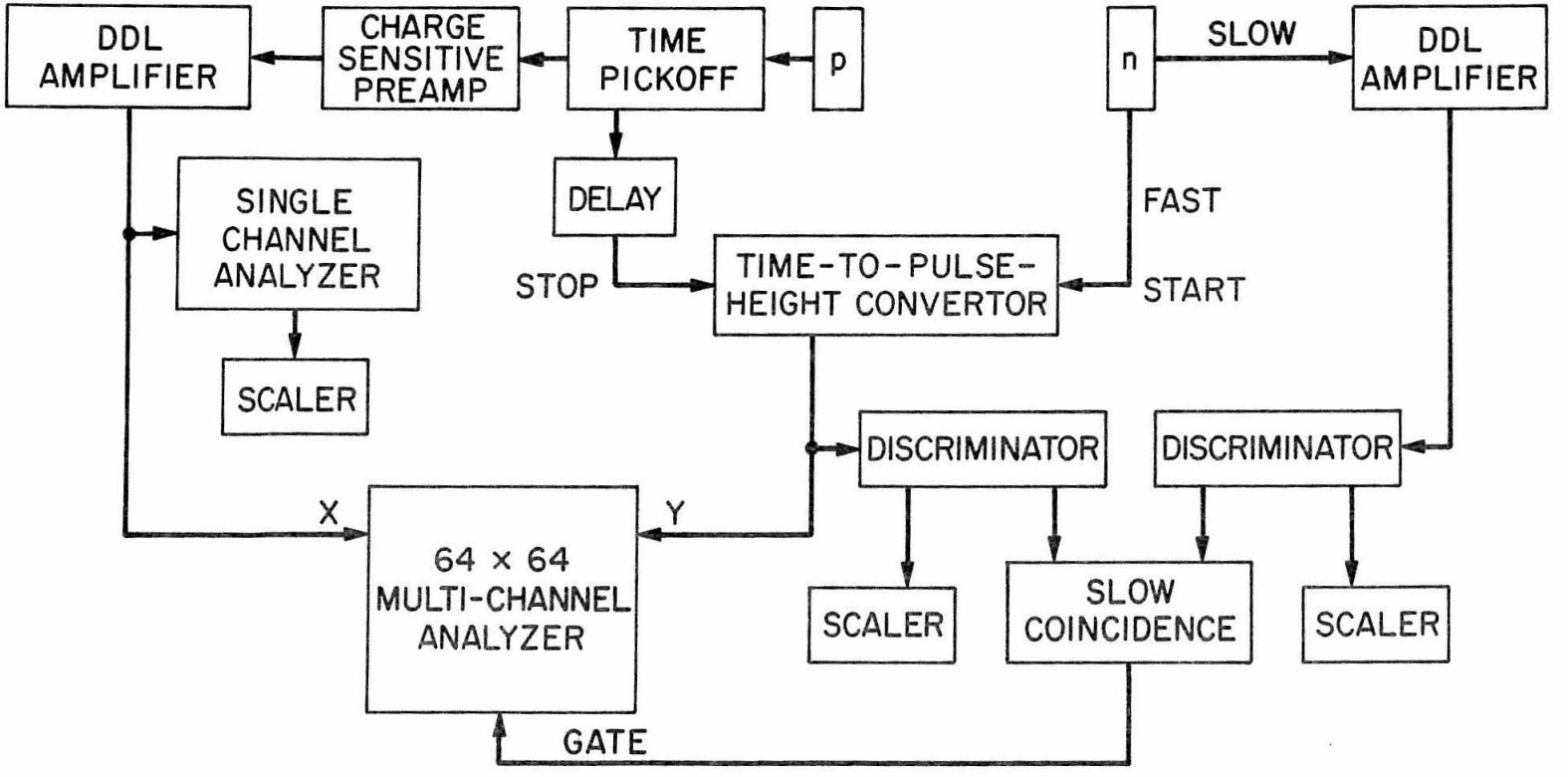
DDL AMPLIFIER
CHARGE SENSITIVE PREAMP
TIME PICKOFF
p
n
SLOW
DDL AMPLIFIER
SINGLE CHANNEL ANALYZER
DELAY
FAST
STOP
TIME-TO-PULSE-HEIGHT CONVERTOR
START
SCALER
DISCRIMINATOR
DISCRIMINATOR
X
Y
64 x 64 MULTI-CHANNEL ANALYZER
SCALER
SLOW COINCIDENCE
SCALER
GATE

FIGURE 30

Two dimensional spectrum of neutron flight time versus proton energy, from the $^{15}N(^{3}He,np)^{16}O$ reaction. Neutron flight time increases from bottom to top, and proton energy from left to right. For further discussion of this figure, see Page 48.

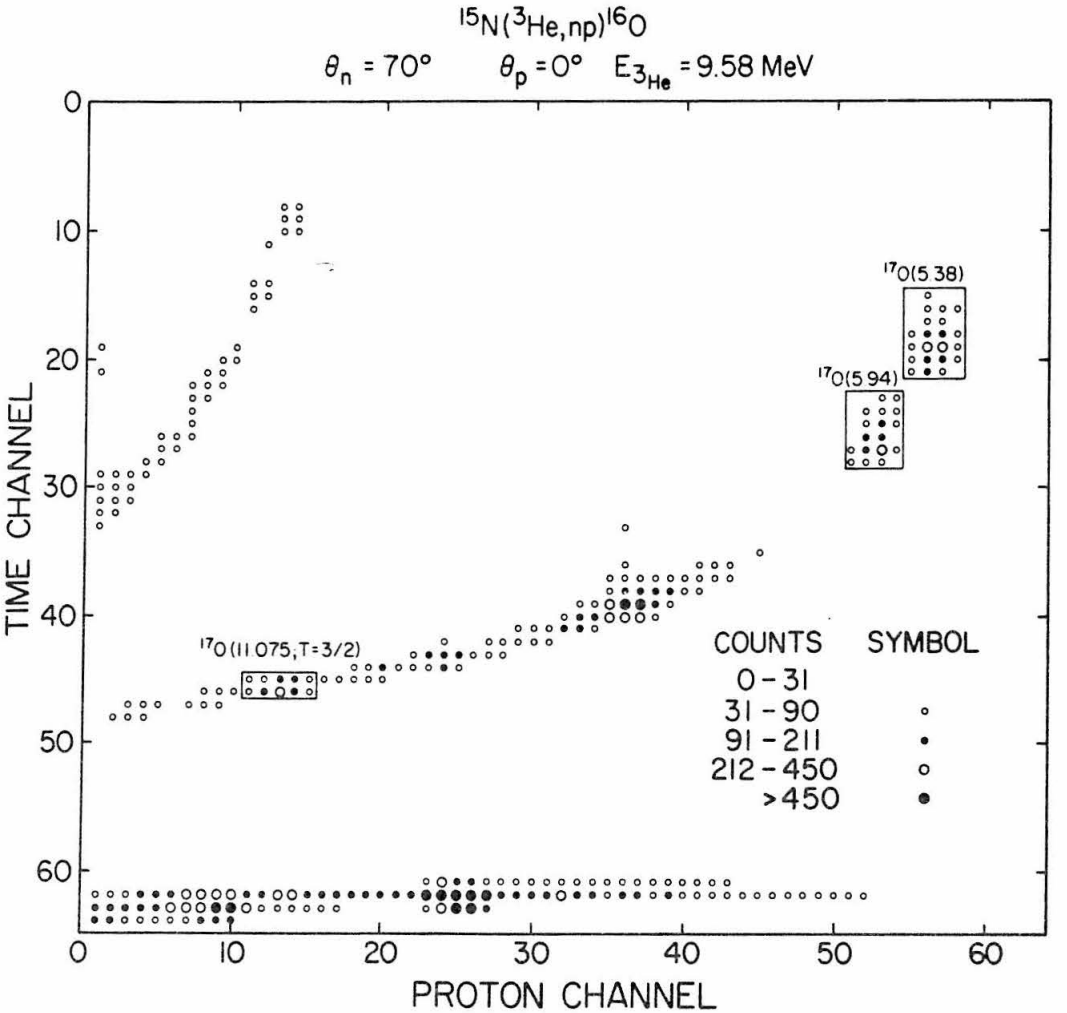
$^{15}N(^{3}He,np)^{16}O$
$\theta_n = 70°$ $\theta_p = 0°$ $E_{^3He} = 9.58$ MeV
TIME CHANNEL
PROTON CHANNEL
0
10
20
30
40
50
60
$^{17}O(5.38)$
$^{17}O(5.94)$
$^{17}O(11.075, T=3/2)$
COUNTS SYMBOL
0 - 31
31 - 90
91 - 211
212 - 450
>450

FIGURE 31

A. Neutron time-of-flight spectrum from the $^{15}N(^{3}He,n)^{17}F$ reaction at an incident energy of 8.44 MeV. The peak near channel 10 corresponds to the $^{17}F(11.195;\ T = 3/2)$ level. The peak near channel 76 is due to prompt gamma-rays.

B. Projection of the kinematic line from the $^{15}N(^{3}He,np)^{16}O(0.0)$ reaction on the neutron axis, with the same time scale as Part A. A peak which is assumed to be due to the decay of the $^{17}F(11.195;\ T = 3/2)$ level to $^{16}O(0.0) + p$, is observable near channel 10.

For further discussion of these spectra, see Page 52.

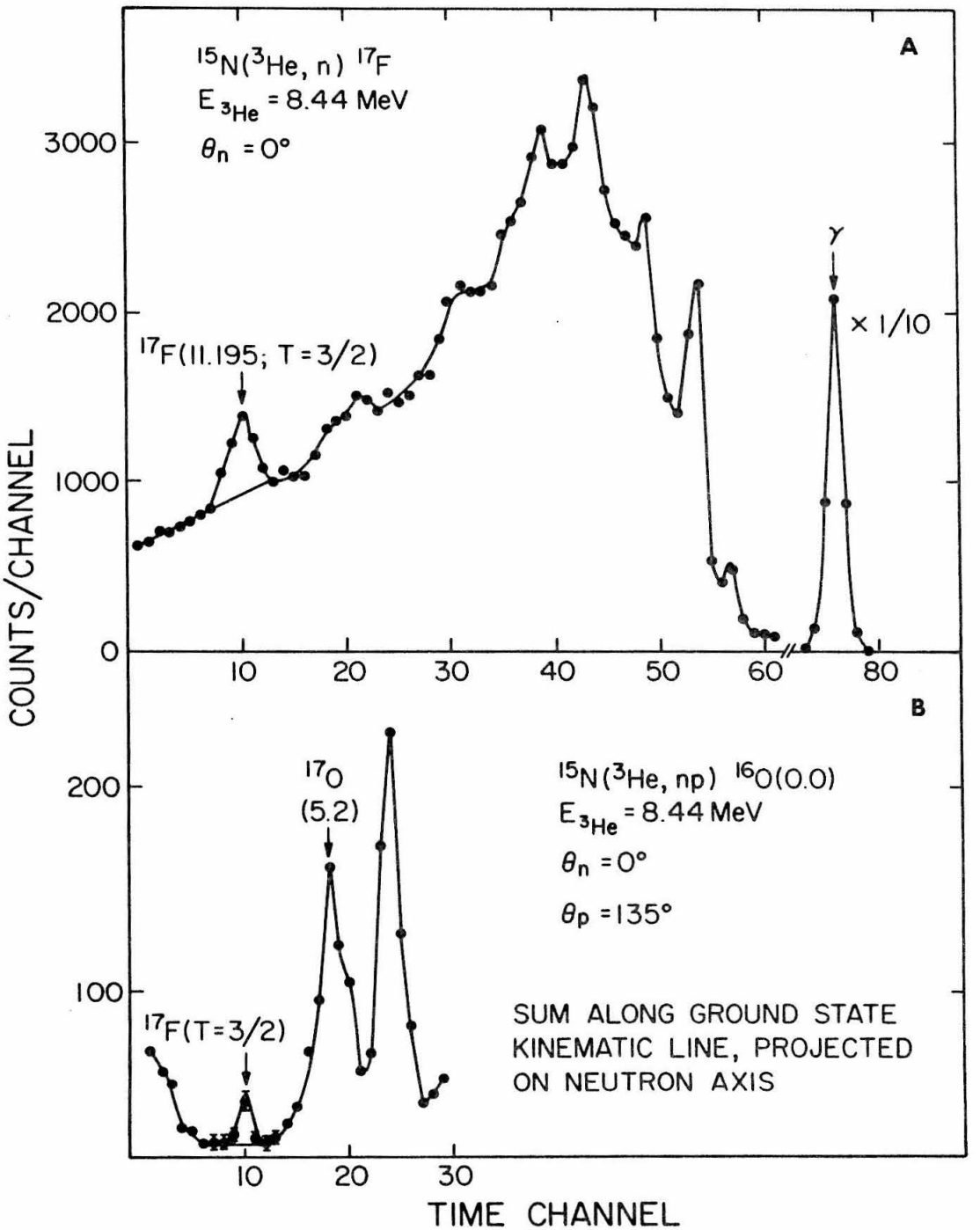
A
$^{15}N(^{3}He, n)\ ^{17}F$
$E_{^{3}He} = 8.44$ MeV
$\theta_n = 0°$
$^{17}F(11.195;\ T=3/2)$
γ
× 1/10
COUNTS/CHANNEL
3000
2000
1000
0
10
20
30
40
50
60
80
B
^{17}O
(5.2)
$^{15}N(^{3}He, np)\ ^{16}O(0.0)$
$E_{^{3}He} = 8.44$ MeV
$\theta_n = 0°$
$\theta_p = 135°$
$^{17}F(T=3/2)$
SUM ALONG GROUND STATE
KINEMATIC LINE, PROJECTED
ON NEUTRON AXIS
200
100
10
20
30
TIME CHANNEL

FIGURE 32

Projections on the neutron axis of the kinematic line from the $^{15}N(^{3}He,np)^{16}O$ (6.05 + 6.13) reaction at (A) 9.18 MeV, (B) 9.03 MeV and (C) 8.93 MeV incident energy for $\theta_n = 0^o$, $\theta_p = 145^o$. For a discussion of the peaks and background levels indicated by the solid lines, see Page 52.

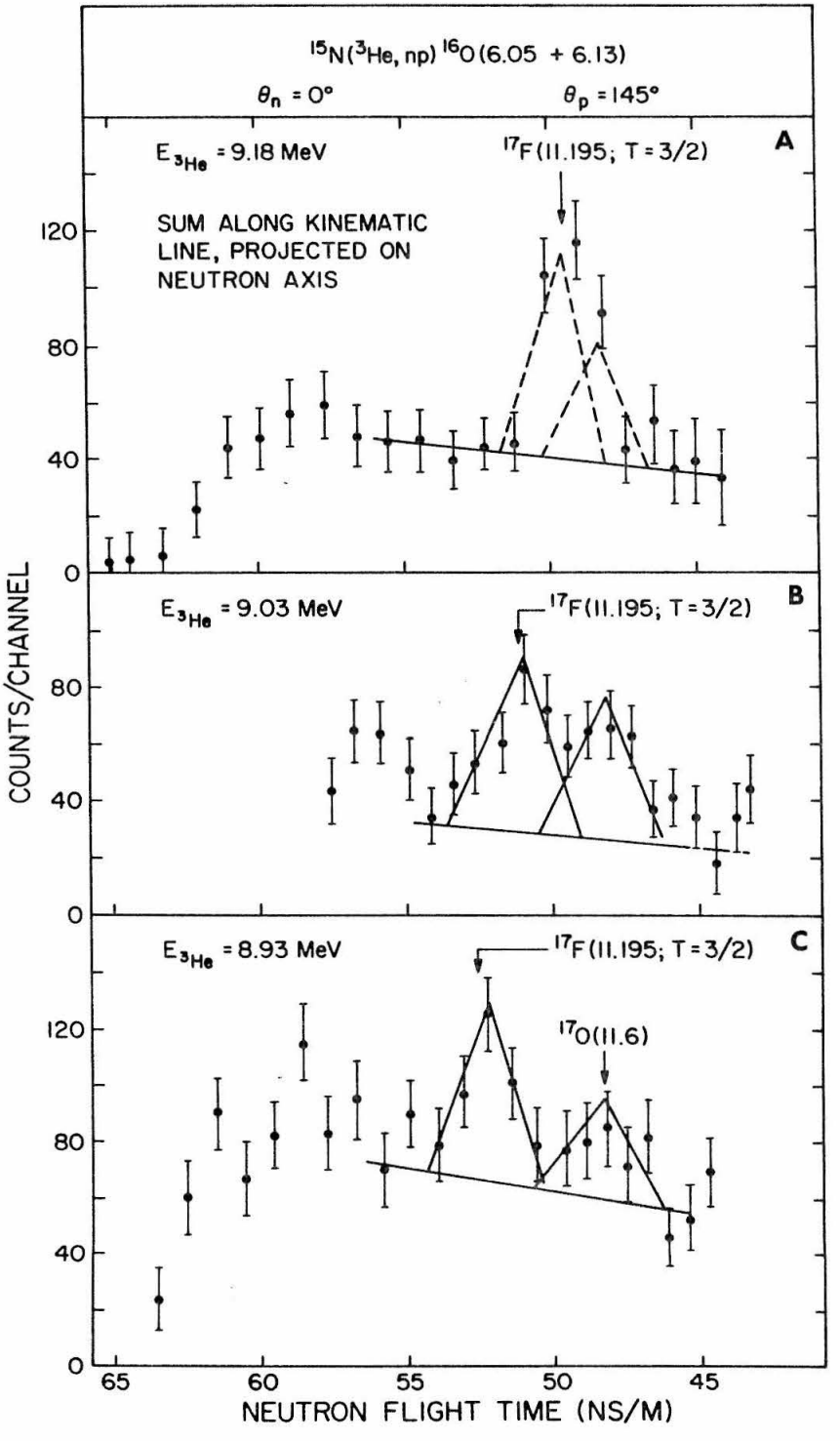
$^{15}N(^3He, np)\,^{16}O(6.05 + 6.13)$
$\theta_n = 0°$
$\theta_p = 145°$
$E_{^3He}$ = 9.18 MeV
$^{17}F(11.195; T = 3/2)$
A
SUM ALONG KINEMATIC LINE, PROJECTED ON NEUTRON AXIS
$E_{^3He}$ = 9.03 MeV
$^{17}F(11.195; T = 3/2)$
B
$E_{^3He}$ = 8.93 MeV
$^{17}F(11.195; T = 3/2)$
$^{17}O(11.6)$
C
COUNTS/CHANNEL
0
40
80
120
65
60
55
50
45
NEUTRON FLIGHT TIME (NS/M)

FIGURE 33

Projections on the neutron axis of the kinematic line from the $^{15}N(^{3}He,np)^{16}O$ (6.05 + 6.13) reaction at (A) 9.68 MeV, (B) 9.58 MeV and (C) 9.48 MeV incident energy for $\theta_p = 0^o$, $\theta_n = 30^o$. The solid lines are merely to guide the eye. The arrows indicate the expected positions of enhancements due to the neutron decay of levels in ^{17}O at 11.023 and 11.075 MeV to $^{16}O(6.13)$ and $^{16}O(6.05)$. For further discussion of these spectra, see Page 57.

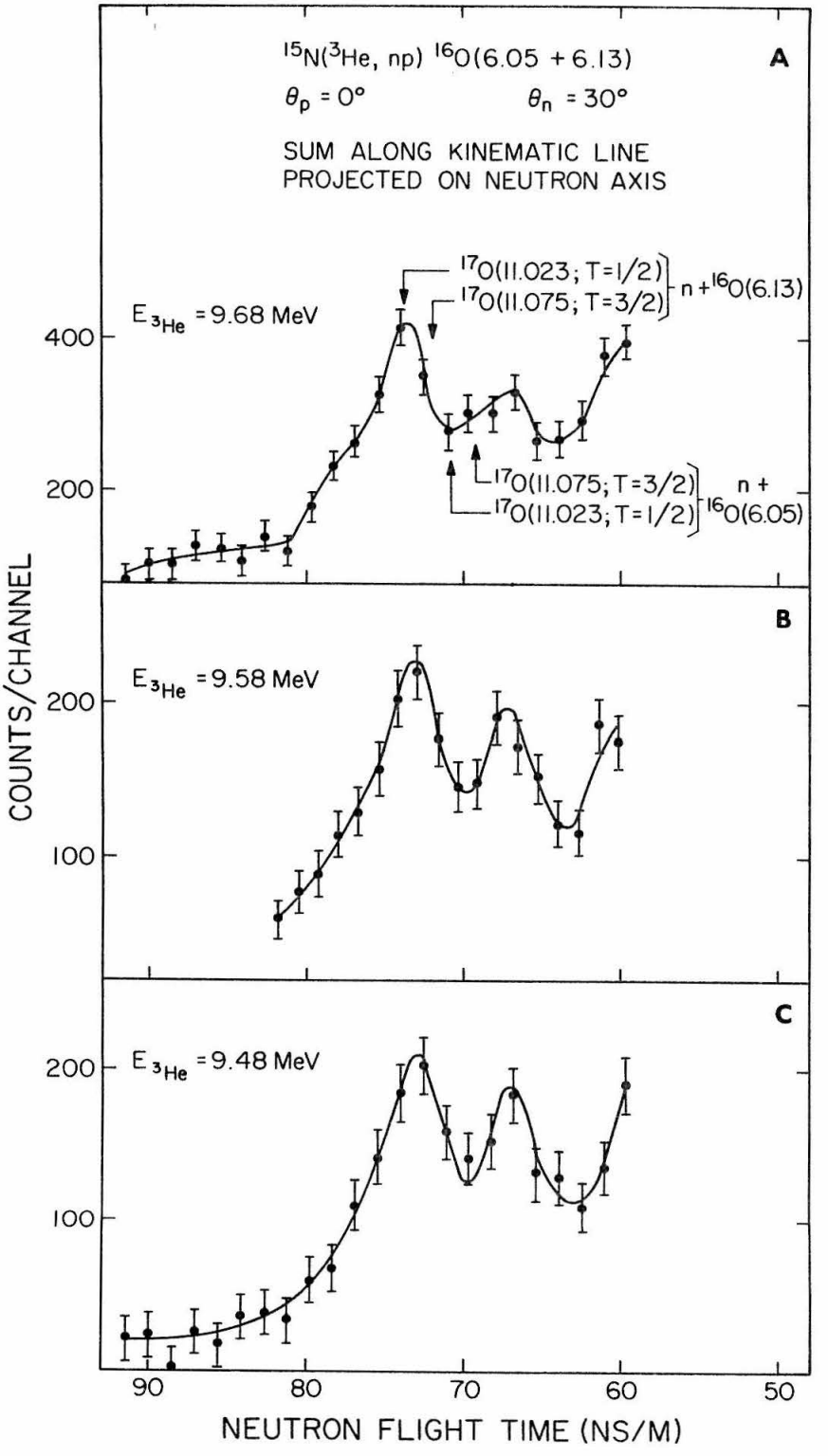
$^{15}N(^3He, np)\ ^{16}O(6.05 + 6.13)$
A
$\theta_p = 0°$
$\theta_n = 30°$
SUM ALONG KINEMATIC LINE
PROJECTED ON NEUTRON AXIS
$^{17}O(11.023; T=1/2)$
$^{17}O(11.075; T=3/2)$
$n + ^{16}O(6.13)$
$E_{^3He} = 9.68$ MeV
400
200
$^{17}O(11.075; T=3/2)$
$^{17}O(11.023; T=1/2)$
$n + ^{16}O(6.05)$
B
$E_{^3He} = 9.58$ MeV
200
100
C
$E_{^3He} = 9.48$ MeV
200
100
COUNTS/CHANNEL
90
80
70
60
50
NEUTRON FLIGHT TIME (NS/M)

FIGURE 34

A. Spectrum of protons detected in the 24" radius magnetic-spectrometer from the $^{15}N(^{3}He,p)^{17}O$ reaction at an incident energy of 9.6 MeV. The horizontal scale is NMR frequency, which is proportional to particle momentum.

B. Spectrum of α-particles from the $^{18}O(^{3}He,\alpha)^{17}O$ reaction at 12 MeV incident energy. The peak labeled $^{11}C(0.0)$ is due to the $^{12}C(^{3}He,\alpha)$ reaction on carbon contaminants in the target.

For further discussion of these spectra, see Page 58.

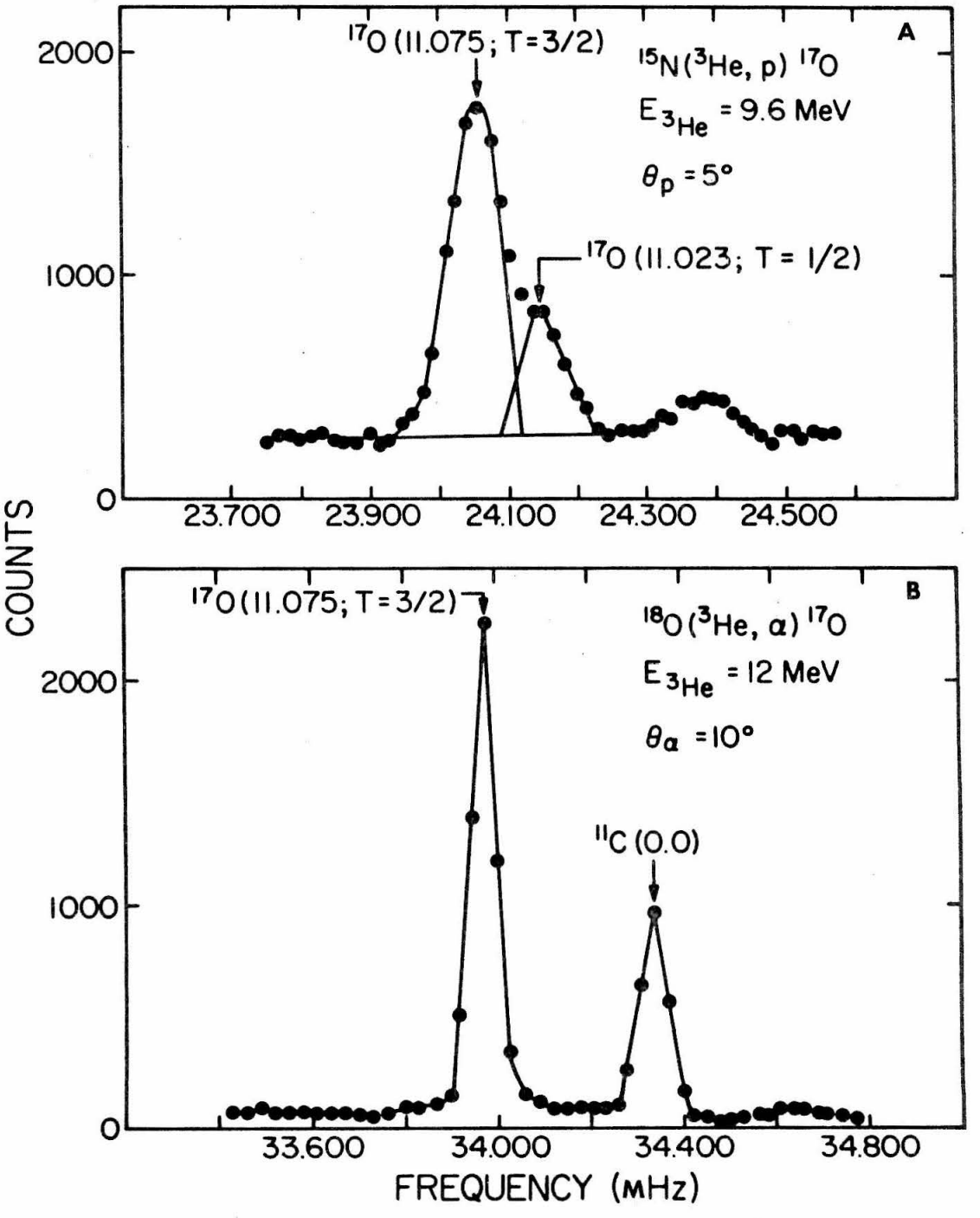
A
^{17}O (11.075; T=3/2)
^{15}N(^{3}He, p) ^{17}O
$E_{^{3}He}$ = 9.6 MeV
θ_p = 5°
^{17}O (11.023; T = 1/2)
2000
1000
0
23.700
23.900
24.100
24.300
24.500
B
^{17}O (11.075; T=3/2)
^{18}O(^{3}He, α) ^{17}O
$E_{^{3}He}$ = 12 MeV
θ_α = 10°
^{11}C (0.0)
2000
1000
0
33.600
34.000
34.400
34.800
COUNTS
FREQUENCY (MHz)

FIGURE 35

A. Energy spectrum of protons and deuterons from the $^{15}N(^{3}He,p)^{17}O$ and $^{15}N(^{3}He,d)^{16}O$ reactions at 9.58 MeV incident energy. Clearly visible are the peaks corresponding to the $^{17}O(11.075;\ T = 3/2)$ level and the d_o peak which was monitored during all $^{15}N(^{3}He,np)^{16}O$ coincidence runs.

B. Projection on the proton axis of the kinematic line due to the $^{15}N(^{3}He,np)^{16}O(0.0)$ reaction at an incident energy of 9.58 MeV, for $\theta_p = 0^{o}$, $\theta_n = 70^{o}$. The peak near channel 12 is assumed to correspond to decays of the $^{17}O(11.075)$ level to the ground state of ^{16}O.

For further discussion of these spectra, see Page 58.

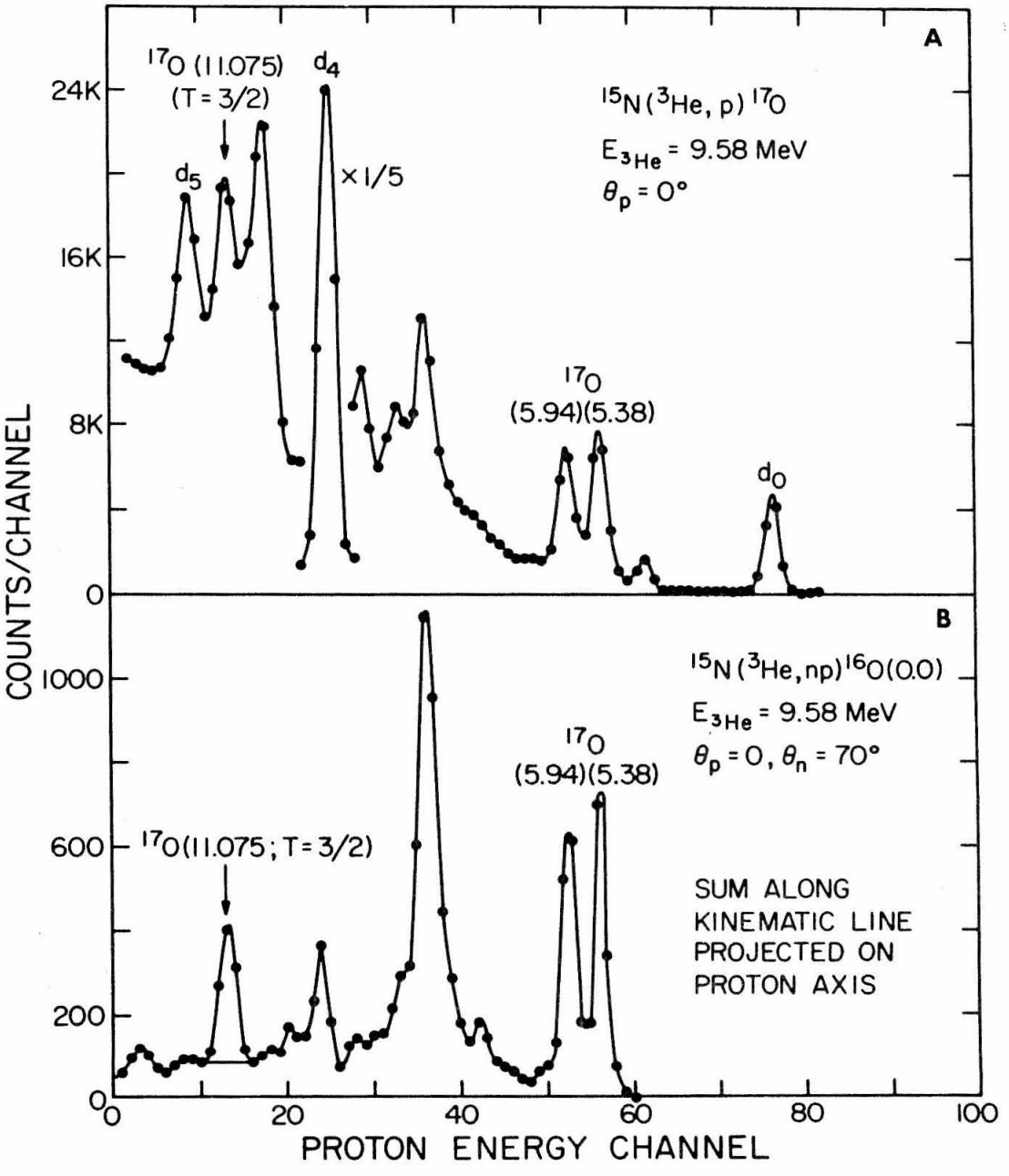
A
^{17}O (11.075)
(T = 3/2)
d_4
d_5
×1/5
^{15}N(^{3}He, p) ^{17}O
$E_{^3He}$ = 9.58 MeV
θ_p = 0°
^{17}O
(5.94)(5.38)
d_0
24K
16K
8K
0
B
^{15}N(^{3}He,np)^{16}O(0.0)
$E_{^3He}$ = 9.58 MeV
θ_p = 0, θ_n = 70°
^{17}O
(5.94)(5.38)
^{17}O(11.075; T = 3/2)
SUM ALONG
KINEMATIC LINE
PROJECTED ON
PROTON AXIS
1000
600
200
0
0
20
40
60
80
100
COUNTS/CHANNEL
PROTON ENERGY CHANNEL

FIGURE 36

Block diagram of the electronic circuitry used in the study of the $^{18}O(^{3}He,\alpha)^{17}O^{*}(n)^{16}O$ reaction, described in Section IV, C. The commercially available instruments symbolized by the boxes are:

1. Time pickoff — Ortec Model 290.
2. Preamplifier — Tennelec Model TC 130.
3. Amplifier — Ortec Model 410.
4. Single channel analyzer — Ortec Model 420.
5. Zero-crossing discriminator — Ortec Model 417.
6. Time-to-amplitude converter — Ortec Model 437.
7. Coincidence — Ortec Model 409.
8. Multichannel analyzer — RIDL 400 Channel.

This circuitry is discussed on Page 60.

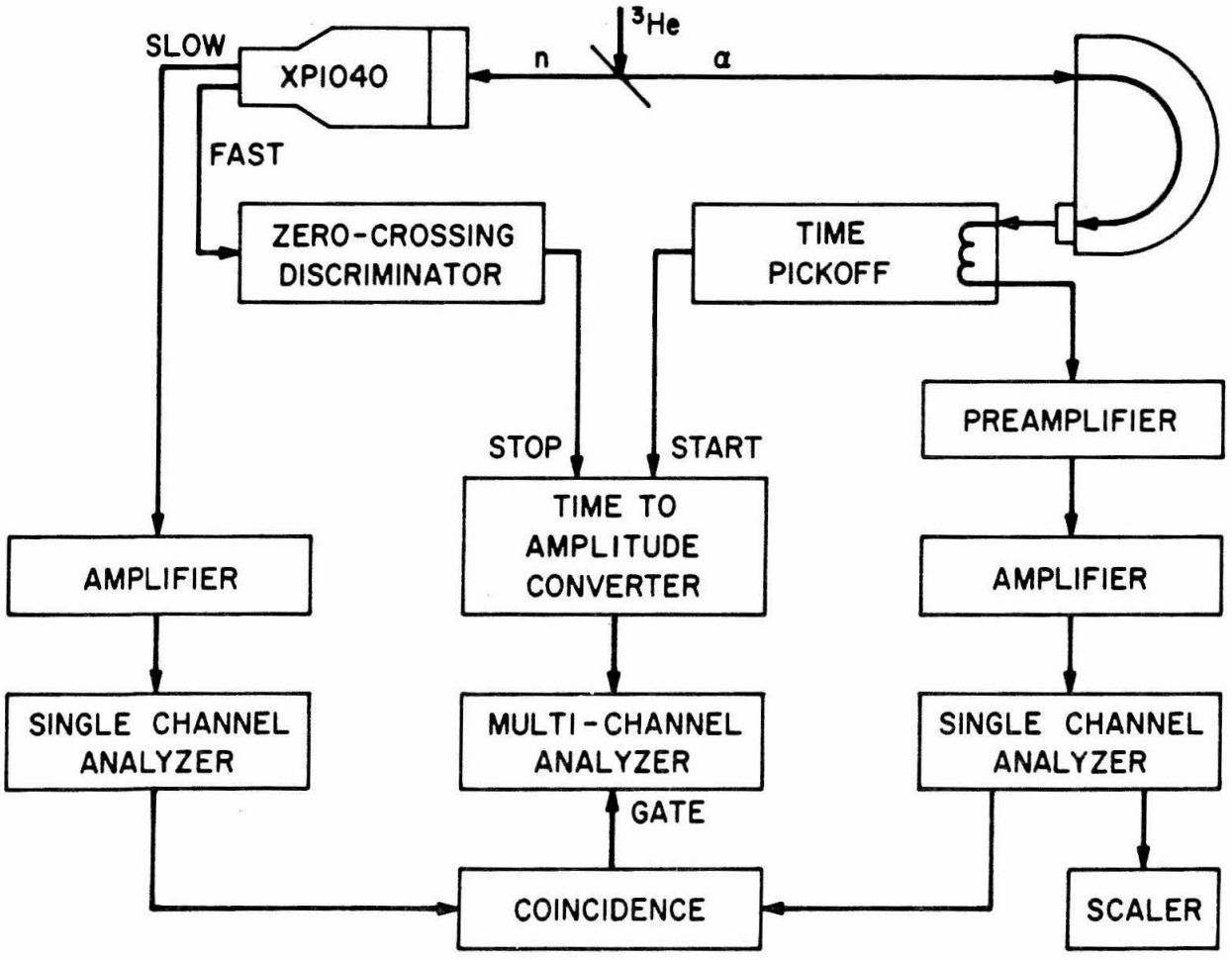
SLOW
XP1040
FAST
^{3}He
n
α
ZERO-CROSSING DISCRIMINATOR
TIME PICKOFF
PREAMPLIFIER
STOP
START
TIME TO AMPLITUDE CONVERTER
AMPLIFIER
AMPLIFIER
SINGLE CHANNEL ANALYZER
MULTI-CHANNEL ANALYZER
SINGLE CHANNEL ANALYZER
GATE
COINCIDENCE
SCALER

FIGURE 37

Time-of-flight spectrum of neutrons in coincidence with α-particles detected from the $^{18}O(^{3}He,\alpha)^{17}O(11.075,\ T = 3/2)$ reaction. A uniform chance coincidence background and normalized real-coincidence background spectra have been subtracted. The solid curve is a line shape for 5.6 MeV neutrons, obtained from the $^{13}C(\alpha,n)^{16}O(0.0)$ reaction at an incident energy of 4.70 MeV; the darker dashed curve is a line shape for 0.86 MeV neutrons, obtained from the t(p,n) reaction at 1.7 MeV. The lighter dashed curve indicates the maximum background assumed in the calculation of the branching ratio for the decay of the $^{17}O(T = 3/2)$ level to ^{16}O (6.05 + 6.13). For further discussion of this spectrum, see Page 63.

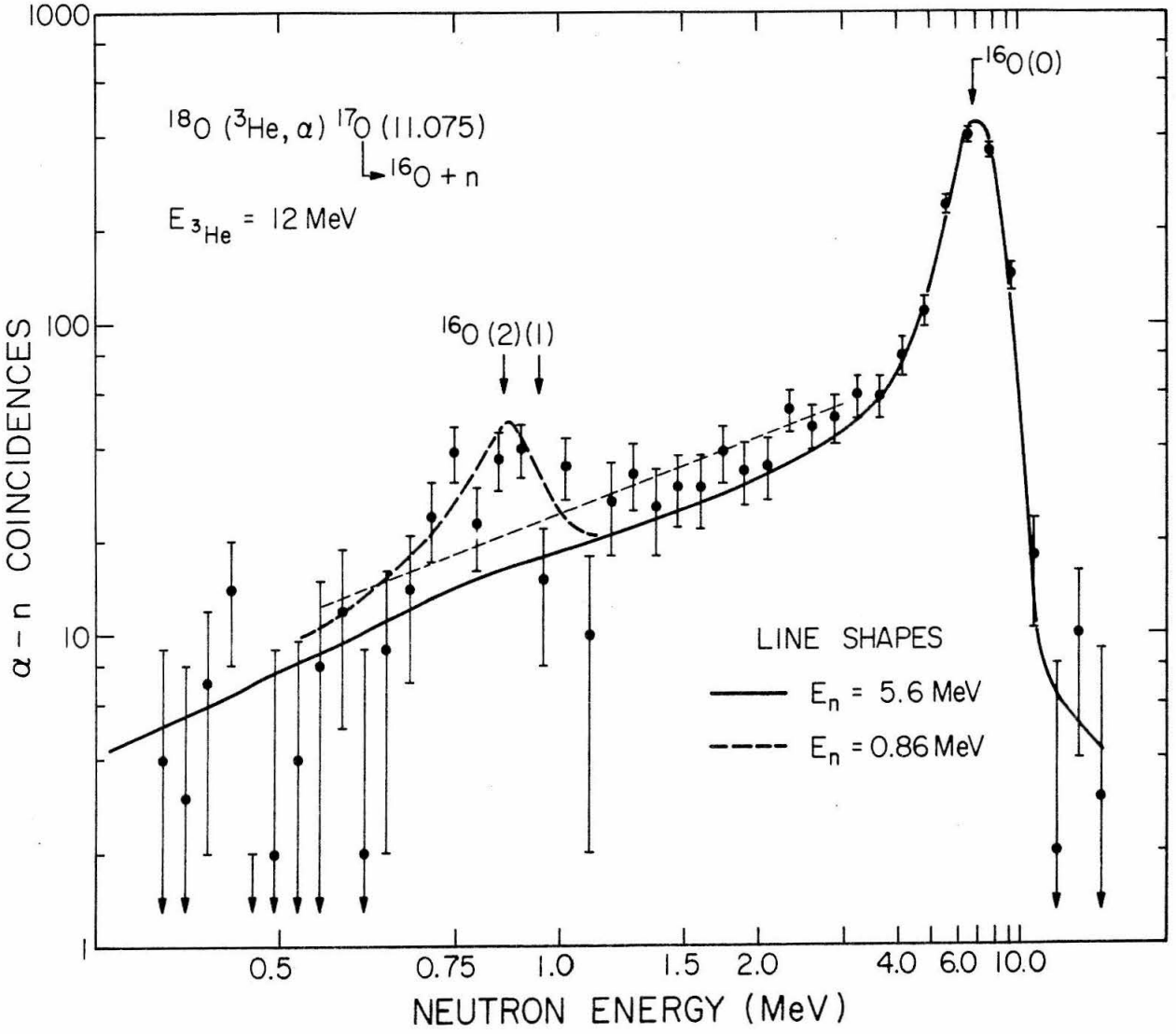
1000
100
10
1
α – n COINCIDENCES
^{18}O (^{3}He, α) ^{17}O (11.075)
↳ ^{16}O + n
$E_{^{3}He}$ = 12 MeV
^{16}O (2)(1)
^{16}O(0)
LINE SHAPES
E_n = 5.6 MeV
E_n = 0.86 MeV
0.5
0.75
1.0
1.5
2.0
4.0
6.0
10.0
NEUTRON ENERGY (MeV)

FIGURE 38

Line shapes for 5.6 MeV neutrons determined from the $^{13}C(^{3}He,n)^{16}O$ (0.0) reaction at 80^{o} for 4.7 MeV incident energy with the neutron detector in the magnet geometry (solid curve) and inside the cannon mount (dashed curve). The arrows indicate the region summed to determine the relative detection efficiency for the two geometries. For a discussion of the magnet geometry, see Page 58. For a description of the cannon mount, see Page 9. For further discussion of this figure, see Page 66.

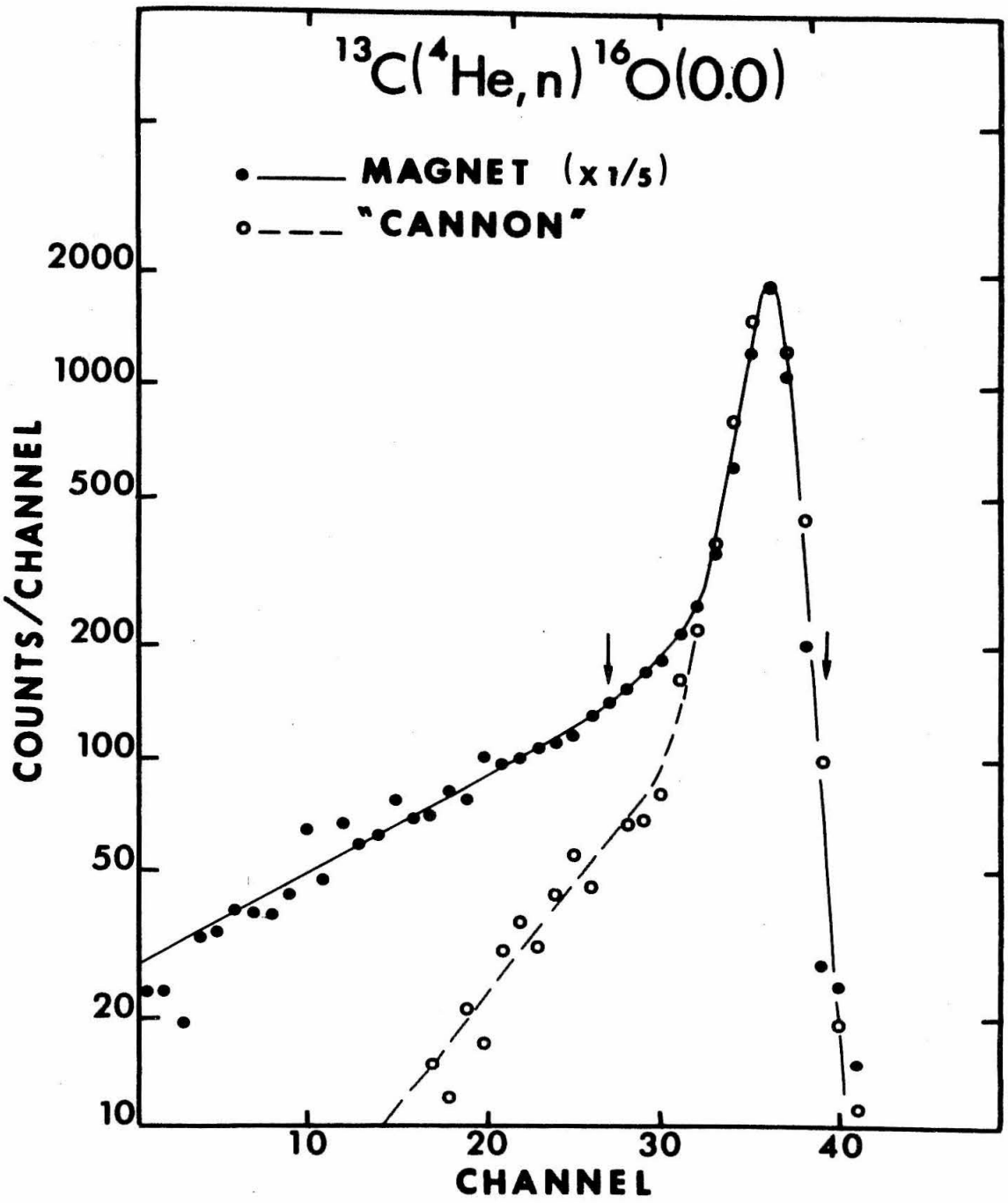
$^{13}C(^{4}He,n)^{16}O(0.0)$
MAGNET (x 1/5)
"CANNON"
COUNTS/CHANNEL
2000
1000
500
200
100
50
20
10
10
20
30
40
CHANNEL